



Title	Development of In-Bi alloys with low-melting temperature for microelectronics interconnections
Author(s)	Jin, Sanghun
Citation	大阪大学, 2019, 博士論文
Version Type	VoR
URL	https://doi.org/10.18910/73569
rights	
Note	

The University of Osaka Institutional Knowledge Archive : OUKA

<https://ir.library.osaka-u.ac.jp/>

The University of Osaka

Doctoral Dissertation

**Development of In-Bi alloys with low-
melting temperature for
microelectronics interconnections**

JIN SANGHUN

July 2019

Graduate School of Engineering
Osaka University

Supervisor

Prof. Hiroshi Nishikawa, Ph. D.

Department of Manufacturing Process, Joining and Welding Research Institute

Osaka University

Doctoral Committee

Prof. Hiroshi Nishikawa, Ph. D

Department of Manufacturing Process, Joining and Welding Research Institute

Osaka University

Prof. Soshu Kiriara, Ph. D.

Division of Sustainable Energy and Environmental Engineering, Graduate School of Engineering

Osaka University

Assoc. Prof. Hiroaki Muta, Ph. D.

Division of Sustainable Energy and Environmental Engineering, Graduate School of Engineering

Osaka University

Contents

Contents	i
List of Figures	v
List of Tables	x
Chapter 1 Research Background	1
1.1 Overview of soldering	1
1.1.1 Interconnection technology in electronic packaging	1
1.1.2 Flip chip bonding	3
1.1.3 Step soldering	4
1.2 Recent trend of soldering	5
1.2.1 Definition of soldering	5
1.2.2 Harmfulness and Regulations of lead (Pb)	8
1.2.3 Lead-free solders	10
1.2.4 Usage environment of lead-free solder	12
1.3 Low temperature solder	16
1.4 Next-generation electronic devices by Flexible substrates	19
1.4.1 Flexible electronics markets growth	19
1.4.2 Materials for Flexible substrate	20
1.5 Motivation of research	22
1.6 Purpose and outline of this study	22
References	24

Chapter 2 Basic properties of In–Bi alloys	32
2.1 Introduction	32
2.2 Experimental	33
2.2.1 Fabrication of In–Bi alloys	33
2.2.2 Microstructure, melting temperatures, and elemental analysis	34
2.2.3 Tensile test	34
2.3 Results and Discussion	35
2.3.1 Phase constitution and microstructure of bulk In–xBi alloys	35
2.3.2 Melting properties	38
2.3.3 Mechanical properties	42
2.3.4 Fracture Characteristics	44
2.4 Conclusion	47
References	48
Chapter 3 Melting properties and microstructure of In–Bi alloys during isothermal aging	51
3.1 Introduction	51
3.2 Experimental	52
3.2.1 Alloy preparation and aging process	52
3.2.2 Melting temperature, elemental analysis and microstructure	54
3.3 Results and Discussion	56
3.3.1 Melting properties, phase constitution and microstructure	56
3.4 Conclusion	69
References	70
Chapter 4 Mechanical properties of In–Bi alloys during isothermal aging	72
4.1 Introduction	72
4.2 Experimental	72
4.2.1 Alloy preparation and aging process	72
4.2.2 Tensile testing	75

4.3	Results and discussion	75
4.3.1	Mechanical properties	75
4.3.2	Fracture modes	82
4.4	Conclusion	89
	References	90
Chapter 5 Shear properties of In–Bi alloy joints with Cu substrates		92
5.1	Introduction	92
5.2	Experimental	93
5.2.1	Joint sample preparation	93
5.2.2	Thermal aging and IMC thickness measurement	94
5.2.3	Shear strength test	95
5.2.4	Microstructural characterization	95
5.3	Results and discussions	96
5.3.1	Cross-sectional microstructure of Cu/In–Bi alloy/Cu joints	96
5.3.2	Morphology of interfacial IMCs and growth rate of IMCs after thermal aging	99
5.3.3	Effect of aging time on shear strengths	105
5.3.4	Fracture surfaces in alloy joints after shear test	107
4.5	Conclusion	109
	References	111
Chapter 6 Transient Liquid Phase Bonding of In-Bi alloy with added Cu particles ...		113
6.1	Introduction	113
6.1.1	TLP bonding process	114
6.2	Experimental	115
6.2.1	TLP bonding sample preparation	115
6.2.2	TLP bonding process	117
6.2.3	Microstructural characterization	117
6.2.4	Differential scanning calorimetry (DSC) analysis	118

6.3 Results and discussions	118
6.3.1 Estimating the Cu content required for TLP bonding	118
6.3.2 Microstructure of the alloy joints	121
6.3.3 Thermal analysis of the compositional shift by DSC	123
6.3.4 Shear strength of the alloy joints	124
6.4 Conclusion	126
References	127
Chapter 7 Summary	130
7.1 Summary	130
7.2 Environmental assessment of In-Bi alloys bonding	133
7.2.1 Materials and bonding process	133
7.2.2 Recycling from e-waste	133
7.3 Future work	136
References	137
Research achievements	138
Acknowledgments	139

List of Figures

Chapter 1

Figure 1.1 Schematically illustrates for (a) single chip and (b) multichip module (MCM) package	2
Figure 1.2 Schematically illustrates of (a) flip chip binding and (b) BGA package with wire bonding technology	3
Figure 1.3 Schematically illustrates of step soldering	4
Figure 1.4 IC package substrate of mobile phone	5
Figure 1.5 Bonding technology used in the electronics industry	6
Figure 1.6 Schematic of soldering process	7
Figure 1.7 A schematic to show lead toxicity in (PCBs) effects on human health	8
Figure 1.8 Schematically illustrates of design of (a) initial joint, (b) melting and wetting, (c) solid-liquid interdiffusion and (d) solidification for TLP bonding	14
Figure 1.9 The DSC results of Sn–Bi–30Cu (a) before reflow (paste), (b) after reflow at 200 °C for 10 min, and (c) after reflow at 200 °C for 50 min	14
Figure 1.10 The variation of (a) thickness of total, dense and porous Ag layers and (b) the measured porosity of porous Ag layers	15
Figure 1.11 Stacked BGA. Package: (a) photo image, (b) and (c) cross-sectional schematic image	17
Figure 1.12 Typical SMT (Surface Mounting Technology) defect modes	17
Figure 1.13 Global Flexible Electronics Market Size and Forecast, 2017-2026	19
Figure 1.14 The analysis of flexible electronics market by product, 2018	20
Figure 1.15 Roadmap of flexible substates technology and products	23

Chapter 2

Figure 2.1 Phase diagram of In–Bi binary system	33
--	----

Figure 2.2 The schematic illustration of the tensile samples	35
Figure 2.3 XRD patterns of In–Bi solders: (a) In–50Bi, (b) In–40Bi, (c) In–33.7Bi, (d) In–30Bi	36
Figure 2.4 The EPMA mapping results of the In–Bi alloys	37
Figure 2.5 DSC curves for various solder compositions: (a) In–50Bi, (b) In–40Bi, (c) In–33.7Bi, (d) In–30Bi	39
Figure 2.6 Tensile test results by alloy compositions: (a) In–50Bi, (b) In–40Bi, (c) In–33.7Bi, (d) In–30Bi	42
Figure 2.7 Corresponding results of the tensile tests	43
Figure 2.8 Photographs of the bulk specimens after tensile tests for observing change in length	45
Figure 2.9 Fracture surfaces on side view after tensile tests: (a) In–50Bi, (b) In–40Bi, (c) In–33.7Bi, (d) In–30Bi	45
Figure 2.10 Fracture surfaces on top view after tensile tests: (a) In–50Bi, (b) In–40Bi, (c) In–33.7Bi, (d) In–30Bi	46

Chapter 3

Figure 3.1 The geometry and size of the tensile test specimen	53
Figure 3.2 The illustration of thermal aging test	53
Figure 3.3 Eutectic spacing within the eutectic In–33.7Bi alloy bulk after 1008 h of thermal aging	55
Figure 3.4 DSC curves under thermal aging test at 40 and 60 °C after 168 h, 504 h and 1008 h: (a) In–50Bi, (b) In–40Bi, (c) In–33.7Bi and (d) In–30Bi	56
Figure 3.5 Comparison of XRD (X-ray Diffraction) patterns for In–Bi alloys under thermal aging test at 40 and 60 °C after 168 h, 504 h and 1008 h: (a) In–50Bi, (b) In–40Bi, (c) In–33.7Bi and (d) In–30Bi	59
Figure 3.6 Cross-sectional SEM images of In–Bi alloys under thermal aging test at 60 °C after 504 h: (a) In–50Bi, (b) In–40Bi, (c) In–33.7Bi and (d) In–30Bi	62
Figure 3.7 Cross-sectional SEM images of In–Bi alloys: (a) as-cast and (b) thermally aged for 1008 h at 40 °C and 60 °C	64

Figure 3.8 Electron probe microanalyzer (EPMA) elemental mapping results of the In–Bi alloys after thermally aged: (a) In–50Bi, (b) In–40Bi, (c) In–33.7Bi and (d) In–30Bi	65
Figure 3.9 Average eutectic spacing within the eutectic In–33.7Bi alloy bulk before and after thermal aging	68

Chapter 4

Figure 4.1 The geometry and size of the tensile test specimen	73
Figure 4.2 The illustration of thermal aging test	74
Figure 4.3 The image of the tensile test: (a) In–50Bi, (b) In–40Bi, (c) In–33.7Bi and (d) In–30Bi	75
Figure 4.4 Tensile test results of In–Bi alloys: (a) as-cast and (b) thermally aged for 168 h, (c) 504 h, and (d) 1008 h at 40 °C	77
Figure 4.5 The effect of aging on the tensile properties of In–Bi alloys: (a) ultimate tensile strength (UTS) and (b) elongation at 40 °C	78
Figure 4.6 Tensile properties by indium content: (a) UTS and (b) elongation at 40 °C	78
Figure 4.7 Tensile properties by thermal aging time: (a) UTS and (b) elongation at 40 °C	78
Figure 4.8 Tensile test results of In–Bi alloys: (a) as-cast and (b) thermally aged for 168 h, (c) 504 h, and (d) 1008 h at 60 °C	80
Figure 4.9 The effect of aging on the tensile properties of In–Bi alloys: (a) ultimate tensile strength (UTS) and (b) elongation at 60 °C	881
Figure 4.10 Tensile properties by indium content: (a) UTS and (b) elongation at 60 °C	81
Figure 4.11 Tensile properties by thermal aging time: (a) UTS and (b) elongation at 60 °C	81
Figure 4.12 Photographs of the bulk specimens after tensile tests for observing change in length of In–Bi alloys: (a) In–50Bi, (b) In–40Bi, (c) In–33.7Bi and (d) In–30Bi thermally aged at 40 °C. And (e) In–50Bi, (f) In–40Bi, (g) In–33.7Bi and (h) In–30Bi thermally aged at 60 °C	83
Figure 4.13 Fracture surfaces of tensile specimens (side view): (a) as-cast and (b) thermally aged for 1008 h at 40 °C	84
Figure 4.14 Fracture surfaces of tensile specimens by thermal aging time (side view)	85
Figure 4.15 Fracture surfaces of tensile specimens (top view): (a) as-cast and (b) thermally	

aged for 1008 h at 40 °C	86
Figure 4.16 Fracture surfaces of tensile specimens (top view)	87
Figure 4.17 The morphology of a ductile fracture	88

Chapter 5

Figure 5.1 Illustration of the heating process: (a) a schematic diagram of the Cu–Cu joint and real joint sample (b) the heating profile of the process	93
Figure 5.2 Schematic illustration of the shear test	95
Figure 5.3 (a) Cross-sectional microstructure of In–Bi alloys as reflowed, (b) thermally aged for 1008 h at 40 °C and (c) 60 °C	96
Figure 5.4 Cross-sectional microstructure of In–Bi alloys as reflowed and thermally aged	97
Figure 5.5 Cross-sectional image of In–Bi alloys as reflowed and thermally aged.....	98
Figure 5.6 EPMA mapping results of In–Bi alloys after thermal aging for 1008 h (a) at 40 °C and (b) at 60 °C	100
Figure 5.7 Cross-sectional EPMA image of the interface after thermal aging for 504 h at 60 °C	102
Figure 5.8 Cross-sectional images of the interfacial IMC layers of the as-reflowed and thermally aged In–Bi alloy joints after aging for 168, 504 and 1008 h (a) at 40 °C and (b) 60 °C	103
Figure 5.9 Result of IMCs thickness after thermal aging (a) at 40 °C and (b) at 60 °C	104
Figure 5.10 Relationship between IMC thickness and square root of aging time (a) at 40 °C and (b) at 60 °C	104
Fig. 5.11 Result of shear strength test after thermal aging (a) at 40 °C and (b) at 60 °C	106
Figure 5.12 EPMA mapping results of fracture surface of (a) as-reflowed and after thermal aging for 1008 h (b) at 40 °C and (c) at 60 °C	108

Chapter 6

Figure 6.1 Illustration of TLP bonding process	114
Figure 6.2 The process of make an alloy paste	115
Figure 6.3 SEM image of (a) Cu particles before addition to the alloy paste and (b) the frequency of Cu particles diameters	116
Figure 6.4 The schematic illustration of the TLP bonding sample	116
Figure 6.5 (a) The heating profile of the process and (b) the schematic illustration of the thermos-compression bonding	117
Figure 6.6 The binary phase diagram of Cu and In	119
Figure 6.7 The microstructure of (a) In–Bi and (b) In–Bi–30Cu after reflow at 100 °C for 1 min	121
Figure 6.8 The microstructure of In–Bi–30Cu after reflow at 100 °C for (a) 10 min and (b) 50 min	121
Figure 6.9 The EPMA analysis of In–Bi–30Cu for (a) 10 min and (b) 50 min	122
Figure 6.10 The line analysis of In–Bi–30Cu after reflow at 100 °C	122
Figure 6.11 The DSC results of In–Bi–30Cu (a) before reflow (paste), (b) after reflow at 100 °C for 10 min, and (c) after reflow at 100 °C for 500 min	123
Figure 6.12 The shear strength results of In–Bi–30Cu alloy	124
Figure 6.13 (a) Cross-sectional image of In–Bi–30Cu alloy after reflowed at 100 °C for 10 min and (b) 50 min	125
Figure 6.14 (a) Cross-sectional image of In–Bi–30Cu alloy after thermos--compressed at 100 °C for 10 min and (b) 50 min	125

Chapter 7

Figure 7.1 Illustration of environmental assessment of In–Bi alloys.....	134
---	-----

List of Tables

Chapter 2

Table 2.1 Quantitative analysis of points A, B, C and D in Fig. 2.4	38
Table 2.2 Results of DSC experiments with In-Bi alloys	41
Table 2.3 Comparison of tensile test results of low-temperature alloys	44

Chapter 3

Table 3.1 The temperature of thermal aging test by calculated	52
Table 3.2 Using condition of electronic devices	52
Table 3.3 Sample size of thermal aging test	54
Table 3.4 Results of DSC experiments with In-Bi alloys under thermal aging at 40 °C after 1008 h	58
Table 3.5 Energy-dispersive spectroscopy (EDS) point analysis results on point; A, B, C, and D	67
Table 3.6 Eutectic spacing of In-33.7Bi alloy	68

Chapter 4

Table 4.1 Sample size of thermal aging test	74
--	----

Chapter 5

Table 5.1 Sample size of thermal aging test	94
Table 5.2 Point analysis of IMCs	102

Table 5.3 Calculated the layer growth coefficient of IMC layers and the linear correlation coefficient (R^2)	105
---	-----

Chapter 6

Table 6.1 Mathematical calculation of sufficient of Cu particle	120
--	-----

Chapter 1

Research background

1.1 Overview of soldering

1.1.1 Interconnection technologies in electronic packaging

Due to the rapid development of the IT (Information Technology) industry and the demand for new services, semiconductors are evolving toward smaller and lighter in terms of weight and size compared to conventional semiconductors. And there is a growing demand for a new type of semiconductor packaging technology that integrates a plurality of devices or chips in a single package in order to implement various data processing and multimedia functions. Particularly, the rapid increase in the market of mobile devices and tablet PC requiring small size and small packages shows that the demand for highly integrated new semiconductor package technology will increase dramatically [1]. The development of high-performance semiconductor chips for high-speed signal processing with the evolution of electronic products and the development of electronic packaging technology for interconnected signal transmission between chips and chips or chips and peripheral devices are also required. However, recently, the performance of electronic products is determined by the signal delay due to the packaging structure rather than the chip itself, and it occupies about 50% of the total

signal delay [2]. Therefore, the development of packaging technology is becoming an increasingly important issue, and many studies are underway to improve it.

Typical packaging of electronic systems consists of several levels, and each level of packaging is associated with interconnection technologies as below [3]:

- Level 0: gate-to-gate interconnection in an monolithic silicon chip/semiconductor;
- Level 1: packaging of semiconductor into chip carrier, multi-chip modules (MCM), and the chip-level interconnects that join the chip to the lead-frames, called first-level interconnection;
- Level 2: Printed circuit board (PCB) level of interconnection in order to connect the components to PCBs and for off-the-board interconnection, named as second-level interconnection;
- Level 3: Connections between PCBs;
- Level 4: Connections between two subassemblies;
- Level 5: Connections among physically separated systems, such as host computer to terminals.

Among these, the interconnections of Level 1 and 2 are becoming an important subject of study due to the increased demands on electronic functionality. And leading to rapid development from single-chip into multichip module packaging as shown in Fig. 1.1.

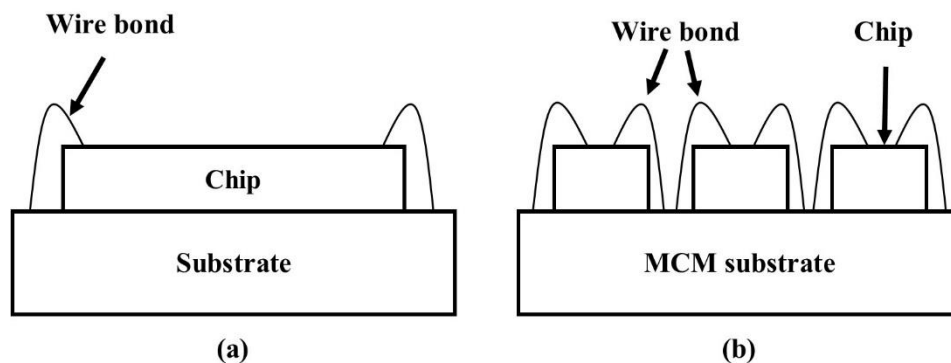


Figure 1.1 Schematically illustrates for (a) single chip and (b) multichip module (MCM) package [3].

A MCM is generically an electronic assembly where multiple integrated circuits (ICs or chips), semiconductor dies and/or other discrete components are integrated, usually onto a unifying substrate, so that in use it is treated as if it were a single component. Packaging of the chips has become a more significant factor in performance. Chip interconnections play a more dominant and limited role in determining overall system speed or performance [4].

1.1.2 Flip chip bonding

Flip Chip Bonding technology is a technique to bond by flip a chip on a substrate or other chip as shown in Figure 1.2 Flip chip bonding technology was first introduced in 1964 by IBM under the name C4 (controlled collapse chip connection) [5]. Flip chip bonding is an interconnection technology such as wire bonding which is traditionally used in packaging. The arrangement of the metal pads on the chip used for wire bonding is one-dimensional, whereas the arrangement of the metal pads on the flip chip bonding is two-dimensionally arranged. thus, Flip chip bonding has the advantage that the number of metal pads that can be connected to the substrate increases by the squared. In 2018, around 35% of the world's wafers were used for flip chip bonding [5].

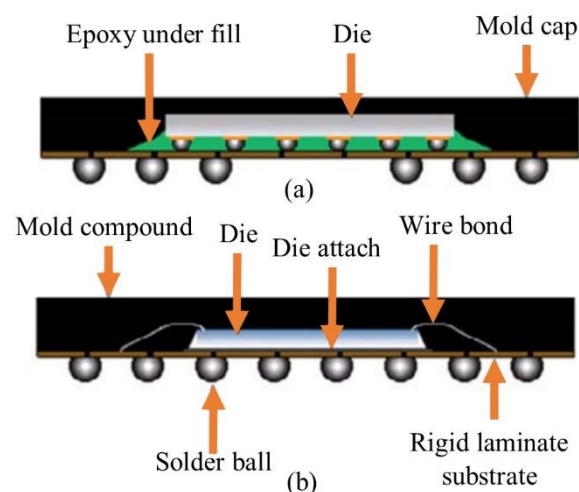


Figure 1.2 Schematically illustrates of (a) flip chip binding and (b) BGA package with wire bonding technology [5].

In terms of interconnection materials, the Pb-based solder alloys have been successfully used in FC interconnection for both the first- and second-level packaging for many years with fair coverage in bump bonding technologies. Bump bonding has some advantages such as bump formed easily by wire bonders, easy to scale up to high volume production and more precise die bond than self-aligning solder assemblies [6].

1.1.3 Step soldering

Step soldering is a method of soldering in which successive joints on a part are joined with solders of successively lower soldering temperatures, so that joints previously soldered are not disturbed as shown in Fig. 1.3.

The availability of solders with lower melting points will make multiple reflow processes on a single board possible. For example, all of the normal components that can tolerate higher reflow temperatures could be soldered to a board using the standard process, and then the lower-temperature components could be added in another reflow process. Since step soldering is a bulk reflow process, it takes less time and is more uniform than hand soldering, and doesn't take any different equipment or special training. [7]

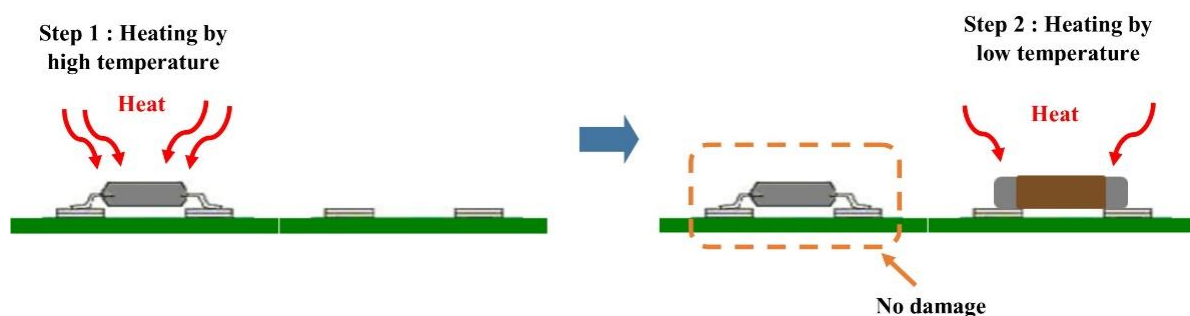


Figure 1.3 Schematically illustrates of step soldering.

1.2 Recent trend of soldering

1.2.1 Definition of soldering

Soldering is widely known as a bonding method for a long time [8]. The soldering is an indispensable technique for board-level packaging on electronic devices, and the importance has increased in recent years in terms of miniaturization and weight reduction of electronic devices. In particular, we believe that a fundamental understanding of soldering technology is required to cope with the development of new technologies every year, in conjunction with environmental regulations such as the use of WEEE (Waste Electrical and Electronic Equipment) and RoHS (Restriction of Hazardous Substances Directive) regulations [9].

Figure 1.4 shows an example of a mobile phone using soldering and a rigid substrate [10]. Soldering technology is an indispensable assembly technology in the modern electronics industry. As refer to the ISO 9454-2 (Soldering and brazing materials) [11], Soldering means a method in which molten solder (filler metal) having a melting point of less than 425 °C penetrates into the gap of the base metal to be bonded.

Soldering is one of the bonding techniques of materials and a kind of welding technology [12]. However, it is different from general melting welding (arc welding, laser welding, etc.) that the base metal is not melted and only solder (filler metal) is melted during soldering [13]. In addition, since the metallurgical bonds are generated between the soldered base metal and the solder, the soldering is different from the bonding using the adhesive. As shown in Figure 1.5, many bonding technologies are used in the electronics industry [14].

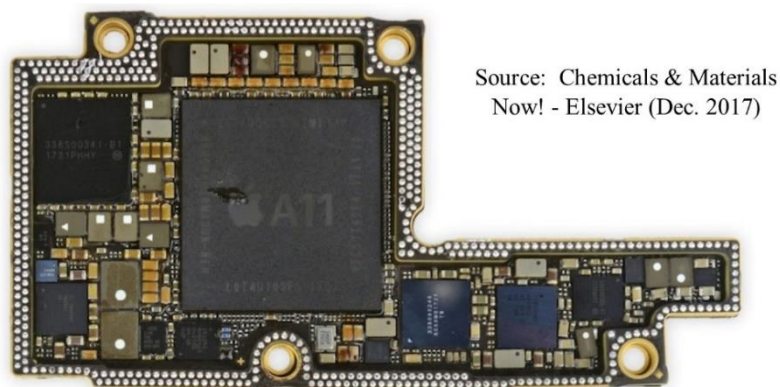


Figure 1.4. IC package substrate of mobile phone [10]. Copy right 2017 Elsevier.

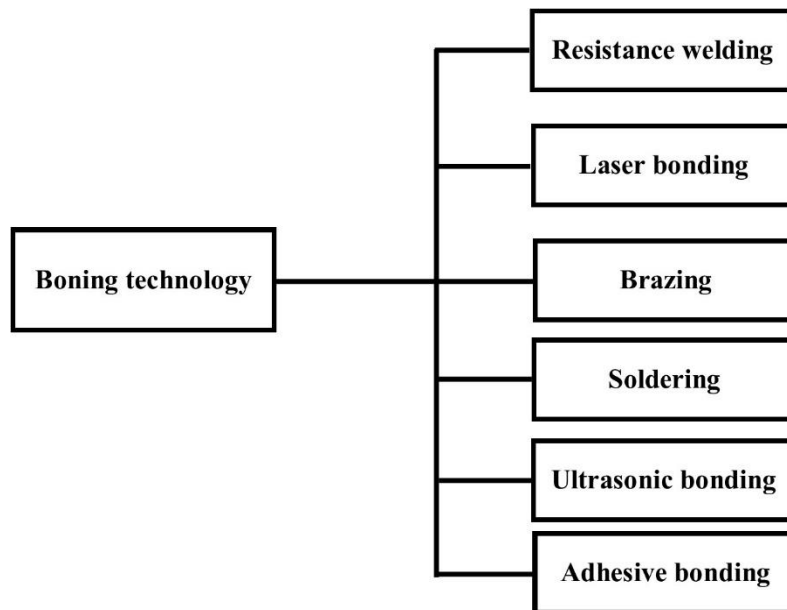


Figure 1.5 Bonding technology used in the electronics industry [14].

As we mentioned, the solder melts into the gap between the substrate and the base metal (non-joints such as electronic parts and substrates), and an intermetallic compound (IMCs) is formed between the solder and the base metal during soldering. This soldering process will be described in more detail using a simple soldering iron in Figure 1.6. The step is as follows [8].

- i) An oxide is covered on the surface of the base metal,
- ii) When the flux is applied and heated, the oxide film is removed,
- iii) As the solder is wetted to the base metal, the interatomic movement occurs between the base metal and the solder,
- iv) Bonding between the atoms moved leads to the formation of intermetallic compound and solidification, and the soldering is completed.

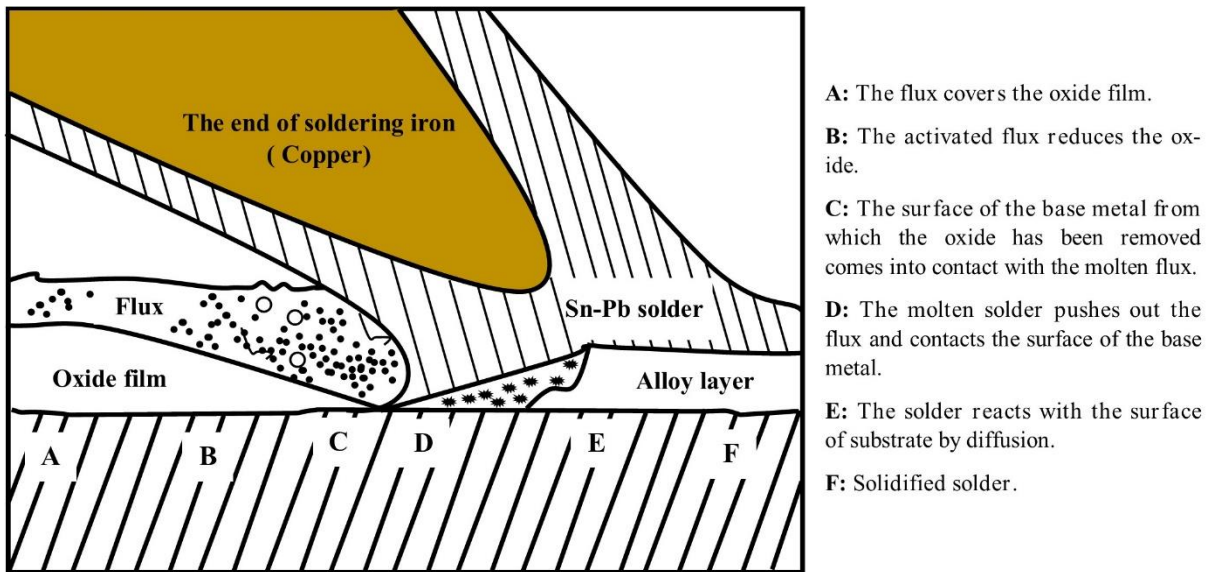


Figure 1.6 Schematic of soldering process [8].

The factors that affect the soldering performance of electronic components can be roughly divided into material factors and process factors. These factors are described in more detail as follows [8].

First, material factors are solder, flux, base metal, and substrate.

The base metal refers to an electronic component or a substrate to be bonded at the time of soldering. In the electronic industry, plating or a metal layer (metallizing) is usually formed on the surface of the base metal so that soldering easily occurs. Generally, Sn-37%Pb solder was used for soldering in the past time. However, recently lead-free solders have begun to be applied due to various environmental regulations.

Second, the process factors can be divided into the work factors and directly related to the soldering, pre-heating, pretreatment. The most important factors of the soldering process are the heating curve and the method (reflow, wave soldering, etc.). And the heating temperature and time including preheating are also important. In addition, about 60% of the defects that occur in soldering process is material design defects. And it should be considered the cleanliness of materials.

1.2.2 Harmfulness and Regulations of lead (Pb)

Sn-Pb based solder had been used as the most effective bonding material for electronic devices for a long time. However, when disposing of electronic devices using solder, lead (Pb) components contained in the solder have been eluted due to acid rain, resulting in contamination of groundwater [15]. When the contaminated groundwater is absorbed into the human body, it is pointed out as an environmental pollutant because it has detrimental effects on the human body such as lowering of intelligence and deterioration of vital function [16]. Fig. 1.7 shows a process of how to effect on human health of lead toxicity in PCBs.

Lead contained in Sn-Pb based solder is known to be eluted by the following reaction [15]. In other words, the lead in the solder is oxidized to PbO in the atmosphere and then eluted with PbSO₄ and Pb(NO₃)₂ by sulfuric acid (H₂SO₄) or nitric acid (HNO₃) contained in the acid rain.

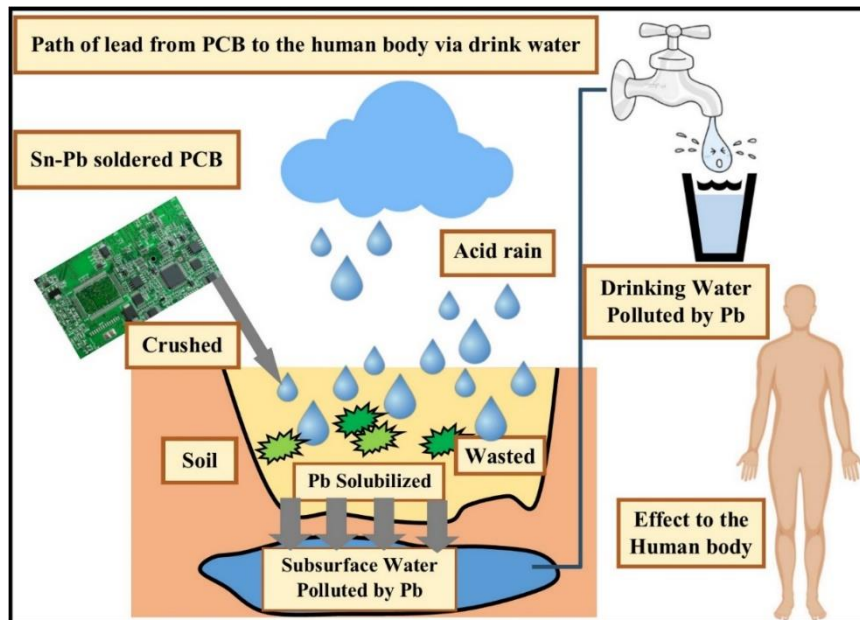


Figure 1.7 A schematic to show lead toxicity in (PCBs) effects on human health (Napp D. 1995) [15].

Due to these problems, starting with a review of the regulations on the use of lead in electrical and electronic solder in the United States in 1990, research on lead-free solders has been proceeding around the world [17]. Research related to the development of lead-free solders was first conducted in the United States with the National Center for Manufacturing Sciences (NCMS) project (1992-1996) [17]. In 1997, the National Center for Manufacturing Sciences Lead Free Solder Project carried out by a consortium of 11 industrial corporations, academic institutions, and national laboratories completed its four-year program to identify and evaluate alternatives to eutectic tin-lead solder. Participating organizations were AT&T/Lucent Technologies, the Navy's Electronics Manufacturing Productivity Facility (EMPF), Ford Motor Company, GM/Delco Electronics, GM/Hughes Aircraft, the National Institute for Standards and Technology (NIST), Rensselaer Polytechnic Institute (RPI), Rockwell International, Sandia National Laboratories, Texas Instruments and United Technologies/Hamilton Standard. The goal of the project was to determine whether safe, reliable, non-toxic, and cost-effective substitutes exist for lead-bearing solders in electronics manufacturing. And in Europe with the Improved Design Life and Environmentally Aware Manufacturing of Electronics Assemblies by Lead-Free Soldering (IDEALS) project (1996-1999) [18]. On July 16, 2001, in a move aimed at accelerating the use of lead-free packages and stimulating the further development of lead-free technologies, three major European semiconductor manufacturers Philips Semiconductors, Infineon Technologies AG and STMicroelectronics unveiled their proposal for the world's first standards for defining and evaluating lead-free semiconductor devices. Their joint document defines the requirements for “green packages”, lead-free solderability tests, moisture sensitivity levels and whisker-free terminations. It is considered to be ahead of Europe and the United States on the basis of lead-free solder and application technology in Japan [19].

As we mentioned, lead (Pb) is toxic when ingested. In addition, The waste disposal of Pb and reclamation may be detrimental to the environment. Thus, reduction in Pb use will eventually be regulated. The European Union (EU) directives on WEEE dictate that products sold in the EU must be lead-free from July 1, 2006. And the EU directives on RoHS dictate that restricts the use of lead (Pb), mercury (Hg), cadmium (Cd), chromium (Cr^{6+}), Polybromide Biphenyl (PBB), and Polybrominated Diphenyl Ether) PBDE in electronics and electrical equipment as of July 1, 2006 [20, 21]. Thus, major electronics companies have moved forward

with developing products with lead-free solder from IT devices such as tablet PC and smart phone to white goods such as TV and refrigerator in the world.

1.2.3 Lead-free solders

There are several definitions of lead-free. In case of products that contain no lead at all, or normally it defined as lead-free when there are less than 1000 ppm of total product weight [13]. Electronics companies Philips Semiconductor, Infineon Technologies and STMicroelectronics defined lead-free components as lead-free, with less than 0.1% lead content in individual materials rather than in the entire package in July 2001 [22]. JEDEC has defined a solid state device with less than 0.2% weight on lead for each material in November 2001 [23]. NEMI defined a leadless solder joint with less than 0.2% Lead-free or deliberately no lead in January 2002 [24].

There are some considerations when choosing solder for lead-free products. For example, reasonable price, low melting point, short temperature range where the liquid to solid changes, whether the component and board level preparation is appropriate, various finishes of the board or component, and good wettability, good material properties such as electrical / thermal conductivity, good mechanical properties such as strength and ductility, good reliability characteristics such as fatigue, creep and corrosion resistance, whether they can be well integrated with parts including lead. There are some alternative lead-free solders when considering the above things. The following is a list of the 6 most commonly used lead-free solders (Sn / Cu, Sn / Ag, Sn / Ag / Cu, Sn / Ag / Bi, Sn / Ag / Cu / Sb, and Sn / Zn / Bi).

i) Sn / Cu

One of the three lead-free solders recommended by the National Electronic Manufacturing Initiative (NEMI), with a possible composition of Sn-0.7Cu solder. Especially suitable for wave soldering, low cost, good combination on almost all plated surface finish. The Cu_6Sn_5 IMCs particles dispersed in the Sn-matrix and act a role in preventing fatigue crack propagation. The problem is relatively high melting

temperature of 227 °C. The tensile and yield strength of Sn-0.7Cu are lower than Pb-based solder [25].

ii) Sn / Ag

Sn-Ag based solder has been applied to industry fields of automobile, aircraft and mobile device. And Ag₃Sn IMCs particles dispersed in Sn-matrix. Sn-3.5Ag is representative composition and melting temperature is 221 °C. And good wettability, good combination on almost all plated surface finish. It is suitable for rework of Sn-Ag-Cu solder joints. However, Sn-Ag alloys also raises concerns about the high cost and toxicity of Ag [26].

iii) Sn / Ag / Cu

Sn-Ag-Cu solder alloy is the representative lead-free alloy of the electronics industry in modern society. Lots of research institutes have recommended this alloy such as NEMI and ITRI. The eutectic alloy has a melting temperature of 216 to 217 °C. The Ag₃Sn and Cu₆Sn₅ IMCs particles are in the Sn matrix, and dislocation movement can be prevented because the grain size is small. Therefore, the fatigue strength can be increased. Solder alloys include Sn-3.0Ag-0.5Cu (JEIDA's recommendation), Sn-3.5Ag-0.75Cu and Sn-3.9Ag-0.6Cu are the most popular compositions for lead-free solders. Good mechanical and thermal properties. However, high cost of Ag, high melting point, plasticity and fatigue properties deteriorate when the Cu / Ag content increases [27].

iv) Sn / Ag / Bi

Sn-3.5Ag-1.0Bi (T_m : 219 ~ 220 °C) and Sn-3.3Ag-4.7Bi (T_m : 210 ~ 215 °C) are the representative ternary alloys. Sn-3.5Ag-1.0Bi has good plasticity, wettability, melting point and fatigue resistance. Sn-3.3Ag-4.7Bi has a high melting point. However,

fatigue characteristics are improved 30 % to Sn-Pb solder. Bismuth dissolves and remains in a large area with residual stress, prevent the movement of dislocation. The problems are toxicity and stiffness of silver and bismuth. And the plasticity and fatigue properties are significantly degraded when the content of bismuth exceeds 5% [28].

v) Sn / Ag / Cu / Sb

Sn-2.5Ag-0.8Cu-0.5Sb (T_m : 217 °C) has some advantages such as good wettability and good mechanical properties. And the thermal and electrical conductivity are very similar with Sn-Pb solder. This is the lowest melting temperature in Sn-Ag-Cu based alloys. However, Sn-2.5Ag-0.8Cu-0.5Sb is also pointed out of disadvantages such as antimony content issue (< 1 wt.%) in Japan market, potential component thermal damage and high cost [29].

vi) Sn / Zn / Bi

Sn-8Zn-3Bi (T_m : 195 °C) has some advantages such as similar melting temperature to Sn-Pb alloy and low cost compared with other main alternatives. However, Sn-8Zn-3Bi is also pointed out of disadvantages such as drossing of Sn-Zn-Bi, corrosion potential and potential of weak joints fillet lifting in wave soldering. In a Zinc containing alloy system, oxidation occurs quickly and void formation is relatively high. However, bismuth is added to reduce this disadvantages [30].

1.2.4 Usage environment of lead-free solder

The requirement of solder joint performance is getting stringent in order to support the modern electronic devices. Especially for automobile, due to the harsh use environment where the under-hood temperature is much higher than other applications, the requirement on the solder joint performance is higher [31]. Moreover, these applications increased the challenges in selecting an appropriate solder alloy and bonding process. Besides in-automobile system, the effort of popularization of electric vehicles has further promoted the usage of electronic components in automobile industry. In view, the fact that this kind of system involves high

current and high temperature, conventional bonding process and materials (SAC Pb-free alloys) cannot fulfill the basic requirement [32]. With such high quantity of electronic components, the usage of solder as interconnect is also prospective. The selection of bonding process to fulfill the requirement of this sector will focus in meeting the specific criteria for manufacturing, reliability, toxicity, cost, and availability. Therefore, the bonding techniques such as TLPB and NPB are described in more detail as follows.

i) Transient liquid phase bonding (TLPB)

The initial TLP bonding is known as diffusion bonding. The TLP is a bonding method as filler metal in order to bond Ni, Fe, and Cu system alloys with using an element which declines a melting point. Basically, in the form of combining the concepts of brazing and diffusion bonding, Unlike the method of solid-phase diffusion bonding in which solid and solid are bonded in general, the TLP bonding is a liquid-phase diffusion bonding in which the metal is isothermal solidification from a liquid state to solid state at a bonding temperature. The filler metal which has a lower melting temperature than bonding temperature is melted at the bonding temperature and the element which declines melting temperature diffuse through the base metal through solid-liquid inter-diffusion and increase the melting temperature of bonding material by isothermal solidification. In the field of electronic material bonding, the TLP bonding is melted at a higher temperature than the bonding temperature through the changed composition [33-35], or an IMC is formed and isothermal solidification has occurred at the joints as shown in Fig. 1.8 [36]. For example, in case of the Sn–Bi solder with added Cu particles [37], Sn and Cu to react and form the Sn–Cu IMCs after TLP bonding. Fig. 1.9 shows that after solder is reflowed at 200 °C for 10min, peaks representing eutectic Sn–Bi and new melting event co-exist at 201 °C, and then disappeared the eutectic peak after reflowed at 200 °C for 50min. And DSC curves in Fig 1.9 indicated the new melting event which was increased by approximately 62 °C.

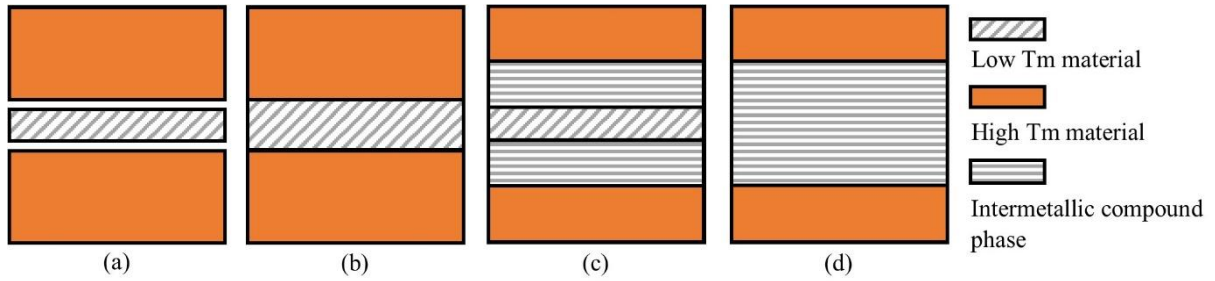


Figure 1.8 Schematically illustrates of design of (a) initial joint, (b) melting and wetting, (c) solid-liquid interdiffusion and (d) solidification for TLP bonding [36].

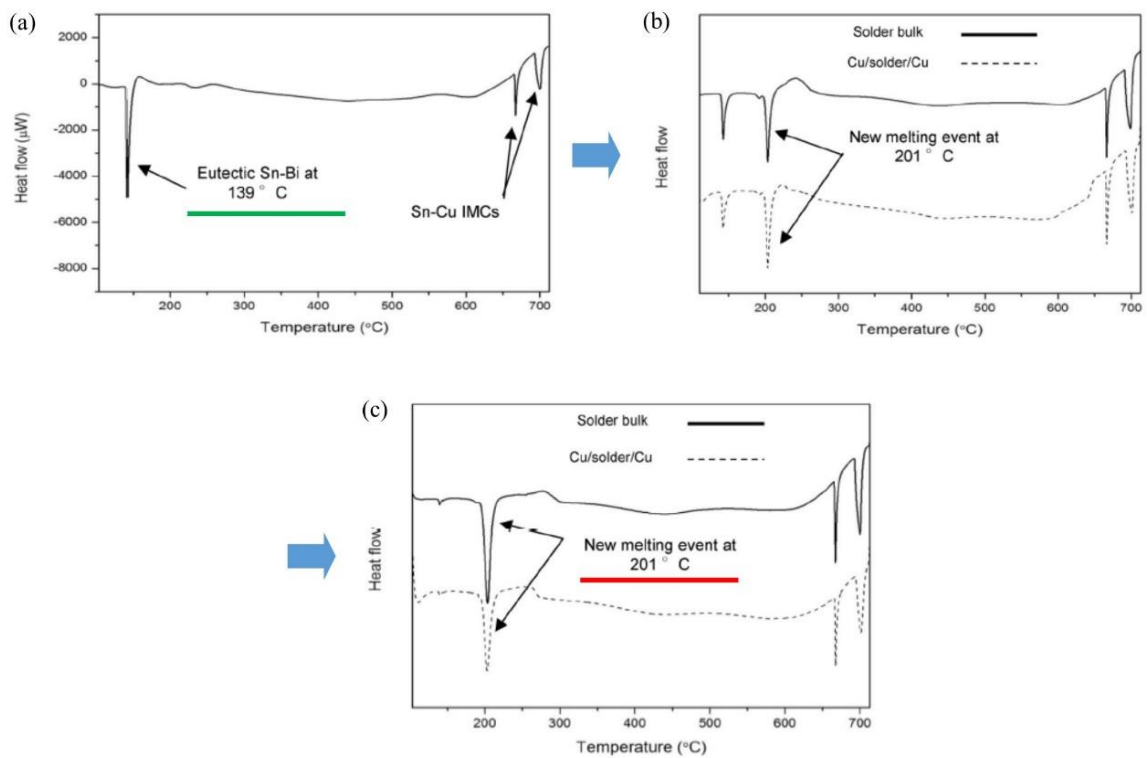


Figure 1.9 The DSC results of Sn-Bi-30Cu (a) before reflow (paste), (b) after reflow at 200 °C for 10 min, and (c) after reflow at 200 °C for 50 min [37].

ii) Nanoporous bonding (NPB)

Nanoporous bonding has received much attention as an alternative joining method to Pb-based soldering for high temperature electronic applications. For example, Ag nanoparticle bonding has still certain issues such as difficulties of in controlling the joining layer thickness and the occurrence of unexpected voids resulting from solvent evaporation [38]. Despite these disadvantages, the bonding of micro- and nano particles of Ag has a great promise as bonding process of the high temperature which has good electrical and thermal conductivity and low-temperature bondability [39]. Kim et al., Ag nanoporous bonding using thermos-compression bonder which applied pressure of 20 MPa at 200 °C and 400 °C indicated NPB shear strength was approximately 16.2 MPa and 27.0 MPa [40]. It was related with density of bonding layer. The Ag nanoporous bonding layers exhibit a dense and porous sandwich structure for all bonding temperatures, where the Ag nanoporous structures had partially collapsed, formed contacts with each other due to compression stress near the surface, and then densified.

The joint strength of nanoporous bonding (NPB) was closely related with the microstructure of the Ag layer and the fracture mode of the joint, and increased with increasing bonding temperature through the formation of strong interface and a coarsened Ag layer as shown in Fig. 1.10.

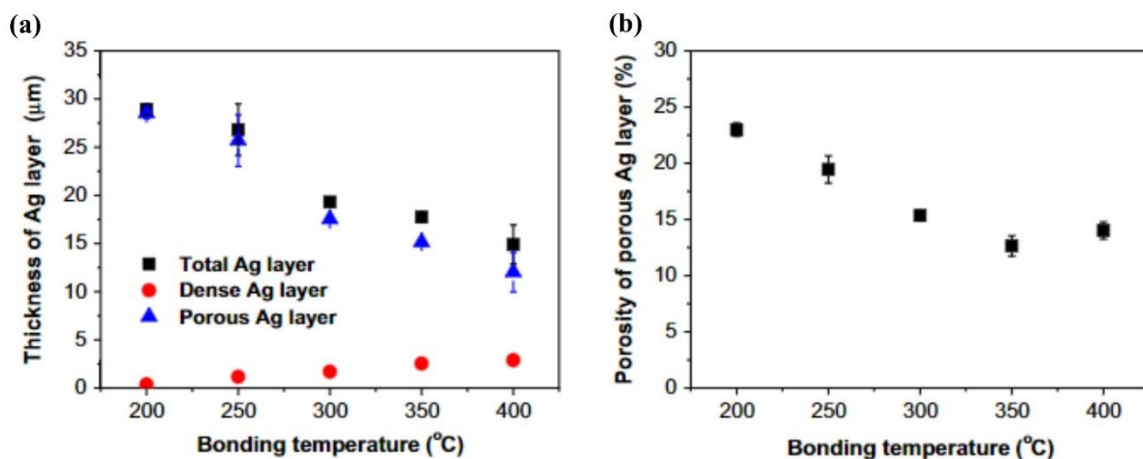


Figure 1.10 The variation of (a) thickness of total, dense and porous Ag layers and (b) the measured porosity of porous Ag layers [40].

1.3 Low temperature solder

As refer to JIS Z 3282: 2017 [41], The low-temperature solder has a solidus temperature below 150 °C. The representative binary lead-free solders satisfying these conditions include Sn-Bi and Sn-In. Their eutectic temperatures are about 139 and 118 °C, respectively [42, 43]. There are two reasons why the interest in low-melting temperature solder is getting bigger in recently as below:

First, the use of low temperature solder can improve the yield of double-sided packaging, which is gradually expanding in accordance with recent high-density packaging technique trends. In other words, it needed the development of low temperature solder for double-sided SMT which melts sufficiently without inducing melting of the high temperature solder used in the first reflow process in the second reflow process [44].

Second, it is necessary to improve the yield of the package stack process. In order to satisfy the manufacturing yield and long-term reliability of the package stacking process (Fig. 1.11) [45] which has been attracting attention as a highly integrated packaging technology in recent years, the warpage of the package should be minimized. In general, the warpage of the package is changed into a cup or a cone shape based on the bonding process temperature of the EMC (Epoxy Molding Compound) moulding (180 °C). Therefore, if the soldering process can be performed below the temperature, soldering is performed with minimized warpage of the package (Fig. 1.12) [46]. Therefore, the package stack process can be implemented under the most stable condition which minimizing short circuit and shape changes of the solder joint.

Thus, the types of typical low melting temperature solders that can satisfy the reasons as mentioned and their respective characteristics are summarized as below:

i) Sn / Bi

Sn-58Bi is a low-temperature solder alloy with a relatively low eutectic temperature of 139 °C. The spreading ratio of the Sn-Bi alloy is about 78 to 80% in the range of 220 to 250 °C, and the contact angle is about 18 °. Unlike other additive elements used in lead-free solder, Bismuth is formed large quantities of solid-solution in Sn-matrix. Bismuth in the solder is concentrated when solidifi-

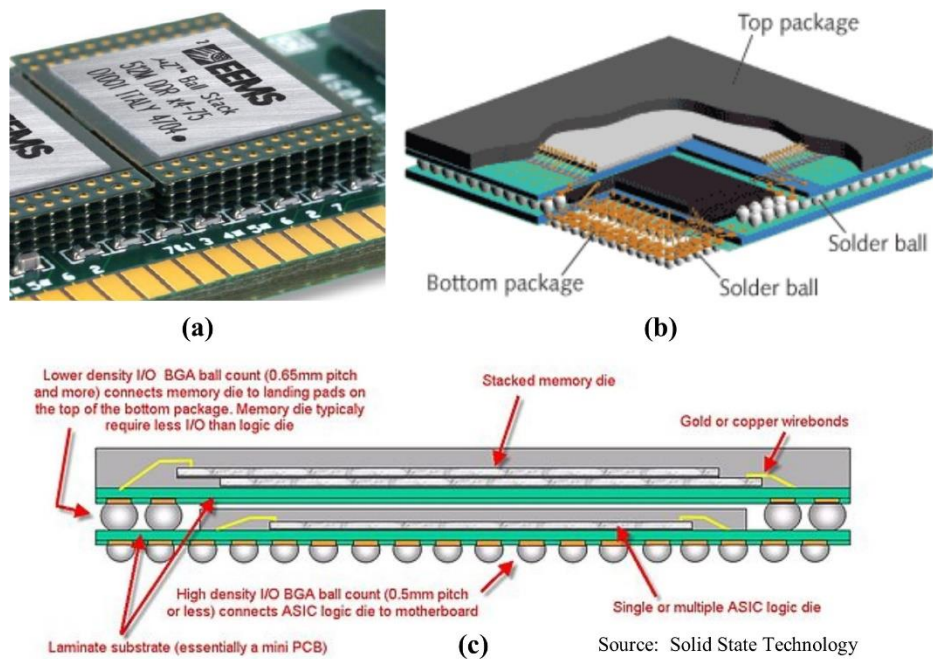


Figure 1.11 Stacked BGA. Package: (a) photo image, (b) and (c) cross-sectional schematic image [45].

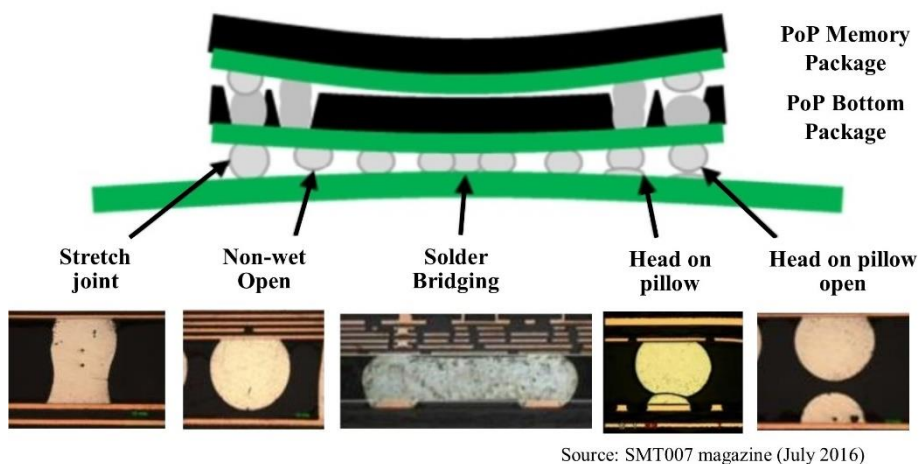


Figure 1.12 Typical SMT (Surface Mounting Technology) defect modes [46].

cation even if the Bi content is 21% or less. Hereby, the eutectic structure is likely to appear due to Bi segregation, and eutectic point (T_m : 139 °C) melting phenomenon occurs. Bismuth also reacts with the Sn-Pb plated layer on the surface of the electronic component, causing a phenomenon called "lift-off & fillet lifting" by cracks which do not bond properly between the Cu pad and the solder. The biggest problem in the practical use of the Sn-Bi alloy is the wide solidification range between 139 °C and 190 °C. This causes the solid / liquid phase area to increase considerably during soldering, and it appears as segregation and causes a lift-off when the solder solidifies [47].

And the Sn-Bi based solder reacts with the Cu pad to form Cu_3Sn and Cu_6Sn_5 compounds in turn from the Cu side toward the Sn-Bi bulk side like the Sn-Ag solder [48]. And previous other studies have confirmed that the interfacial bonding strength often deteriorates with increasing the thickness of the IMC layer under high-temperature conditions [49–51]. However, for some solder joints, the increasing thickness of the IMC layer is not the exclusive reason for the decrease of the bonding strength. For example, the Cu_3Sn layer often compromises the mechanical properties of solder joints due to the formation of voids at the interface. Besides, the Bi segregation at interfaces can also dramatically deteriorate the bonding strength [52–54]. Liu et al. [55] have reported that the Bi segregation at the Cu/ Cu_3Sn interface led to the sharp decrease in the mechanical properties of Cu/Sn–Bi couples after aging at 120 °C for 7 days, which greatly restrained the wide usage of Sn–Bi solder in the electronic packaging field.

Since the maximum solubility of Bi to Sn is as high as 21%, Bismuth may form a coarse precipitate at the time of solidification and adversely affect the mechanical properties. Therefore, in consideration of soldering characteristics, it is necessary to make the bismuth content of 5% or less, to disperse precipitates coarsely by alloying the third element.

ii) Sn / In

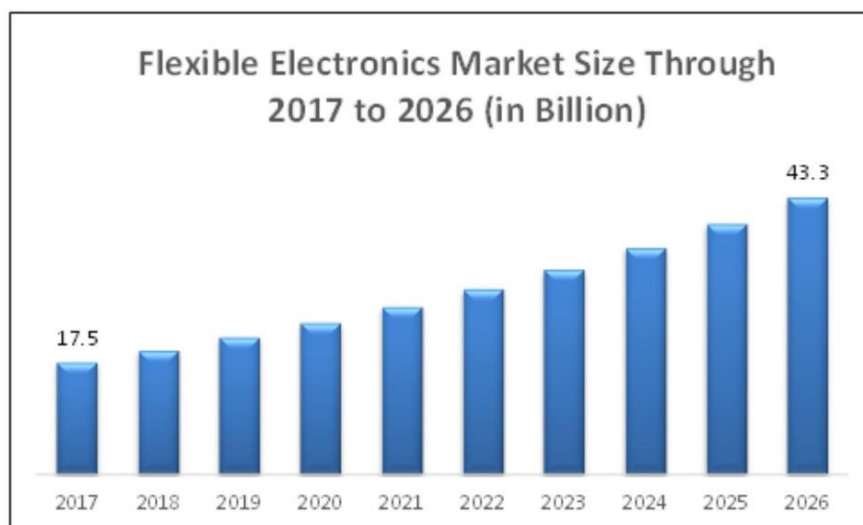
The Sn–In solder has a eutectic composition of Sn–50.9In and the eutectic temperature is 117 °C. And the melting point is lower than other alternative solders.

However, the composition mainly used for surface mounting is usually Sn–52In. The intermetallic compounds such as a β -phase of In-rich and a γ -phase of Sn-rich are produced in the Sn–In alloy system. Sn–In solder alloy forms an irregular eutectic that change to a fine-grained two phase mixture at high solidification rates. Sn-In solder has good ductility and wettability [56]. However, the cost is a disadvantage, indium is expensive. And Sn–In solder have not been studied as much yet.

1.4 Next-generation electronic devices by flexible substrates.

1.4.1 Flexible electronics markets growth

Refer to the reports of Maximize Market Research. The market for printed, flexible and organic electronics will grow from \$17.5 Billion in 2017 to \$43.3 billion in 2026 as shown in Fig. 1.13 [57]. The majority of that is OLEDs (Organic Light-Emitting Diode); printed biosensors; and printed conductive ink (used for a wide range of applications, but predominately PV). On the other hand, stretchable electronics, logic and memory, flexible batteries and capacitive sensors are much smaller segments but with strong growth potential as shown in Fig. 1.14 [58].



Source: Maximize Market Research

Figure 1.13 Global Flexible Electronics Market Size and Forecast, 2017-2026 [58].

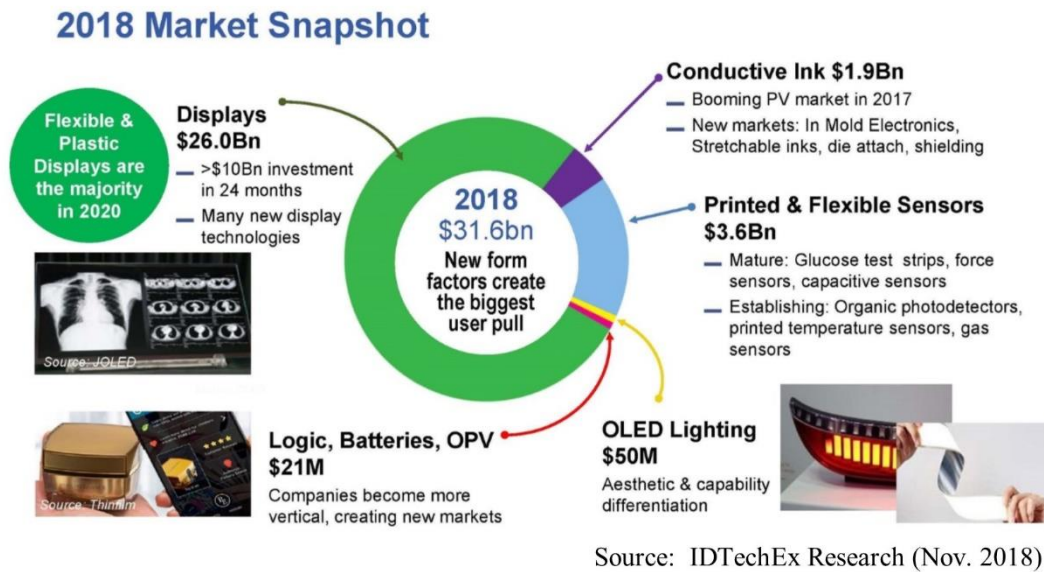


Figure 1.14 Analysis of flexible electronics market by product, 2018 [58].

1.4.2 Materials for Flexible substrate

Flexible circuit means technology for building electronic circuits by depositing electronic devices on flexible substrates [59]. The substrates used in flexible electronics need meet various requirements such as thermal properties, chemical properties, dimensional stability, mechanical properties, surface flatness & roughness and so on. thus, Polyimide (PI) and Polyethylene terephthalate (PET) are the traditional suitable materials to make up the flexible substrate.

1) Polyimide (PI)

Polyimide is synthesized by polymerizing with an aromatic dianhydride and an aromatic diamine. The most notable characteristics of polyimide are its excellent heat resistance (T_g is between 360 °C and 410 °C) and excellent chemical resistance (no known organic solvents for the film). It also has good flexibility and electrical properties. However, the main problems of polyimide are high moisture absorption on 4% after 24 hours at 23°C, which result in a poor dimensional stability [60].

2) Polyethylene terephthalate (PET)

PET is a plastic resin and the most common type of polyester. It can be obtained through the polycondensation of ethylene glycol and terephthalic acid. PET is often used in PCB (printed circuit board) for a large circuit which is not requiring soldering because of the lack of heat resistance ($T_g = 80\text{ }^\circ\text{C}$) [61].

The use of flexible substrates will significantly reduce the weight of flat panel display and provide the ability to conform bend or roller display into any shape as shown in Fig. 1.15 [62]. PI and PET substrate might be a suitable candidate for transparent flexible substrates in the flat panel display or other electronic applications.



Source: INTECH open science (2015)

Figure 1.15 Roadmap of flexible substrates technology and products [62].

1.5 Motivation of research

Modern electronic devices are smaller, lighter, thinner, and more energy-efficient than previous products [63], and flexible electronics are a representative technological innovation in the electronics industry. Flexible and wearable electronics are emerging technologies with significant potential. Recently, the market for flexible electronics boomed when foldable smartphones and rollable displays went on sale [59]. According to IDTechEX, the market for flexible electronics approached \$31.6 billion in 2018. The forecasted market size is expected to be \$77.3 billion in 2029 [57]. These market trends show how the market for flexible electronics will grow in the foreseeable future. As the market grows, flexible and bendable substrates are attracting more attention. Polypropylene (PP) and poly-(methyl methacrylate) (PMMA) are two of the materials attracting attention as next-generation substrates. And transparent PP and PMMA with high flexibility will be undoubtedly demanded in the future to fabricate such foldable display devices. However, these substrate materials have low melting temperatures below 170 °C [64, 65]. The temperature of the reflow process for regularly applying environmentally friendly Sn-based solder alloys is approximately 250 °C [66], e.g., Sn–3.0Ag–0.5Cu (217 °C) [67], Sn–3.5Ag (221 °C) [68], and Sn–0.7Cu (227 °C) [69]. In this case, PP and PMMA are subject to thermal damage during the reflow process. Therefore, Sn-based low-temperature alloys, such as Sn–Zn and Sn–Bi solder alloy systems, were proposed as an alternative. In particular, the eutectic Sn–8.8 mass% Zn (Sn–9Zn) and Sn–58 mass% Bi (Sn–58Bi) alloys have low melting temperatures of about 198 and 139 °C, respectively [70–74]. However, these melting temperatures are still too high for PP and PMMA substrates. Thus, it is necessary to develop filler metals which can be soldered at temperature below 100 °C to avoid thermal damage to the temperature-sensitive components in flexible electronic devices. In–xBi binary alloys is proposed as a candidate for low-temperature Pb-free solder alloys. Indium-based alloys exhibit low melting points, extreme softness, and ductility [75].

1.6 Purpose and outline of this study

This dissertation covers the alloying of In–xBi alloys, analyze the thermal and mechanical properties, microstructure, fracture surface characteristic and verification of the reliability of In–xBi alloys bonding joint under the thermal aging test.

In this chapter (Chapter 1), this chapter describes the objectives of the research, as well as a brief introduction to the soldering and alternative solder alloys for lead-free are also reviewed. And low temperature alloys are also introduced, on the basis of applying for the flexible substrate.

In *Chapter 2*, the fabrication of In-xBi alloys tensile specimen from In–Bi cast bar using alloying method is presented. The microstructure of In–Bi binary alloys and related mechanical properties as a function of indium content were also clarified.

In *Chapter 3*, the thermal aging test was conducted on In–Bi alloy specimens to evaluate the change of their morphologies, phase constitution and thermal property during aging.

In *Chapter 4*, the mechanical properties and fracture surface characteristics of In–Bi alloys under isothermal aging to test and analyze their thermal stability were investigated.

In *Chapter 5*, the joining properties of the In–Bi alloys by reflow is reported. And thermal aging tests are carried out, and the change in interface morphology and shear strength of the alloy joints are discussed.

In *Chapter 6*, Cu microparticles as the high-temperature material and mixed with In-Bi eutectic powder as the low-temperature material. And the influence of processing temperature, time and thermos compression conditions on joint strength, remelting temperature has been investigated. In addition, the interfacial microstructure between the filler metal and Cu substrate and particles were investigated

In *Chapter 7*, the results obtained in the present study are summarized, and suggestions for future works and presented.

References

- [1] <https://www.cleverism.com/understanding-device-market-desktop-tablet-mobile/>
- [2] Blodgett, Albert J., “Microelectronic packaging”, Scientific American, 249.1 (1983) 86–97.
- [3] Brown, W. D., “advanced electronic packaging: with emphasis on multichip modules”, 2nd edn, IEEE Press, Newyork, (1999).
- [4] Shubin, I., et al., “Novel packaging with rematable spring interconnect chips for MCM”, 59th Electronic Components and Technology Conference, IEEE, 2009.
- [5] Kang, Sung K., Peter Gruber, and Da-Yuan Shih, “An overview of Pb-free, flip-chip wafer-bumping technologies”, Jom 60.6 (2008) 66–70.
- [6] Sakai, Hiroyuki, et al, “A millimeter-wave flip-chip IC using micro-bump bonding technology”, 1996 IEEE International Solid-State Circuits Conference, Digest of Technical Papers, ISSCC, IEEE, (1996).
- [7] Mei, Zequn, Helen A. Holder, and Hubert A. Vander Plas., “Low-temperature solders”, Hewlett Packard Journal, 47 (1996) 91–98.
- [8] Jacobson, G. Humpston DM., “Principles of soldering and brazing”, ASM International, Materials Park, OH 128 (1993).
- [9] Turbini, Laura J., et al., “Examining the environmental impact of lead-free soldering alternatives”, IEEE Transactions on Electronics Packaging Manufacturing, 24.1 (2001) 4–9.
- [10] Nowak, Damian, et al., “Mechanical properties of SMD interconnections on flexible and rigid substrates”, Soldering & Surface Mount Technology, 28.1 (2016) 27–32.
- [11] <https://www.iso.org/standard/2386.html>
- [12] Tu. King-Ning, “Solder joint technology”, Vol. 117, New York: Springer, (2007) 4–7.
- [13] M. Abtew and G. Selvaduray, “Lead-free solders in microelectronics”, Materials Science and Engineering: R: Reports, 27(5-6) (2000) 95–141.

- [14] <https://chemical-materials.elsevier.com/new-materials-applications/iphone-teardown-home/>
- [15] Zoran Miric, Anton, and Angela Grusd, “Lead-free alloys”, *Soldering & Surface Mount Technology*, 10.1 (1998) 19–25
- [16] Landrigan, P. J., “Toxicity of lead at low dose”, *British journal of industrial medicine*, 46.9 (1989) 593
- [17] NCMS. Lead-free solder project final report, NCMS Report environmental hazard potential from Pb in solders carried 0401RE96, Michigan: National Center for Manufacturing Sciences, in electronic waste streams. Three strong lead-free solder (1997)
- [18] Harrison MR, Vincent JH. IDEALS: Improved design life and environmentally aware manufacturing of electronics assemblies by Cu near eutectic, Sn–Zn eutectic, and Sn–Bi eutectic lead-free soldering. In: Proc 12th Microelectronics and Packaging alloys. Among them, Sn–(3–4) wt% Ag–(0.5–0.9) wt% Conference, Cambridge: IMAPS Europe, (1999) 98–104
- [19] Gutowski, Timothy, et al., “Environmentally benign manufacturing: observations from Japan, Europe and the United States”, *Journal of Cleaner Production*, 13.1 (2005) 1–17.
- [20] Directive, E. C., “Directive 2012/19/EU of the European Parliament and of the Council of 4 July 2012 on waste electrical and electronic equipment, WEEE” *Official Journal of the European Union L*, 197 (2012) 38–71.
- [21] Puttlitz, Karl J., and George T. Galyon, “Impact of the ROHS directive on high-performance electronic systems. Part I need for lead utilization in exempt systems”, *Journal of materials science Materials in electronics*, 18.1-3 (2007) 331–346
- [22] Plumbridge, W. J., “Tin pest issues in lead-free electronic solders”, *Lead-Free Electronic Solders*, Springer, Boston, MA (2006) 307–318
- [23] Fukuda, Yuki, Paul Casey, and Michael Pecht, “Evaluation of selected Japanese lead-free consumer electronics”, *IEEE Transactions on Electronics Packaging Manufacturing*, 26.4 (2003) 305–312
- [24] Rao, Srinivas, Jasbir Bath, and Harjinder Ladhar, “Lead-free manufacturing”, *Lead-Free*

Electronics (2006) 101–138

- [25] Osório, Wislei R., et al., “Microstructure, corrosion behaviour and microhardness of a directionally solidified Sn–Cu solder alloy” *Electrochimica Acta*, 56.24 (2011) 8891–8899
- [26] Yang, Wenge, Robert W. Messler, and Lawrence E. Felton, “Microstructure evolution of eutectic Sn-Ag solder joints”, *Journal of Electronic Materials*, 23.8 (1994) 765–772
- [27] Lehman, L. P., et al., “Growth of Sn and intermetallic compounds in Sn-Ag-Cu solder” *Journal of Electronic Materials*, 33.12 (2004) 1429–1439
- [28] Vianco, P. T., and J. A. Rejent, “Properties of ternary Sn-Ag-Bi solder alloys: Part I—Thermal properties and microstructural analysis”, *Journal of electronic materials*, 28.10 (1999) 1127–1137
- [29] Chen, B. L., and G. Y. Li, “Influence of Sb on IMC growth in Sn–Ag–Cu–Sb Pb-free solder joints in reflow process” *Thin Solid Films*, 462 (2004) 395–401
- [30] Zhou, Jian, Yangshan Sun, and Feng Xue, “Properties of low melting point Sn–Zn–Bi solders”, *Journal of alloys and compounds*, 397. 1-2 (2005) 260–264
- [31] Weng, Wayne Ng Chee, “Evolution of Pb-Free Solders” *Recent Progress in Soldering Materials*, IntechOpen, (2017) 93–95
- [32] Zhu, Ninghui, “Thermal impact of solder voids in the electronic packaging of power devices”, *Fifteenth Annual IEEE Semiconductor Thermal Measurement and Management Symposium (Cat. No. 99CH36306)*. IEEE, (1999)
- [33] MacDonald, W. D., and T. W. Eagar, “Transient liquid phase bonding” *Annual review of materials science*, 22.1 (1992) 23–46.
- [34] Welch, Warren, et al., “Transient liquid phase (TLP) bonding for microsystem packaging applications” *The 13th International Conference on Solid-State Sensors, Actuators and Microsystems, Digest of Technical Papers, TRANSDUCERS'05.*, Vol. 2. IEEE, 2005.
- [35] Sharif, Ahmed, Chee Lip Gan, and Zhong Chen, “Transient liquid phase Ag-based solder technology for high-temperature packaging applications” *Journal of Alloys and Compounds*, 587 (2014): 365–368
- [36] Bosco, N. S., and F. W. Zok, “Critical interlayer thickness for transient liquid phase

- bonding in the Cu–Sn system”, *Acta Materialia*, 52.10 (2004): 2965–2972
- [37] Mokhtari, Omid, and Hiroshi Nishikawa, “Transient liquid phase bonding of Sn–Bi solder with added Cu particles” *Journal of Materials Science: Materials in Electronics*, 27.5 (2016) 4232–4244
- [38] Suganuma, Katsuaki, and Jinting Jiu, “Advanced bonding technology based on nano-and micro-metal pastes” *Materials for Advanced Packaging*, Springer, Cham, (2017) 589–626
- [39] Kim, Min-Su, et al., “Reliability of Ag Nanoporous Bonding Joint for High Temperature Die Attach under Temperature Cycling”, *Materials Transactions*, 57.7 (2016) 1192–1196
- [40] Kim, Min-Su, and Hiroshi Nishikawa, “Silver nanoporous sheet for solid-state die attach in power device packaging” *Scripta Materialia*, 92 (2014) 43–46
- [41] <https://www.jisc.go.jp/app/jis/general/GnrJISSearch.html>, JIS Z 3282: 2017
- [42] Mei, Zequn, and J. W. Morris, “Characterization of eutectic Sn–Bi solder joints” *Journal of Electronic Materials*, 21.6 (1992) 599–607
- [43] Morris, J. W., JL Freer Goldstein, and Z. Mei, “Microstructure and mechanical properties of Sn–In and Sn–Bi solders” *JOM* 45.7 (1993) 25–27
- [44] Josifović, Ivan, Jelena Popović-Gerber, and Jan Abraham Ferreira, “New Double-Sided SMT Power Inductor”, *IEEE Transactions on Industry Applications*, 49.4 (2013) 1637–1648
- [45] Horibe, Akihiro, et al., “Inter chip fill for 3D chip stack” *Transactions of The Japan Institute of Electronics Packaging*, 2.1 (2009) 160–162
- [46] Sun, Peng, et al., “Warping reduction of package-on-package (PoP) module by material selection & process optimization”, 2008 International Conference on Electronic Packaging Technology & High Density Packaging, IEEE (2008) 1–6
- [47] Suganuma, Katsuaki, “Advances in lead-free electronics soldering”, *Current Opinion in Solid State and Materials Science*, 5.1 (2001) 55–64
- [48] Miao, Hui-Wei, and Jenq-Gong Duh, “Microstructure evolution in Sn–Bi and Sn–Bi–Cu solder joints under thermal aging” *Materials chemistry and physics*, 71.3 (2001) 255–271

- [49] Li, J. F., et al., “Interfacial reactions between molten Sn–Bi–X solders and Cu substrates for liquid solder interconnects” *Acta Materialia*, 54.11 (2006) 2907–2922
- [50] Yang, Q. L., and J. K. Shang, “Interfacial segregation of Bi during current stressing of Sn-Bi/Cu solder interconnect”, *Journal of electronic materials*, 34.11 (2005) 1363–1367
- [51] Vianco, P. T., and J. A. Rejent, “Properties of ternary Sn-Ag-Bi solder alloys: Part I—Thermal properties and microstructural analysis”, *Journal of electronic materials*, 28.10 (1999) 1127–1137
- [52] Yang, Q. L., and J. K. Shang, “Interfacial segregation of Bi during current stressing of Sn-Bi/Cu solder interconnect” *Journal of electronic materials*, 34.11 (2005) 1363–1367
- [53] Lee, Chang-Bae, et al., “The effect of Bi concentration on wettability of Cu substrate by Sn-Bi solders” *Materials Transactions*, 42.5 (2001) 751–755
- [54] Yoon, Jeong-Won, Chang-Bae Lee, and Seung-Boo Jung, “Interfacial reactions between Sn-58 mass% Bi eutectic solder and (Cu, electroless Ni-P/Cu) substrate”, *Materials transactions*, 43.8 (2002) 1821–1826
- [55] Liu, P. L., and J. K. Shang, “Segregant-induced cavitation of Sn/Cu reactive interface”, *Scripta materialia*, 53.6 (2005) 631–634
- [56] Sommadossi, S., et al.. “Mechanical properties of Cu/In-48 Sn/Cu diffusion-soldered joints”, *Zeitschrift für Metallkunde*, 93.6 (2002) 496–501
- [57] Flexible, Printed and Organic Electronics Forecasts 2019–2029: Players & Opportunities; IDTechEx: Boston, MA, USA, October 2019.
- [58] Foldable OLEDs: Introduction and Market Status. Available online: <https://www.oled-info.com/foldableoleds>
- [59] Wong, William S., and Alberto Salleo, eds., “Flexible electronics: materials and applications”, Springer Science & Business Media, Vol. 11. (2009) 11–13
- [60] Hsiao, Yu-Sheng, et al., “Chemical formation of palladium-free surface-nickelized polyimide film for flexible electronics”, *Thin Solid Films*, 516.12 (2008) 4258–4266
- [61] Sun, Lei, et al., “Flexible high-frequency microwave inductors and capacitors integrated on a polyethylene terephthalate substrate”, *Applied Physics Letters*, 96.1 (2010) 013509

- [62] Bardsley, James Norman, “International OLED technology roadmap” IEEE Journal of selected topics in quantum electronics, 10.1 (2004) 3–9
- [63] MacDonald, William A., et al., “Latest advances in substrates for flexible electronics”, Journal of the Society for Information Display, 15.12 (2007) 1075–1083
- [64] Kalifa, P.; Chéné, G.; Gallé, C., “High-temperature behaviour of HPC with polypropylene fibres: From spalling to microstructure”, Cem. Concr. Res., 31 (2001) 1487–1499
- [65] Koleva, M., “Poly(methylmethacrylate) (PMMA)”, CAEDS Inject. Mould. Mater., 2 (2014) 1–5
- [66] Chowdhury, M.M.R.; Hoque, M.A.; Ahmed, S.; Suhling, J.C.; Hamasha, S.; Lall, P., “Effects of mechanical cycling on the microstructure of SAC305 lead free solder”, In Proceedings of the 2018 17th IEEE Intersociety Conference on Thermal and Thermomechanical Phenomena in Electronic Systems, San Diego, CA, USA (2018) 1324–1332
- [67] Gain, A.K.; Zhang, L.C.; Chan, Y.C., “Microstructure, elastic modulus and shear strength of alumina (Al₂O₃) nanoparticles-doped tin–silver–copper (Sn–Ag–Cu) solders on copper (Cu) and gold/nickel (Au/Ni)-plated Cu substrates”, J. Mater. Sci. Mater. Electron., 26 (2015) 7039–7048
- [68] Gain, A.K.; Zhang, L., “Thermal aging effects on microstructure, elastic property and damping characteristic of a eutectic Sn–3.5Ag solder” J. Mater. Sci. Mater. Electron., 29 (2018) 14519–14527
- [69] Gain, A.K.; Zhang, L.; Quadir, M.Z., “Thermal aging effects on microstructures and mechanical properties of an environmentally friendly eutectic tin-copper solder alloy”, Mater. Des., 110 (2016) 275–283
- [70] Sukanuma, K.; Kim, K.-S., “Sn-Zn Low Temperature Solder. In Lead-Free Electronic Solders”, Springer, Boston, MA, USA, (2007) 121–127
- [71] Mei, Z.; Morris, J.W., “Characterization of eutectic Sn-Bi solder joints” J. Electron. Mater., 21 (1992) 599–607
- [72] Mokhtari, O.; Nishikawa, H., “Correlation between microstructure and mechanical

properties of Sn–Bi–X solders”, *Mater. Sci. Eng. A.*, 651 (2016) 831–839

[73] Mokhtari, O.; Nishikawa, H., “Effects of In and Ni addition on microstructure of Sn-58Bi solder joint”, *J. Electron. Mater.*, 43 (2014) 4158–4170

[74] Mokhtari, O.; Zhou, S.; Chan, Y.C.; Nishikawa, H., “Effect of Zn addition on interfacial reactions between Sn-Bi solder and Cu substrate”, *Mater. Trans.*, 57 (2016) 1272–1276

[75] Hiren R. Kotadia, Philip D. Howes, Samjid H. Mannan, “A review: on the development of low melting temperature Pb-free solders”, *Microelectron. Reliab.*, 54 (6–7) (2014) 1253–1273

Chapter 2

Basic properties of In–Bi alloys

2.1 Introduction

The basic properties of materials describe their melting, mechanical and fracture characteristics. The melting properties of the In–Bi alloys were measured by differential scanning calorimetry (DSC). And the melting behaviors of the In–Bi alloys were determined using a typical onset-intercept method which means fusion start temperature [1]. The mechanical properties of materials describe relations between stresses acting in the material and the respective deformation. The ultimate tensile strength (UTS) which presents the maximum strength in the engineering stress-strain curve, when a neck starts to develop in the material during tension. And the strain, increases with the applied load or the stress, by the value of Young's modulus as long as loading is within the elastic limit [2]. The fracture surface morphology indicates the identify the crack origin location and to determine a crack propagation mechanism. the information obtained from the location, orientation, extent of cracking, and fracture surface morphology use to determine a root cause for the failure [3]. Therefore, in this chapter, In–Bi alloys with melting temperatures approximately 80 °C were selected and their basic material properties such as melting temperature, microstructure and

mechanical properties after tensile testing were evaluated to understand the characteristics of In–Bi alloys.

2.2 Experimental

2.2.1 Fabrication of In–Bi alloys

In–50 mass% Bi, In–40 mass% Bi, In–33.7 mass% Bi, and In–30 mass% Bi having a liquidus temperature of approximately 80 °C on the In–Bi binary phase diagram, as shown in Fig. 2.1 [4]. The liquidus temperature of In–50Bi is 89.5 °C, the liquidus temperature of In–40Bi is 89.5 °C, the eutectic temperature of In–33.7Bi is 72.7 °C and The liquidus temperature of In–30Bi is 89.5 °C [4]. In–33.7Bi is a eutectic composition, In–50Bi and In–40Bi are hypoeutectic composition, and In–30Bi is hypereutectic composition. The alloys were produced by pure indium (99.99%) and pure bismuth (99.99%) purchased from Nilaco Co. (Tokyo, Japan). Each alloy was melted in a furnace at 500 °C for 5 h before being casted in a steel mold. Bulk specimens were prepared for the tensile test as well as for microstructure analysis. The molten solder in graphite crucible was casted in a steel mold to form samples of approximately 50 mm × 10 mm × 5 mm in size. The alloying process was performed in air, and the molten solder was stirred frequently to ensure a homogeneous alloy. Further, the prepared samples were cooled at a rate of 4.5 °C/s to 5.0 °C/s.

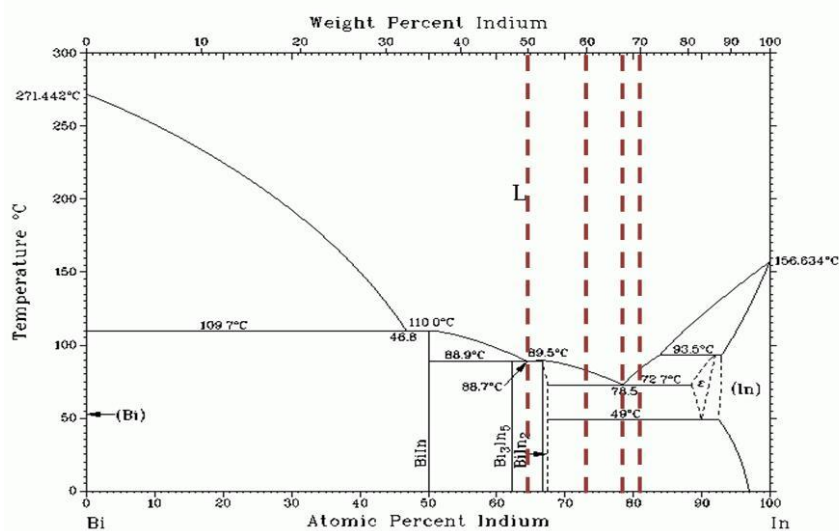


Figure 2.1 Phase diagram of In–Bi binary system [4].

2.2.2 Microstructures, melting temperatures, and elemental analysis

Samples were sectioned by a fine cutter. After that, the bulk samples were mounted on epoxy and hardener. The mounted samples were mechanically polished using SiC paper until # 2000 and then polished with two grades of DP-spray P (1 μm and 3 μm) and final polishing was performed using an OPS solution. The polished samples were immersed in pure ethanol and ultrasonically cleaned for 5 min. Elemental mapping of the microstructure was conducted by an electron probe microanalyzer (EPMA, JXA-8530F, JEOL). The phase constitution of each sample was measured by X-ray diffractometer (XRD, Ultima IV, Rigaku) with Cu $K\alpha$ radiation ($\lambda=1.5405 \text{ \AA}$) at an accelerating voltage of 40 kV. The diffracted beam was scanned in steps of 0.02° across a 2θ range of 20° - 80° , with a scan rate of 2° min^{-1} . The Pearson's crystal data powder diffraction file cards, including #533520 for In, #1401494 for Bi, #1400714 for BiIn, #1300118 for BiIn₂ and #534483 for Bi₃In₅, were used as references for the identification of diffraction pattern. Quantitative phase analysis was conducted by means of the reference intensity ratio method using the PDXL software provided by Rigaku. The melting properties of the In–Bi alloys were measured by differential scanning calorimetry (DSC, DSC7020, Hitachi). All samples for DSC were approximately 8.0 mg and used an Al pan / cover assembly. The heating from 50 °C to 150 °C was controlled at a rate of approximately 10 °C / min, and the measurement was repeated three times. The melting behaviors of the In–Bi alloys were determined using a typical onset-intercept method by JIS Z 3198-1 [1]. During all DSC runs, the samples were kept in an inert environment to prevent oxidation by flowing a constant flow of nitrogen gas.

2.2.3 Tensile test

The tensile strength and elongation of the In–Bi alloys were evaluated by a tensile test. Prior to the test, the specimens cast into bar-shaped steel molds were machined into a dumbbell-shape for tensile testing. The dumbbell-shaped machining is to observe the fracture that occurs in the middle of the sample [5]. For this reason, the dimensions of the gauge section of the tensile test specimen were 1.0-mm thick 2.0-mm wide, and 10-mm long, as shown in Fig. 2.2. Tensile tests were performed at room temperature on a universal testing machine (Autograph AG-X, Shimadzu) at a strain rate of $0.3 \text{ mm}\cdot\text{min}^{-1}$ to obtain tensile properties such as the

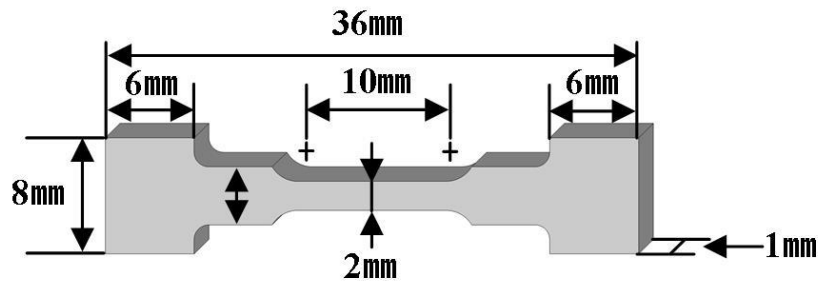


Figure 2.2 The schematic illustration of the tensile samples.

ultimate tensile strength (UTS) and elongation. All stress-strain characteristics of the In–Bi alloys are presented using an engineering stress-strain curve by assuming the equivalent level to the true stress-strain due to a small deformation range. Further, the necking and fracture surface of the alloys after tensile testing was examined using scanning electron microscopy (SEM, SU-70, Hitachi).

2.3 Results and Discussion

2.3.1 Phase constitution and microstructure of bulk In–xBi alloys

Fig. 2.3 shows the XRD patterns of In–Bi alloys. Bi_3In_5 was only detected in the In–50Bi alloy and BiIn_2 was detected in the In–40Bi, In–33.7Bi, and In–30Bi. It is confirmed that the In–Bi binary system contains stable intermediate phases: Bi_3In_5 , BiIn_2 , and an ϵ -phase. The Bi_3In_5 phase is generated in a peritectic reaction ($\text{Liquid} + \text{BiIn} \rightarrow \text{Bi}_3\text{In}_5$) at 88.9°C and forms a eutectic with BiIn_2 at approximately 64.6 mass% In at 88.7°C . The ϵ -phase is also generated in a peritectic reaction ($\text{Liquid} + (\text{In}) \rightarrow \epsilon$) between 93.5°C and 49°C , and forms a eutectic with BiIn_2 at 78.5 mass% In and 72.7°C . Further, a crystallized eutectic is formed: “ $\text{Liquid} \rightarrow \epsilon + \text{BiIn}_2$ ” ($T = 72.7^\circ\text{C}$, $X = 66.7 \text{ mass\% In}$) [4].

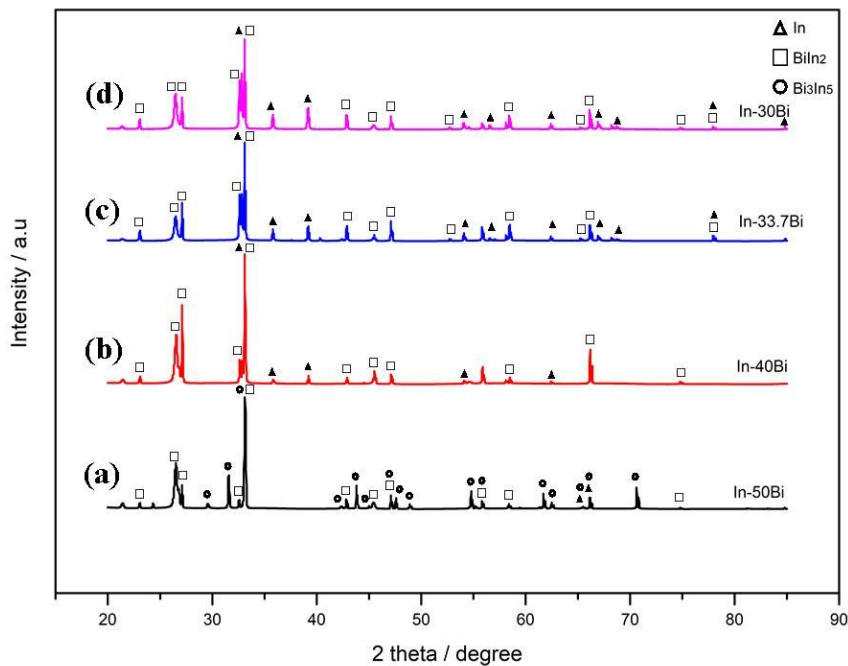


Figure 2.3 XRD patterns of In–Bi solders: (a) In–50Bi, (b) In–40Bi, (c) In–33.7Bi, (d) In–30Bi.

Fig. 2.4 shows the SEM images and EPMA mapping results of the In–Bi alloys after casting. In the SEM images, the gray, dark gray and bright regions represent In-rich phase and $\text{Bi}_x\text{--In}_y$ intermetallic compounds. The In–50Bi case appears as a peritectic reaction, where the liquid and the BiIn solid-solution phase are isolated by the Bi_3In_5 . The In–40Bi case appears as a hypoeutectic alloy. As a hypoeutectic alloy containing between 66.7 mass% In and 78.5 mass% (eutectic point) indium is cooled, the liquid begins to solidify at the liquidus temperature, producing the solid BiIn_2 phase. However, solidification is completed by going through the eutectic reaction. When the alloy is cooled below 72.7 °C, all remaining liquid goes through the eutectic reaction and transform to a lamellar mixture of In and BiIn_2 . For the microstructure shown in Fig. 2.4, the eutectic microconstituent surrounds the solid BiIn_2 that formed between the liquidus and eutectic temperatures. The eutectic microconstituent is continuous and the primary phase is dispersed between the colonies of the eutectic microconstituent. The In–33.7Bi case shows the eutectic composition. It has one eutectic reaction and the lowest melting temperature (solidification occurs at 72.7 °C) Above the temperature, the alloy is all liquid and,

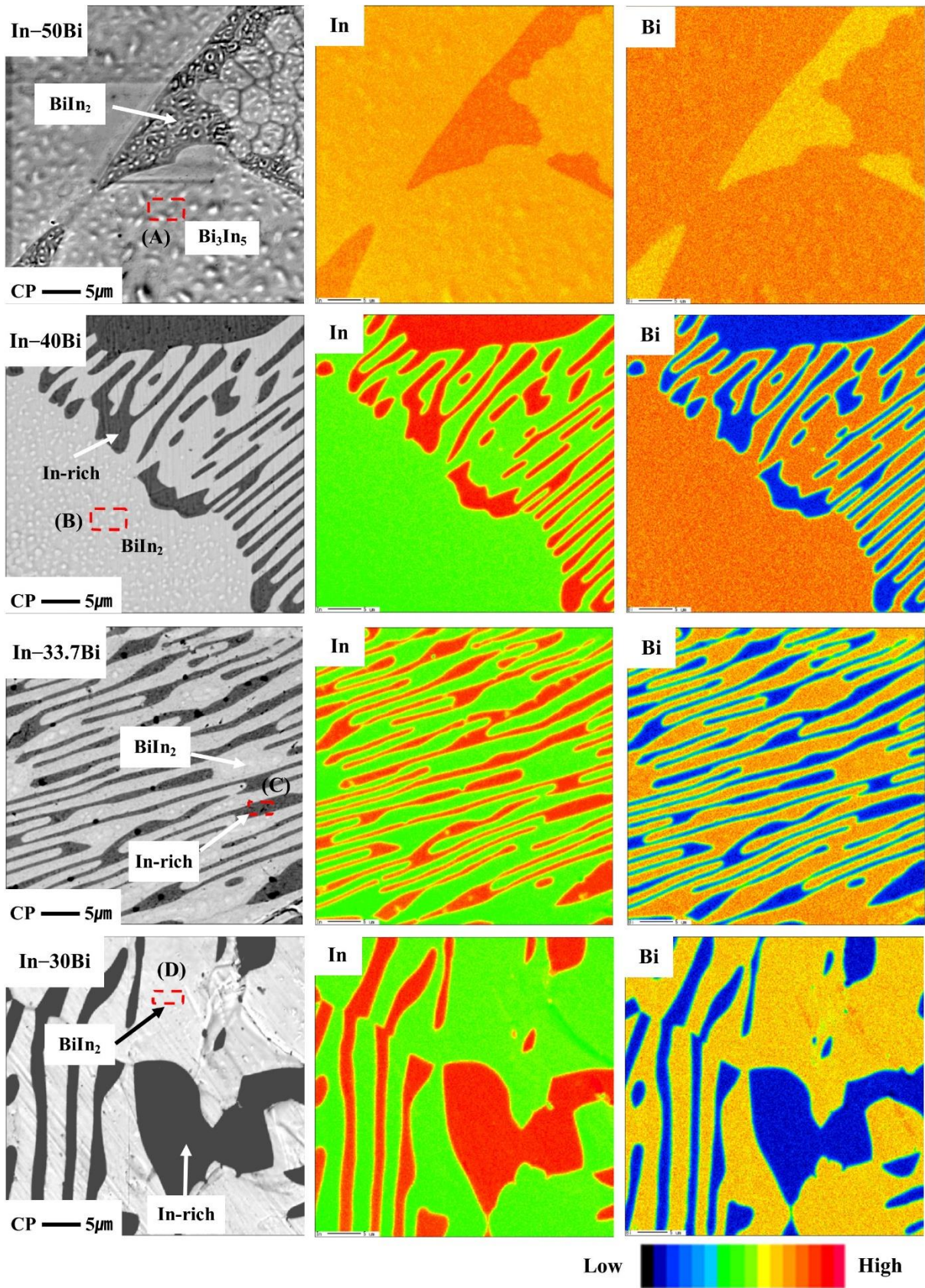


Figure 2.4 The EPMA mapping results of the In-Bi alloys.

Table 2.1 Quantitative analysis of points A, B, C and D in Fig. 2.4

Element	Point A (at.%)	Point B (at.%)	Point C (at.%)	Point D (at.%)
Indium	61.4	67.1	92.9	66.8
Bismuth	38.6	32.9	7.1	33.2
Total	100	100	100	100
Estimated phase	Bi_3In_5	BiIn_2	In-rich	BiIn_2

therefore, it should contain two solid solutions, In (ϵ -phase) and BiIn_2 , which are formed during the eutectic reaction. The solid In (ϵ -phase) and BiIn_2 grow from the liquid in a lamellar. The lamellar structure permits the indium and bismuth atoms to move through the liquid, in which diffusion is rapid, without having to move an appreciable distance. The In–30Bi case appears as a hypereutectic alloy. It has a eutectic structure owing to very close composition to the In–33.7Bi alloy.

In was detected in the In-rich phase, and Bi appeared to be included in the BiIn_2 and Bi_3In_5 . As shown in Fig. 2.4 and Table 2.1, the composition of the In–Bi IMCs and the In-rich phase were investigated using a quantitative analysis by the EPMA.

2.3.2 Melting properties

The melting properties of the In–Bi alloys were measured by a DSC. DSC analysis was carried out to confirm the fundamental melting behavior of the In–Bi alloys. The result of the test can be used to determine the reflow temperature which is approximately 20 °C to 30 °C higher than the melting temperature of the alloy [6]. DSC curves for all specimens are shown in Fig. 2.5 and summarized in Table 2.2. During the heating process of the DSC analysis, the In–Bi alloys showed a eutectic composition with a peak at 72.7 °C. The other composite alloys showed different curves. The onset temperature implies a fusion start [7]. The increase of indium amount in In–Bi alloys depressed their onset temperatures. This was an obvious indium-amount-dependent melting-point depression. However, three compositions of alloys except the In–50Bi had similar onset temperatures at 71.5 °C. This indicates a temperature

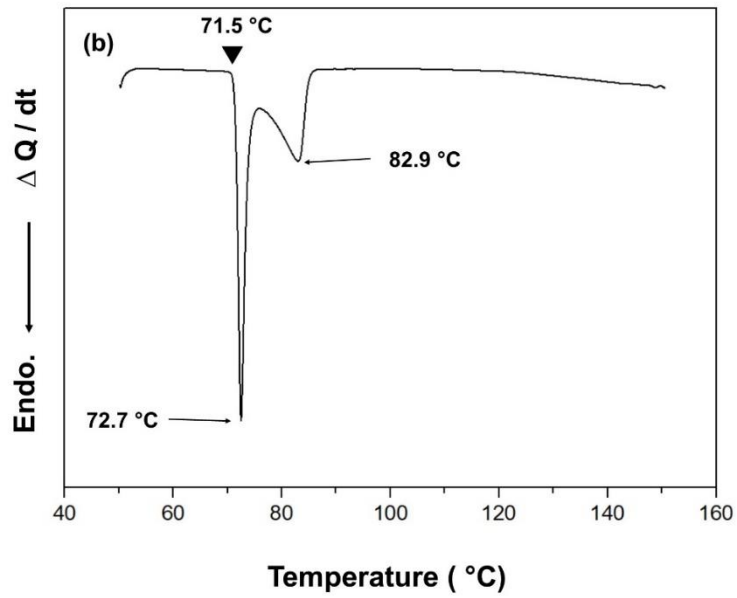
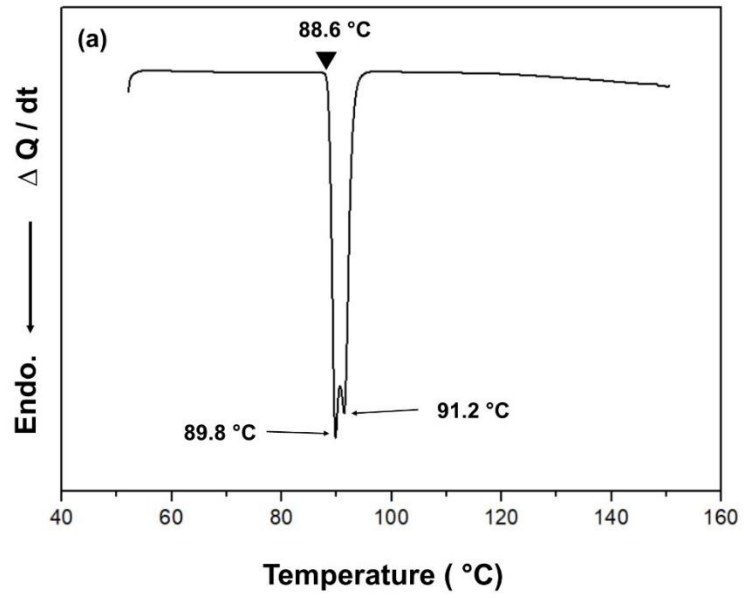


Figure 2.5 DSC curves for various solder compositions: (a) In-50Bi, (b) In-40Bi, (c) In-33.7Bi, (d) In-30Bi.

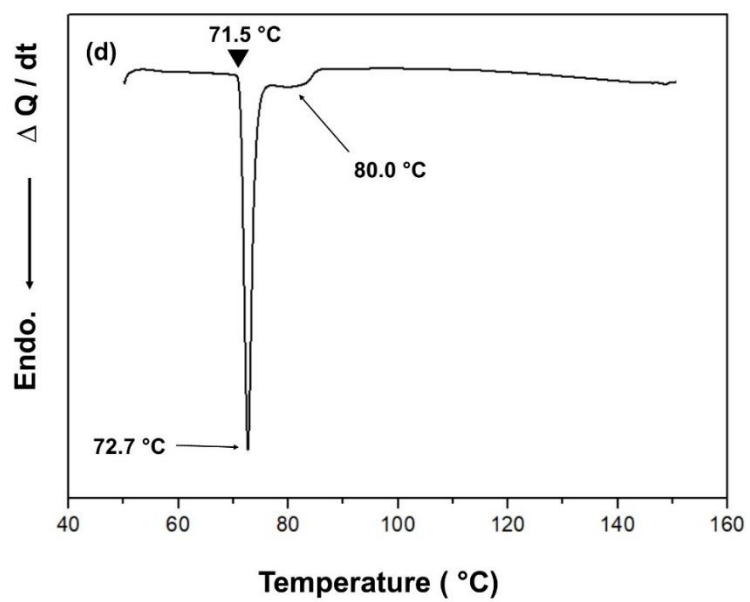
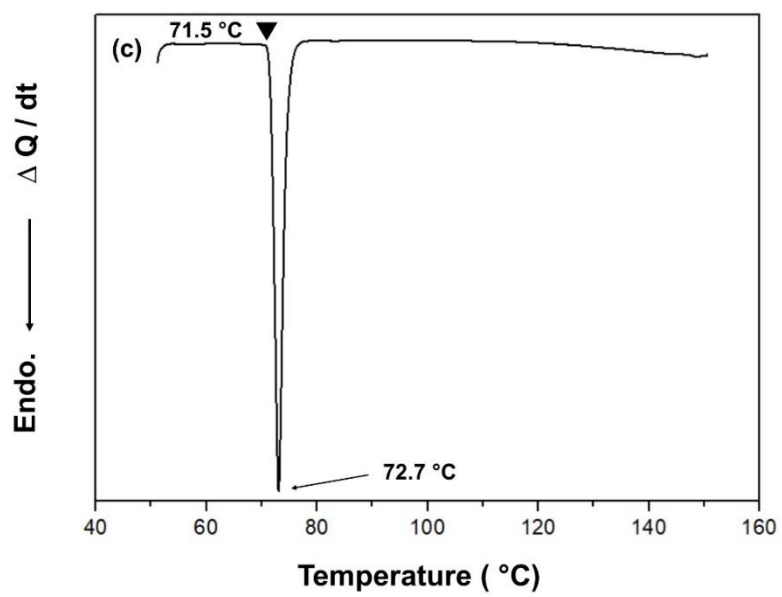


Figure 2.5 (continued)

Table 2.2 Results of DSC experiments with In-Bi alloys

Alloy compositions	Onset temperature (°C)	Peak I (°C)	Peak II (°C)	ΔH_m (mJ/mg)
In-50Bi	88.6	89.8	91.2	34.3
In-40Bi	71.5	72.7	82.9	29.1
In-33.7Bi (eutectic)	71.5	72.7		24.9
In-30Bi	71.5	72.7	80.0	27.9

similar to the eutectic line of 72.7 °C as can be seen from the In–Bi binary phase diagram. In the In–50Bi case, the onset temperature was found at 88.6 °C and the first endothermic peak existed at 89.8 °C which might be a peritectic reaction and a second endothermic peak existed at 91.2 °C which might be a congruent reaction. In the In–40Bi case, a first endothermic peak existed at 72.7 °C and a second endothermic peak existed at 82.9 °C which might be a hypoeutectic reaction. In the In–33.7Bi case, an endothermic peak existed at 72.7 °C. The plot shown in Fig. 2.5(c) appears to show only a single peak, which might be a eutectic reaction [7]. In the In–30Bi case, a first endothermic peak existed at 72.7 °C and a minor endothermic peak existed at 80 °C, which might be hypereutectic reaction. Minor endothermic peaks provide the evidence that In–30Bi is not a eutectic but an alloy with a composition very close to the eutectic composition. The melting transition of In–Bi alloys took place over a temperature of 1.2 °C. This phenomenon can be attributed to the phase transition due to the abrupt melting.

The enthalpy of fusion can be determined by computing the peak area of the DSC curve as listed in Table 2.2. The value of the enthalpy of fusion of the In–Bi alloys determined from the heating curves at a heating rate of 10 °C/min is between 24.9 J/g and 34.3 J/g. The variation of the fusion enthalpy measurement can be caused by various compositions. The eutectic composition had the smallest heat of fusion than the other compositions, which means that the eutectic composition produces phase transformation the easiest.

2.3.3 Mechanical properties

The mechanical properties of the In–Bi alloys were investigated using tensile test. The values measured were normalized to the starting parameters of the cross-section and gauge length to be illustrated (engineering stress-strain diagrams). Fig. 2.6 shows the stress-strain curves of a specimen measured at room temperature, whose figure shows well the averages and representative results determined for at least ten times. The stress-strain curves exemplify that of an In alloy in Table 2.3 and Fig. 2.7, respectively. The ultimate tensile strength (UTS) and elongation of the In–50Bi alloy were 17.8 MPa and 42.5 %; for the In–40Bi alloy, the respective values were 13.6 MPa and 43.2 %; for the In–33.7Bi alloy, the respective values were 11.1 MPa and 71.8 %, and for the In–30Bi alloy, the respective values were 10.2 MPa and 76.0 %. The UTS of the binary In–Bi alloys decreased, but their elongation dramatically increased when the indium content was increased at room temperature. The decrease in UTS through the indium addition was most likely caused by the deformation induced from recrystallization [8]. A large increase in ductility might be caused by the addition of excess indium to the binary In–Bi alloys that formed the In-rich phase [9]. The elastic-plastic transition was clearly resolved by a sharp bend in the stress-strain curve. The ideal plastic behavior is a good approximation for deformation of indium-based solders at room temperature. The decrease in measured load is due to the increasing reduction in cross-sectional area up to the neck of the sample.

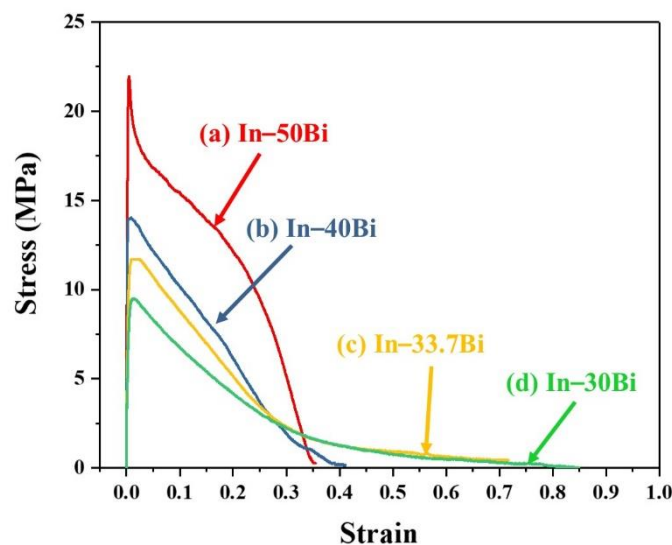


Figure 2.6 Tensile test results by alloy compositions: (a) In–50Bi, (b) In–40Bi, (c) In–33.7Bi, (d) In–30Bi.

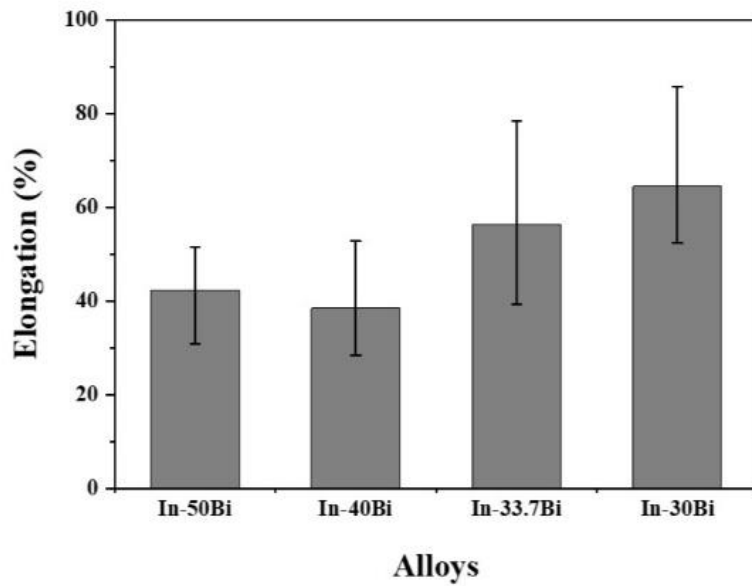
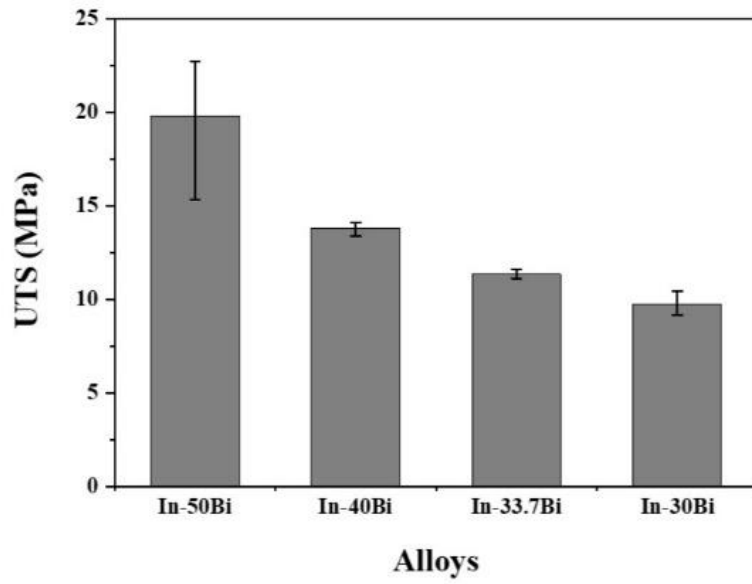


Figure 2.7 Corresponding results of the tensile tests.

Table 2.3 Comparison of tensile test result of low-temperature alloys

Compositions		UTS (MPa)	Elongation (%)	Strain rate	Temperature (°C)	References
In-xBi alloys	In-50Bi	17.8	42.5	0.0005/s	25	-
	In-40Bi	13.6	43.2			
	In-33.7Bi (eutectic)	11.1	71.8			
	In-30Bi	10.2	76.0			
Sn-58Bi (eutectic)		48.2	37.5	0.0005/s	25	[10]
Sn-52In (eutectic)		12.0	47.3	0.001/s	25	[11]

Both the elongation and reduction in the area remained very high. Table 2.3 shows comparison of the tensile results of alternative low-temperature alloys. The UTS result of In-Bi alloys is lower than Sn-58Bi [10], however, similar to Sn-52In [11]. And in case of elongation, In-Bi alloys have excellent ductility than Sn-58Bi and Sn-52In. In conclusion, the In-Bi alloys have outstanding low-temperature deformation properties as expected.

2.3.4 Fracture Characteristics

The fracture specimens after tensile test were observed with different alloy compositions as shown in Fig. 2.8. The In-Bi alloy has outstanding low-temperature deformation properties. As expected, In-Bi alloys revealed high ductility. Fig. 2.8 depicts the macroscopic fracture modes for each alloy. The fracture surfaces in Figs. 2.9 show ductile fractures of the neck shape for all the In-Bi alloys at room temperature, which is common shape for soft alloys. Different neck shapes occurred because of the ductile properties of indium. Typically, ductile fractures have some evidences of appreciable gross deformation at the fracture surfaces such as twisting and tearing [12]. The center of the dumbbell-shaped bar, is expected to show evidence of necking, with a significant portion of the fracture surface. The In-50Bi that has the lowest indium content gives moderately ductile fracture characteristics

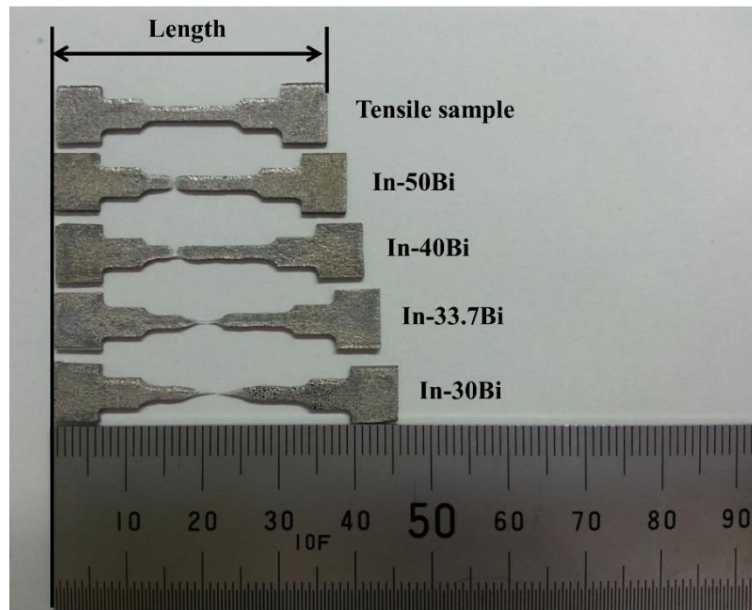


Figure 2.8 Photographs of the bulk specimens after tensile tests for observing change in length.

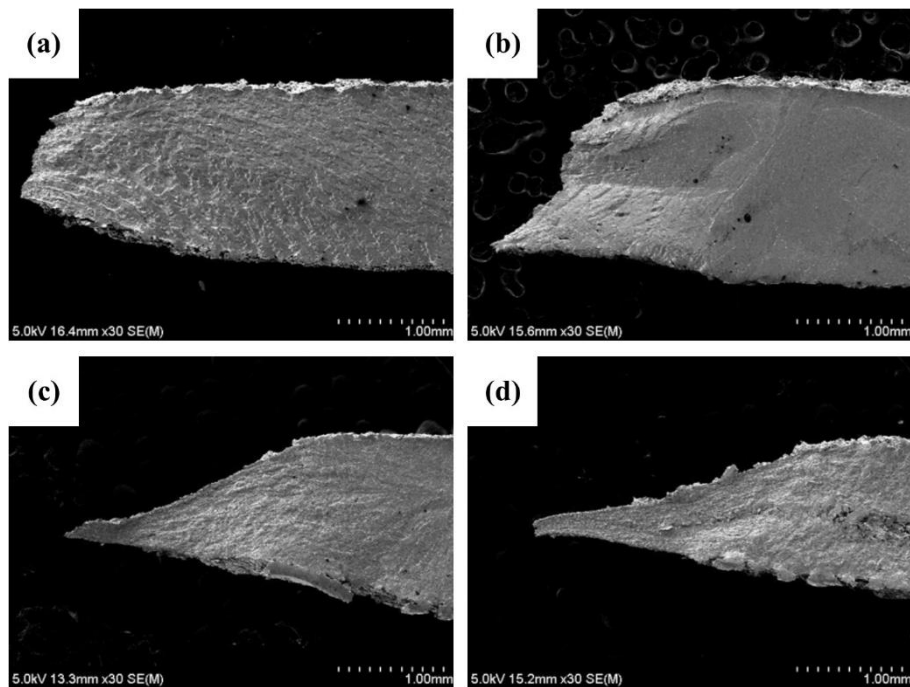


Figure 2.9 Fracture surfaces on side view after tensile tests: (a) In-50Bi, (b) In-40Bi, (c) In-33.7Bi, (d) In-30Bi.

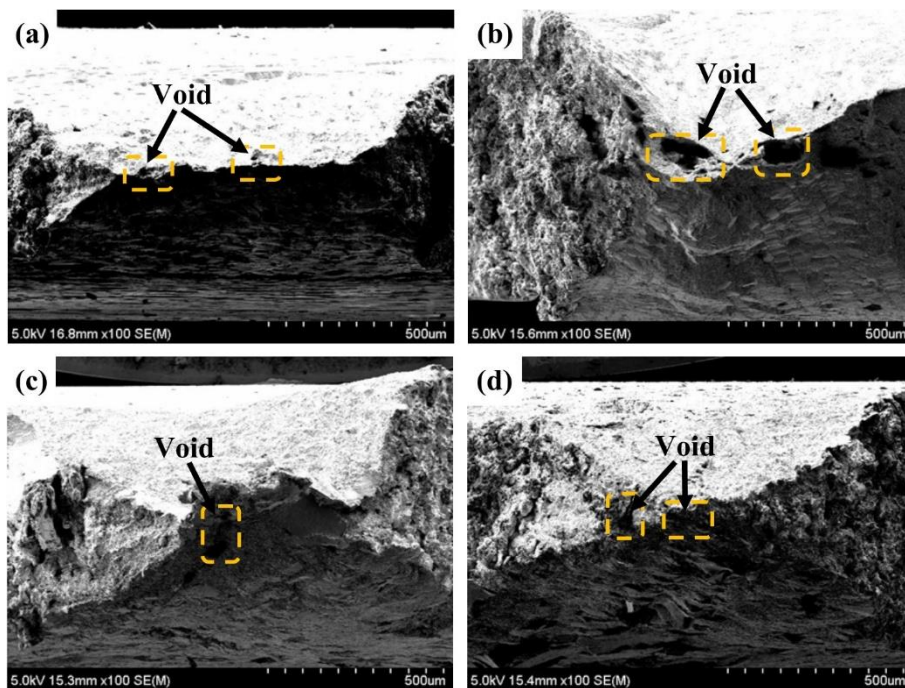


Figure 2.10 Fracture surfaces on top view after tensile tests: (a) In-50Bi, (b) In-40Bi, (c) In-33.7Bi, (d) In-30Bi.

after some necking, as shown in Fig. 2.9(a). In this central interior region, an irregular and fibrous appearance occurred. However, higher indium contents are shown to be of high ductility, as represented by close to approximately 100 % reduction in cross-sectional area shown in Figs. 2.9(c-d). It necks down to a point and this type of failure is typically called a rupture. Ductility fracture is accompanied by necking, microvoids nucleation and coalescence, or grain boundary sliding [13, 14]. During the ductile fracture process, the fracture is caused by simple overloads, or by applying too high a stress to the In-Bi alloys. Fig. 2.10 shows some voids could be observed around the tip of fracture position. Generally, small spherical voids form when a high stress causes separation of the alloy at grain boundaries. As the local stress increases, the microvoids grow and coalesce into larger cavities. Eventually, the contact area becomes too small to support the load and fracture occurs. From the view point of the fracture shape, typical ductile fracture made could be observed for all alloys.

2.4 Conclusion

In this chapter, the effects of In content on the microstructure and mechanical properties of In–Bi alloys were investigated. The following conclusions can be made:

- (1) The microstructures of the investigated In–Bi alloys contained primary In-phase, Bi_3In_5 , and BiIn_2 Phases.
- (2) Indium depresses the melting temperature of In–Bi alloys when the indium content is increased. The endothermic peaks were found in the DSC curves: the solid-liquid phase transformation occurred between $72.7\text{ }^\circ\text{C}$ and $91.2\text{ }^\circ\text{C}$ on each DSC curve.
- (3) The tensile strength of the In–Bi alloys declined with increasing indium content. On the other hand, elongation was dramatically increased when the indium content was increased at room temperature.
- (4) A typical appearance of ductile fracture was found in the In–Bi alloys. As the indium content increased, the cross-sectional area of the tensile sample decreased, which shows high-ductility characteristics.

In the view point of melting properties and mechanical properties, the In–33.7Bi alloy with $72.7\text{ }^\circ\text{C}$ eutectic melting temperature is a candidate for potential applications of flexible electronic devices using PP and PMMA as substrate.

References

- [1] JIS Z 3198-1, The methods for lead-free solders-part 1: Methods for measuring of melting temperature ranges, Jpn. Ind. Stand., (2003) 1–6
- [2] Shi, X. Q., et al., “Effect of temperature and strain rate on mechanical properties of 63Sn/37Pb solder alloy”, TRANSACTIONS-AMERICAN SOCIETY OF MECHANICAL ENGINEERS JOURNAL OF ELECTRONIC PACKAGING, 121 (1999) 179–185
- [3] Zhao, J., Y. Miyashita, and Y. Mutoh, “Fatigue crack growth behavior of 96.5 Sn–3.5 Ag lead-free solder”, International Journal of fatigue, 23.8 (2001) 723–731
- [4] H. Okamoto, P.R. Subramanian, L. Kacprzak, “Binary Alloy Phase Diagrams”, 2nd edn. ASM International, Materials Park, (1990) 748–750
- [5] Mokhtari, Omid, and Hiroshi Nishikawa, “Correlation between microstructure and mechanical properties of Sn–Bi–X solders”, Materials Science and Engineering: A, 651 (2016) 831–839
- [6] N.-C. Lee, “Optimizing the reflow profile via defect mechanism analysis” Solder. Surf. Mt. Technol., 11(1) (1999) 13–20
- [7] T. Hakakeyama, Z. Liu, “Handbook of Thermal Analysis”. Wiley, New York (1998) 6–13
- [8] R.P. Reed et al., “Tensile strength and ductility of indium”, Mater. Sci. Eng. A, 102(2) (1988) 227–236
- [9] M. Plotner, B. Donat, A. Benke, “Deformation properties of indium-based solders at 294 and 77 K”, Cryogenics, 31(3) (1991) 159–162
- [10] Chen, Xu, et al., “Mechanical deformation behavior and mechanism of Sn–58Bi solder alloys under different temperatures and strain rates”, Materials Science and Engineering: A, 662 (2016) 251–257
- [11] Jones, W. K., Y. Q. Liu, and M. Shah, “Mechanical properties of Sn–In and Pb–In solders at low temperature” Proceedings 3rd International Symposium on Advanced Packaging Materials Processes, Properties and Interfaces. IEEE (1997) 46–53

- [12] Cheng, Xiaojin, “A study on indium joints for low-temperature microelectronics interconnections”, Diss. Loughborough University (2011) 23–24
- [13] A.A. Benzerga, L. Jean-Baptiste, “Ductile fracture by void growth to coalescence.”, *Adv. Appl. Mech.*, 44 (2010) 169–305
- [14] A. Pineau, A.A. Benzerga, T. Pardoen, “Failure of metals I: Brittle and ductile fracture”, *Acta Mater.*, 107 (2016) 424–483

Chapter 3

Melting properties and microstructure of In–Bi alloys during isothermal aging

3.1 Introduction

Previous study (*Chap. 2*) have investigated the basic properties of In–Bi alloys, as well as their melting and mechanical properties. However, the reliability of solder alloy in the user environment is important for flexible electronics. Therefore, in this study, the thermal aging test was conducted on In–Bi alloy specimens to evaluate the change of their morphologies, phase constitution and thermal property during aging. As refer to the JEDEC Standard (JESD22-A103C) [1], Thermal aging test conditions and durations may be used as appropriate by metals characteristics such as melting point of metals. In particular, the reason why the aging temperature is set at 40 °C and 60 °C, the normal aging temperature is about 80 % of the melting temperature of the material in degree Kelvin (273 plus the degrees centigrade) [2]. However, a thermal aging temperature based on In–33.7Bi (eutectic) alloy was calculated by 2.6 °C as shown in Table 3.1. The temperature of 2.6 °C is below room temperature. It means the thermal aging test can only be confirmed the thermal effect of room temperature. Therefore, an aging

Table 3.1 The temperature of thermal aging test by calculated

Alloy system designations	Onset temperature	80 % of	90 % of	93.8 % of	95 % of
In–50Bi	71.5 °C	2.6 °C	37.1 °C	50.1 °C	54.3 °C
In–40Bi	88.6 °C	16.3 °C	52.4 °C	66.2 °C	70.5 °C
In–33.7Bi					
In–30Bi					

Table 3.2 Using condition of electronic devices

	Automotive electronics	Home appliance	Industrial
Using condition of temperature	- 40 ~ 155 °C	0 ~ 40 °C	- 10 ~ 70 °C
Using condition of humid	0 ~ 100 %	Low	Low

temperature of 40 and 60 °C was selected as it represents the typical user and harsh environmental conditions for flexible electronic devices as shown in Table 3.2 [3-5].

3.2 Experimental

3.2.1 Alloy preparation and aging process

The In and Bi used in this study were in the form of a pure metal sheet and shot, respectively, both which are commercially available. As shown in Table 3.1, In–Bi binary alloys were fabricated with as the same with Chapter 2. Alloys with 50, 60, 66.3, and 70 mass% In (Nilaco., Tokyo, Japan, 99.99% pure) are herein referred to as In–50Bi, In–40Bi, In–33.7Bi (eutectic), and In–30Bi, respectively. These specimens were fabricated by dissolving the corresponding metallic sheet and shot in a furnace at 500 °C for 5 h. An equipoise with ± 0.1 mg accuracy was used to weigh the elements. The alloying process was performed in a graphite crucible, in air, with manual stirring every 30 min to ensure homogeneity. The molten alloy was then chill-cast in a steel mold to form a bar-type ingot with a length of 50 mm, width of

10 mm, and thickness of 5 mm. Before the thermal aging test the In–Bi alloys were remelted at 250 °C for 1 h in a crucible. Next, they were cast into bar-shaped steel molds and machined into dumbbell shapes for tensile testing using wire-cutting electrical discharge machines (AG360L, Sodick, Kanagawa, Japan). As shown in Figure 3.1, the dimensions of the gauge section of the tensile test specimens were 1.0 mm (depth) × 2.0 mm (width) × 10 mm (length). The dumbbell shape allows the fracture in the middle of the samples to be observed. After machining, SiC paper was utilized to polish the specimens mechanically, up to #2000 grit. Next, polycrystalline diamond spray (3 and 1 μm; DP-spray P, Struers, Ballerup, Denmark) was used to further polish

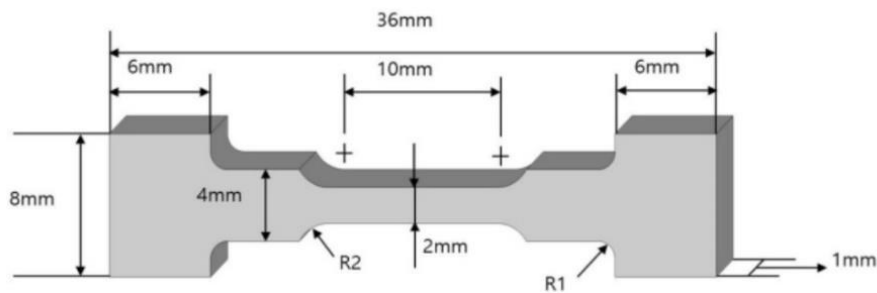


Figure 3.1 The geometry and size of the tensile test specimen.

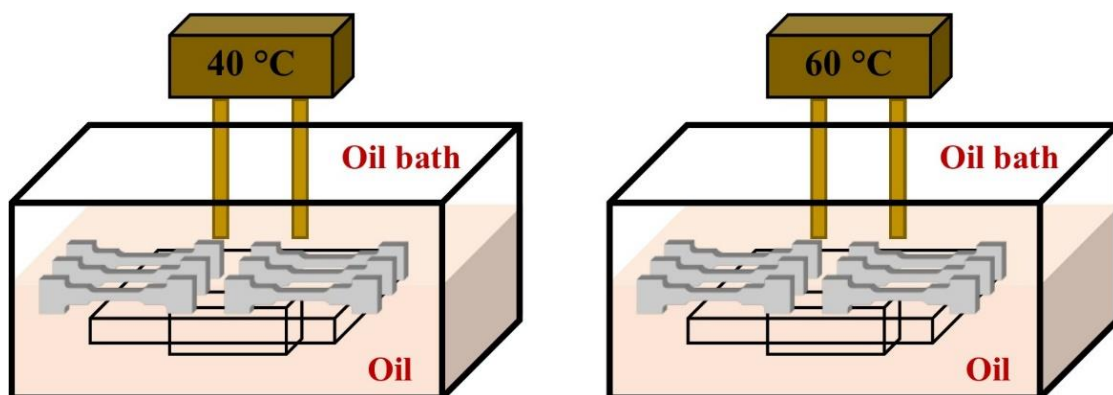


Figure 3.2 The geometry of thermal aging test in oil bath.

Table 3.3 Sample size of thermal aging test

Temperature	Alloy system designations	108 h	504 h	1008 h	Sum.	Total
40 °C	In-50Bi	8	8	8	24	96
	In-40Bi	8	8	8	24	
	In-33.7Bi	8	8	8	24	
	In-30Bi	8	8	8	24	
60 °C	In-50Bi	8	8	8	24	96
	In-40Bi	8	8	8	24	
	In-33.7Bi	8	8	8	24	
	In-30Bi	8	8	8	24	

the specimens. The polished specimens were used for tensile testing after thermal aging. Eight repetitions of the tests were performed to collect the presented results and averages as shown in Table 3.3. The samples were aged in an oil bath at a temperature of 40 °C and 60 °C for 168, 504, and 1008 h as shown in Fig 3.2. After aging, the samples were removed from the oil bath and cooled to 23 °C. The oil on the sample surfaces was removed with ethanol.

3.2.2 Melting temperature, elemental analysis and microstructure

The melting temperatures of the In-Bi alloys were measured by differential scanning calorimetry (DSC, DSC7020, Hitachi, Tokyo, Japan). All samples for DSC were approximately 0.008 g and used an aluminum pan and cover assembly. The scan temperature ranges from 30 to 120 °C was controlled at a rate of approximately 10 °C / min. The melting behaviors of the In-Bi alloys were determined using a typical onset-intercept method by JIS Z 3198-1 [6]. During all DSC runs, the samples were kept in an inert environment to prevent oxidation by flowing a constant flow of nitrogen gas. The heating was repeated three times.

The phase contents of each alloy were measured by X-ray diffraction (XRD, Ultima IV, Rigaku, Tokyo, Japan) with Cu K α radiation ($\lambda = 1.54059 \text{ \AA}$) at an accelerating voltage of 40 kV. The

diffraction beam was scanned in steps of 0.02° across the 2θ range of $20\text{--}80^\circ$ at $2^\circ/\text{min}$. The International Center for Diffraction Data powder diffraction file cards, including #00-005-0642 for In, #01-071-0226 for BiIn_2 , and #01-071-0223 for Bi_3In_5 , were used as references to identify the diffraction patterns [7]. Quantitative phase analysis was conducted via the reference intensity ratio method using PDXL software provided by Rigaku. Phase analysis was reaffirmed by HighScore Plus software version 3.0e (PANalytical B.V, Almero, Netherlands). A fine cutter was employed to section the samples and the bulk samples were mounted in epoxy and hardener. Next, SiC paper was employed to polish the mounted samples up to 2000 grit. DP-spray P (3 and $1\ \mu\text{m}$) was also used to polish the samples before the final step, which involved an oxide polishing suspension (OP-S, Struers). Immediately following the polishing process the samples were submerged in pure ethanol and ultrasonically cleaned for 5 min. A morphological study of the microstructure was performed using a field-emission scanning electron microscope (FE-SEM, SU-70, Hitachi, Tokyo, Japan) equipped with energy-dispersive spectroscopy (EDS, Oxford Instruments, Abingdon, UK). Elemental mapping of the microstructure was performed using an electron probe microanalyzer (EPMA, JXA-8530F, JEOL, Tokyo, Japan). The eutectic spacing of the In–33.7Bi alloy, as defined in Figure 3.3, was measured to quantify the magnitude of the fine structure under thermal aging using ImageJ software, which measured 30 positions under each aging condition.

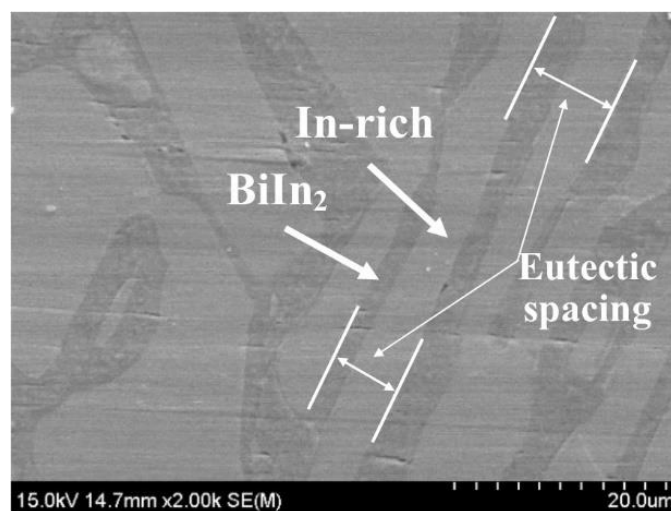


Figure 3.3 Eutectic spacing within the eutectic In–33.7Bi alloy bulk after 1008 h of thermal aging.

3.3 Results and discussions

3.3.1 Melting temperature, phase constitution and microstructure

In previous *Chapter 2*[8], we have analyzed the melting properties of In–xBi alloy. And in this study, DSC performed on the samples before and after aging, and the DSC curves for all specimens are showed in Fig. 3.4 and summarized in Table 3.4. The onset temperature means a melting start of material [9]. As shown in Fig. 3.4(a), during the heating process of the DSC analysis, the In–50Bi alloy showed the onset temperature at 88.6 °C and a first endothermic peak existed at 89.8 °C which might be a peritectic reaction and a second endothermic peak existed at 91.2 °C which might be a congruent reaction [8]. As shown in Fig. 3.4(b), the In–40Bi alloy showed the onset temperature at 71.5 °C and a first endothermic peak existed at 72.7 °C and a second endothermic peak existed at 82.9 °C which might be a hypoeutectic reaction. As shown in Fig. 3.4(c), the In–33.7Bi alloy showed the onset temperature at 71.5 °C and an endothermic peak existed at 72.7 °C which might be eutectic reaction.

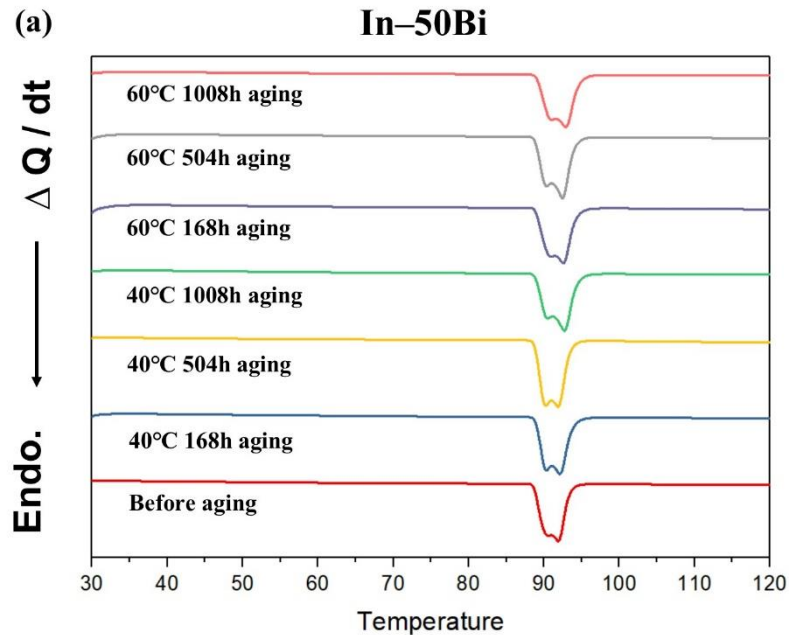


Figure 3.4 DSC curves under thermal aging test at 40 and 60 °C after 168 h, 504 h and 1008 h: (a) In–50Bi, (b) In–40Bi, (c) In–33.7Bi and (d) In–30Bi.

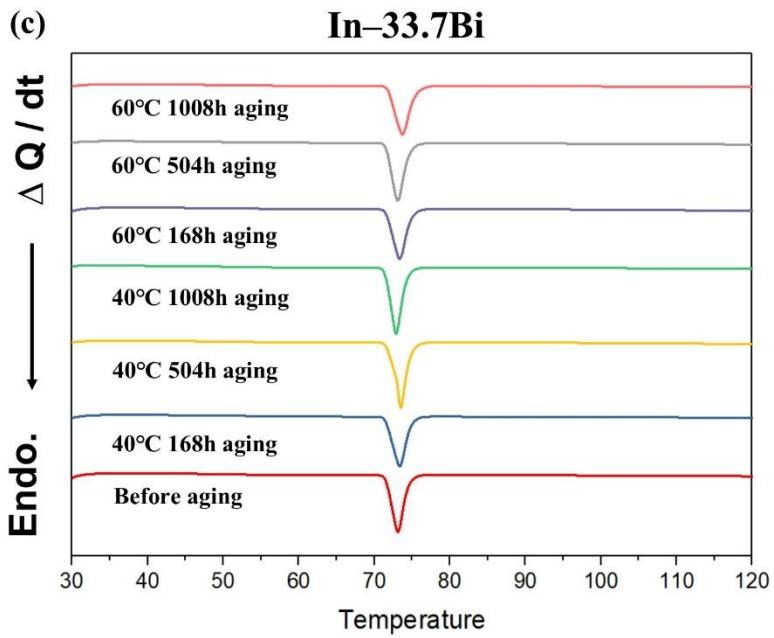
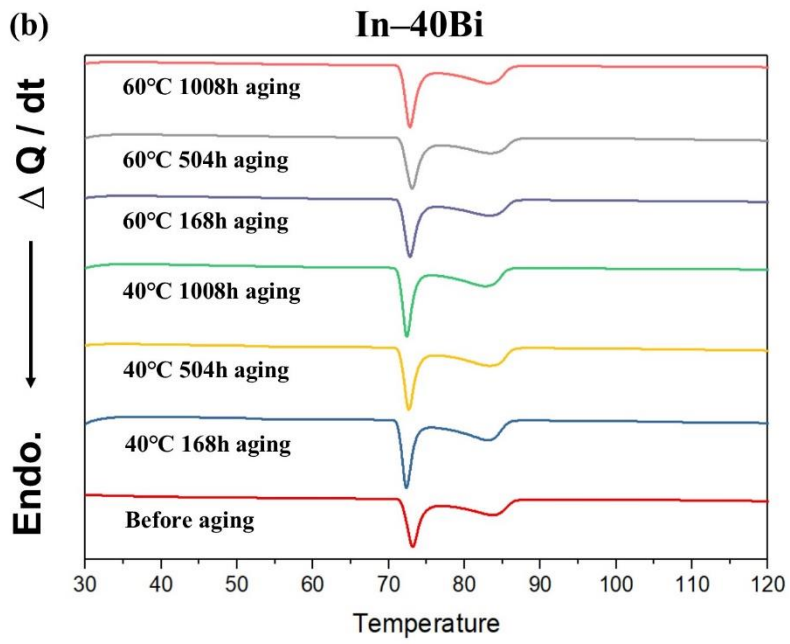


Figure 3.4 (continued)

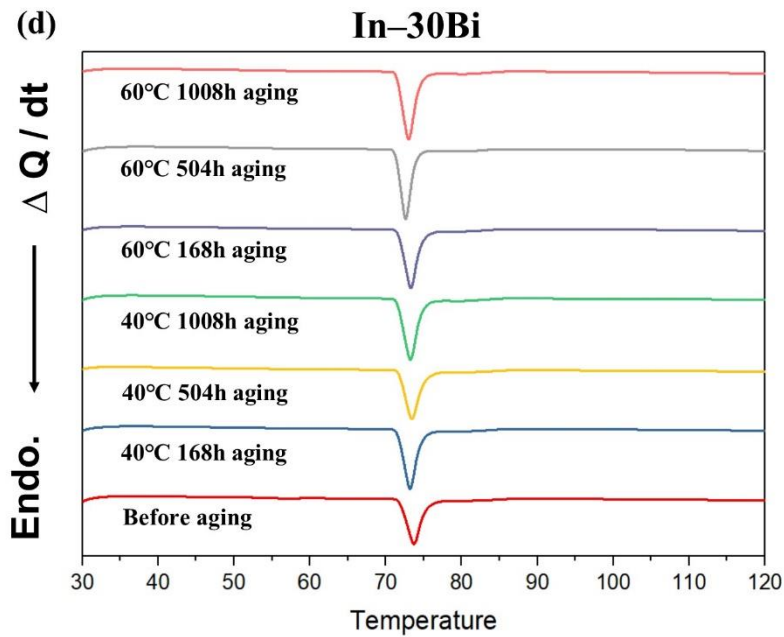


Figure 3.4 (continued)

Table 3.4 Results of DSC experiments with In-Bi alloys under thermal aging at 40 °C after 1008 h

Alloy compositions	Onset temperature (°C)	Peak I (°C)	Peak II (°C)	ΔH_m (mJ/mg)
In-50Bi	88.6	89.8	91.2	34.3
In-40Bi	71.5	72.7	82.9	29.1
In-33.7Bi (eutectic)	71.5	72.7		24.9
In-30Bi	71.5	72.7	80.0	27.9

Finally, as shown in Fig. 3.4(d), In-30Bi alloy showed the onset temperature at 71.5 °C and an endothermic peak existed at 72.7 °C and a minor endothermic peak existed at 80 °C which might be hypereutectic reaction. Minor endothermic peaks provide the evidence that In-30Bi is not a eutectic same as In-33.7Bi. However, it means very close to the eutectic composition. As shown in Fig. 3.4, the results of DSC did not change significantly even after thermal aging

at 40 and 60 °C. It means that there is no new phase generated by the reaction. In other to confirm the phase constitution of In-Bi alloys.

We compared the phase compositions of the as-cast and thermally aged alloys. The XRD patterns of the In–Bi alloys shown in Figure 3.5 include BiIn_2 , Bi_3In_5 , and In-phase peaks. According to the In–Bi binary phase diagram [10], two IMC phases of BiIn_2 and Bi_3In_5 formed in the In–50Bi alloy. Fig. 3.5 show the Bi_3In_5 phase which was generated from a peritectic reaction occurring at 88.9 °C. A peritectic reaction occurring between 93.5 and 49 °C also generated the ϵ -phase, which formed a eutectic with BiIn_2 at 72.7 °C. Figure 3.5 shows the comparison of XRD patterns for In–Bi alloys under thermal aging test at 40 and 60 °C after 168 h, 504 h and 1008 h. No significant differences appear between the patterns for the as-cast and thermally aged specimens.

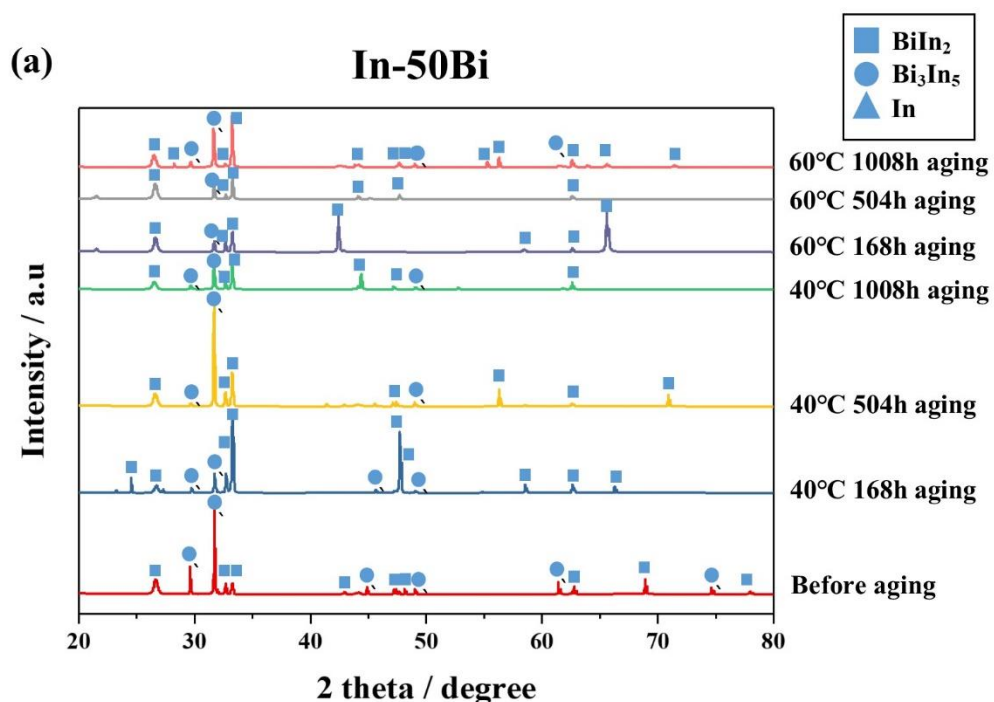


Figure 3.5 Comparison of XRD (X-ray Diffraction) patterns for In–Bi alloys under thermal aging test at 40 and 60 °C after 168 h, 504 h and 1008 h: (a) In–50Bi, (b) In–40Bi, (c) In–33.7Bi and (d) In–30Bi.

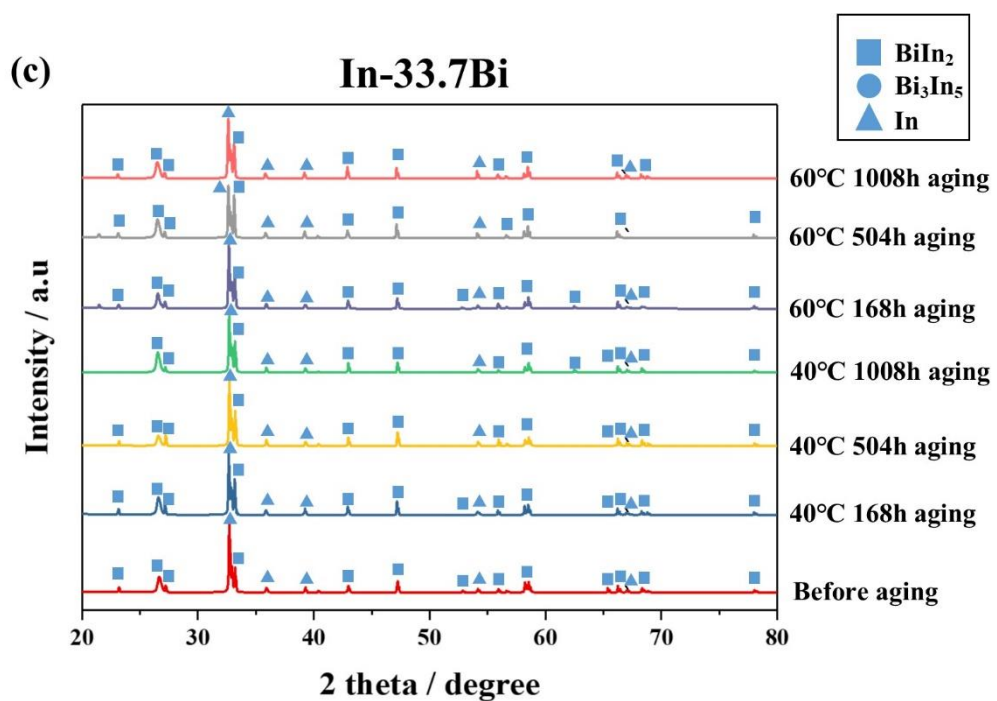
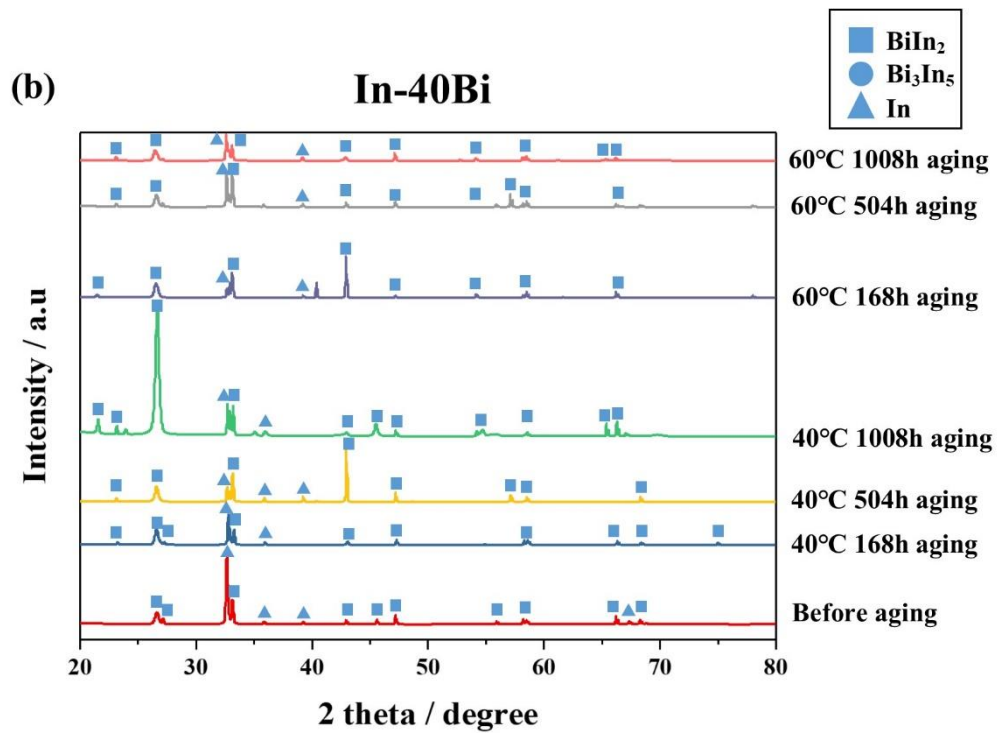


Figure 3.5 (continued)

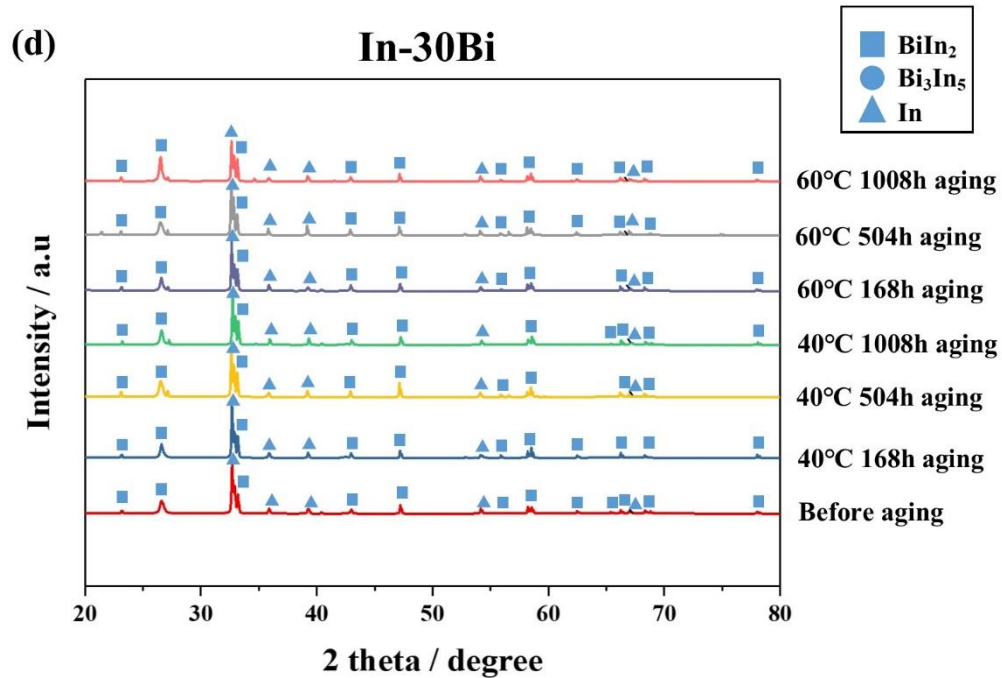


Figure 3.5 (continued)

Figure 3.6 shows cross-sectional images of the In–Bi alloys. The dark gray and bright gray colors represent the In-rich phase and Bi_xIn_y IMCs, respectively. A peritectic reaction occurs when Bi_3In_5 isolates the liquid and the solid-solution phase of BiIn [10]. A peritectic reaction also occurs when the In–50Bi alloy appears. The In–40Bi alloy is hypoeutectic; at the liquidus temperature the solidification of the liquid begins, leading to a solid BiIn_2 phase. However, the eutectic reaction must occur in order for the solidification to finish. Cooling the alloy below 72.7 °C allows the eutectic reaction to occur for all of the remaining liquid. A transformation into a lamellar mixture of In and BiIn_2 follows the cooling process; particularly for In–33.7Bi, in which eutectic microconstituents surround the solid BiIn_2 , as shown in Figure 3.6. No significant differences appear between the patterns for the as-cast and thermally aged specimens as shown in Fig. 3.7.

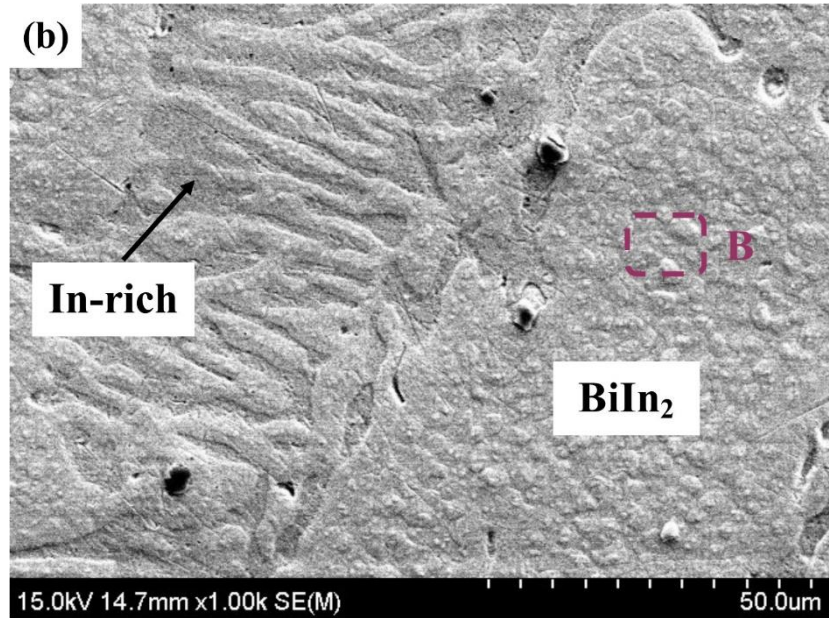
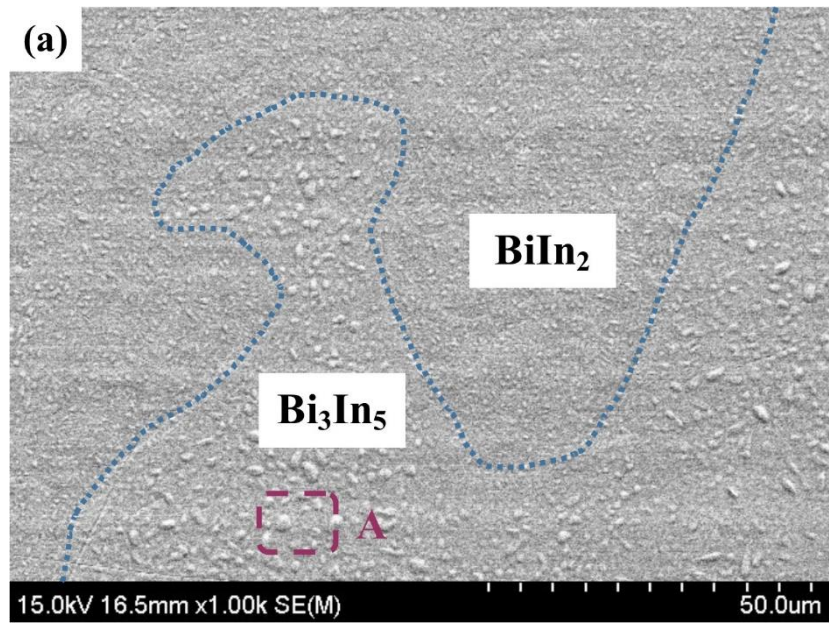


Figure 3.6 Cross-sectional SEM images of In–Bi alloys under thermal aging test at 60 °C after 504 h: **(a)** In–50Bi, **(b)** In–40Bi, **(c)** In–33.7Bi and **(d)** In–30Bi.

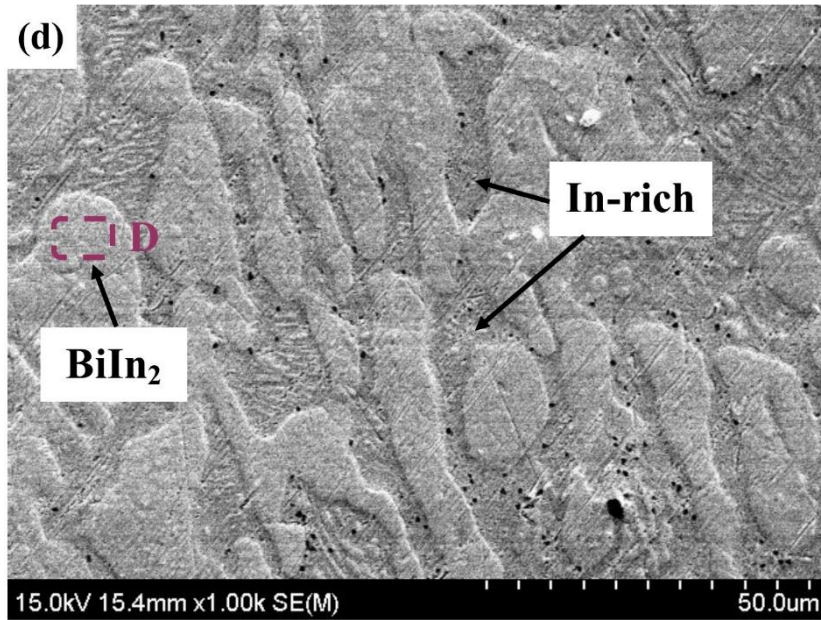
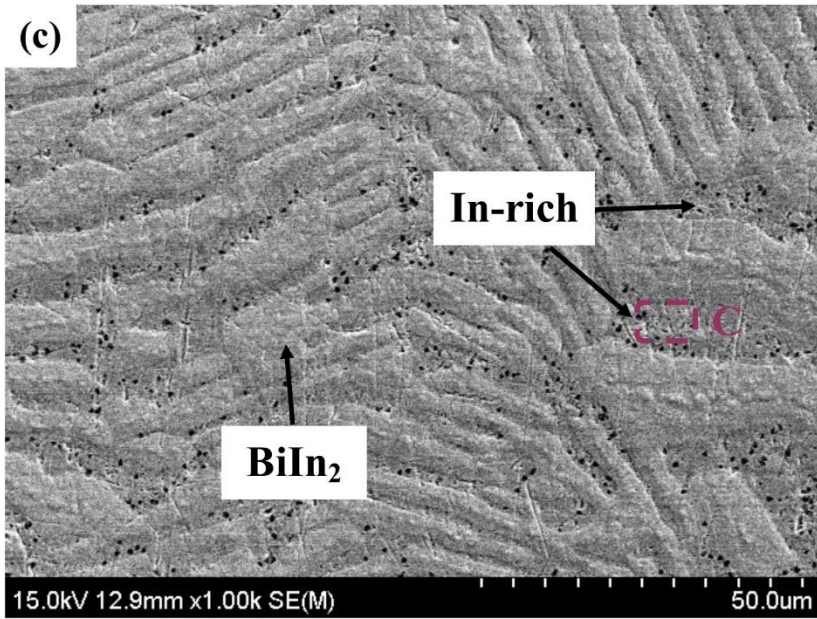


Figure 3.6 (continued)

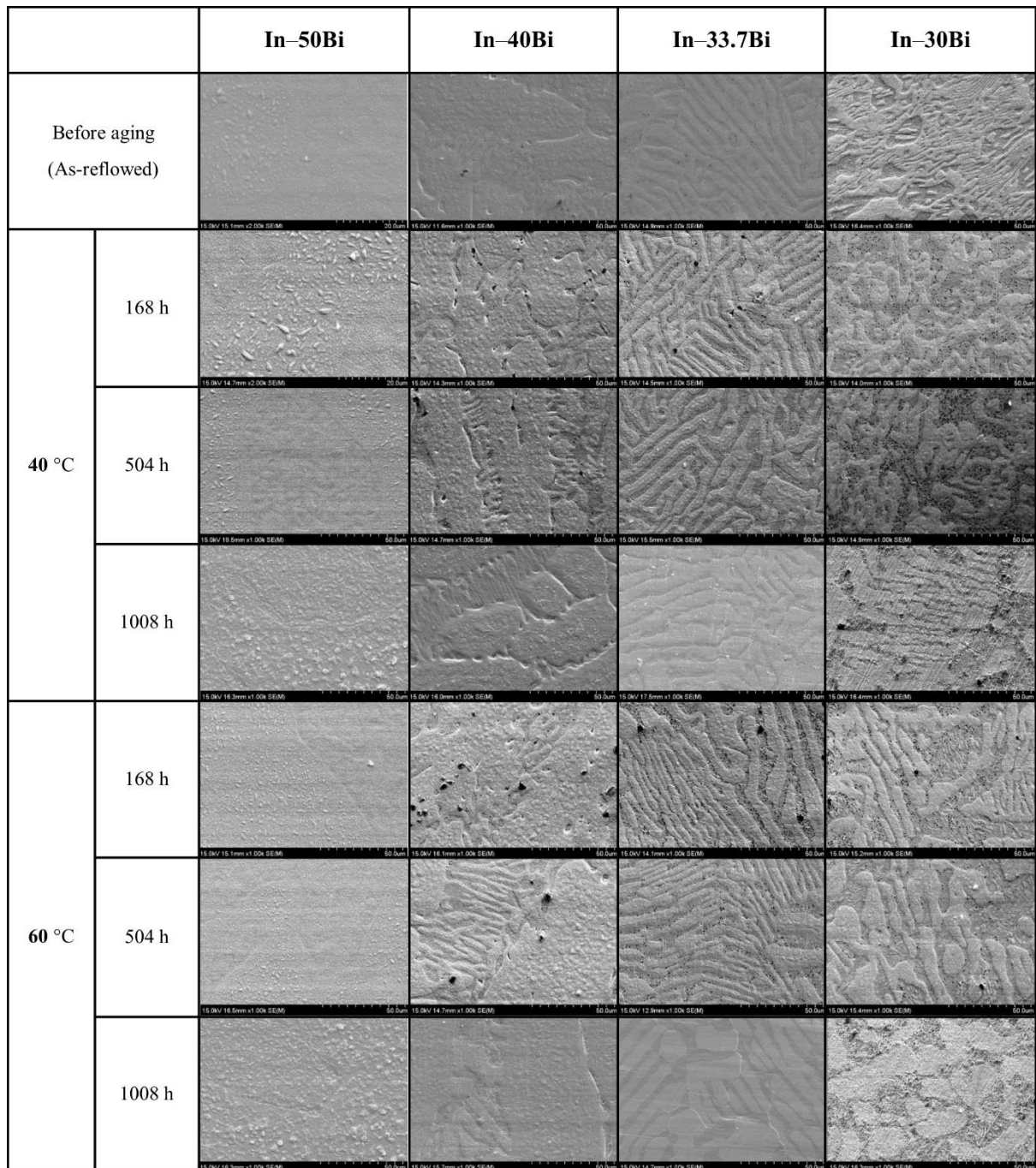


Figure 3.7 Cross-sectional SEM images of In-Bi alloys: (a) as-cast and (b) thermally aged for 1008 h at 40 °C.

Figure 3.8 shows the backscattered electron and mapping images obtained using the EPMA. These images show several signals from In and Bi. The Bi_3In_5 and BiIn_2 phases can be clearly identified in these images. For In–50Bi, the phases are completely separated into the Bi_3In_5 and BiIn_2 phases as shown in Fig. 3.8(a). In the elemental map obtained through the EPMA the bright gray region has a composition of Bi–62In (at. %) and can be classified as Bi_3In_5 ; the dark gray region is Bi–67In (at. %) and can be classified as BiIn_2 . However, in In–33.7Bi the bright region is BiIn_2 and the dark region is Bi–98In (at. %), and is therefore classified as an the In-rich phase, as shown in Fig. 3.8(c) and Table 3.4. No significant differences appear between the patterns for the as-cast and thermally aged specimens as shown in Fig. 3.8

As defined in Figure 3.3, the eutectic spacing of the In–33.7Bi alloy is measured. Figure 3.11 shows that the eutectic spacing of the as-cast In–33.7Bi alloy is 5.12 μm . Small changes in the eutectic spacing are observed in In–33.7Bi after thermal aging at 40 °C and 60 °C for 168, 504, and 1008 h. The eutectic spacing gradually increases during thermal aging because of the accelerated diffusion rate between the In and Bi phases and the trend to achieve chemical

(a) In–50Bi

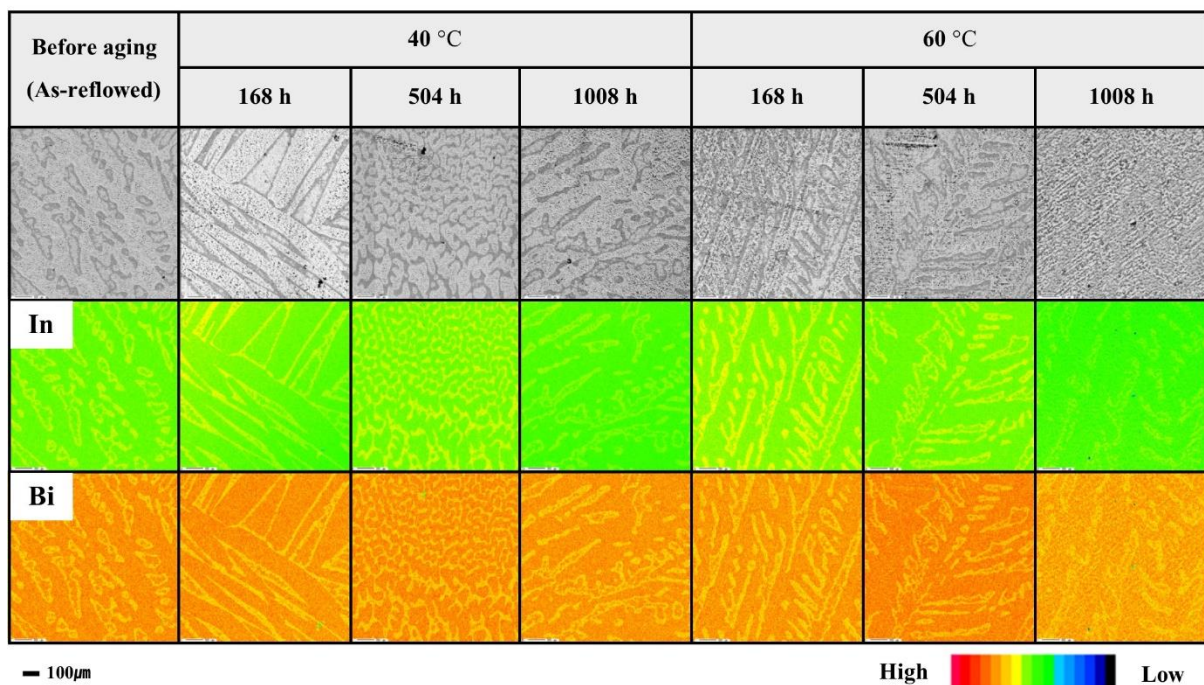
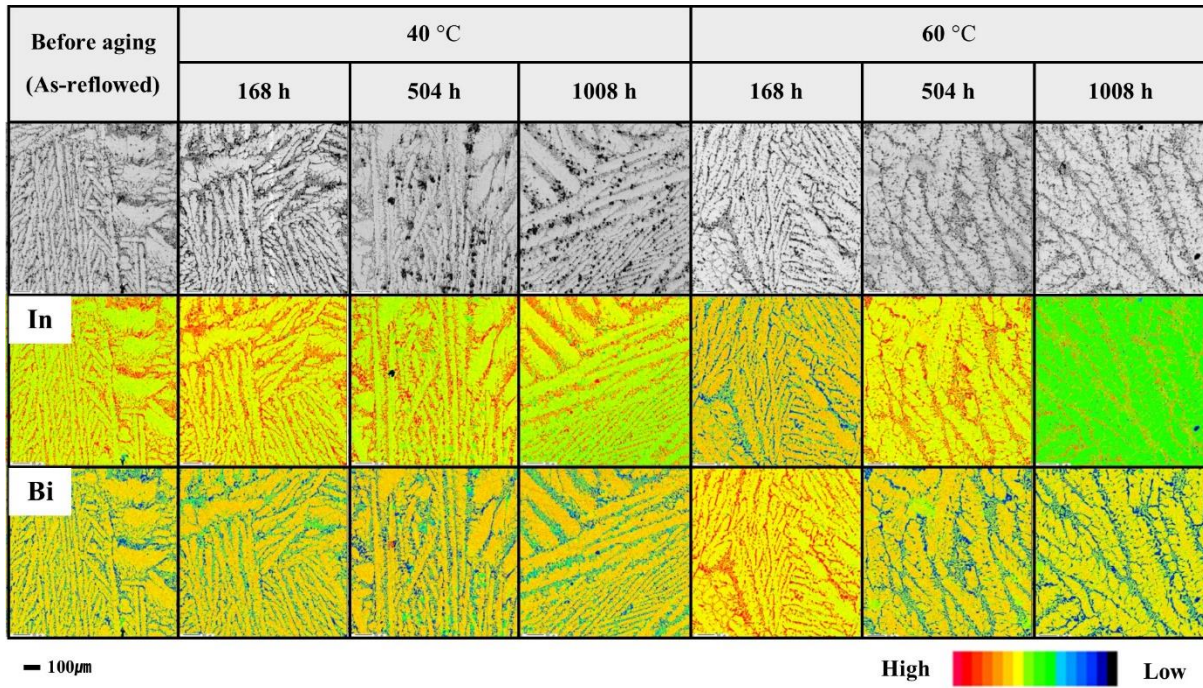


Figure 3.8 Electron probe microanalyzer (EPMA) elemental mapping results of the In–Bi alloys after thermally aged: (a) In–50Bi, (b) In–40Bi, (c) In–33.7Bi and (d) In–30Bi.

(b) In-40Bi



(c) In-33.7Bi

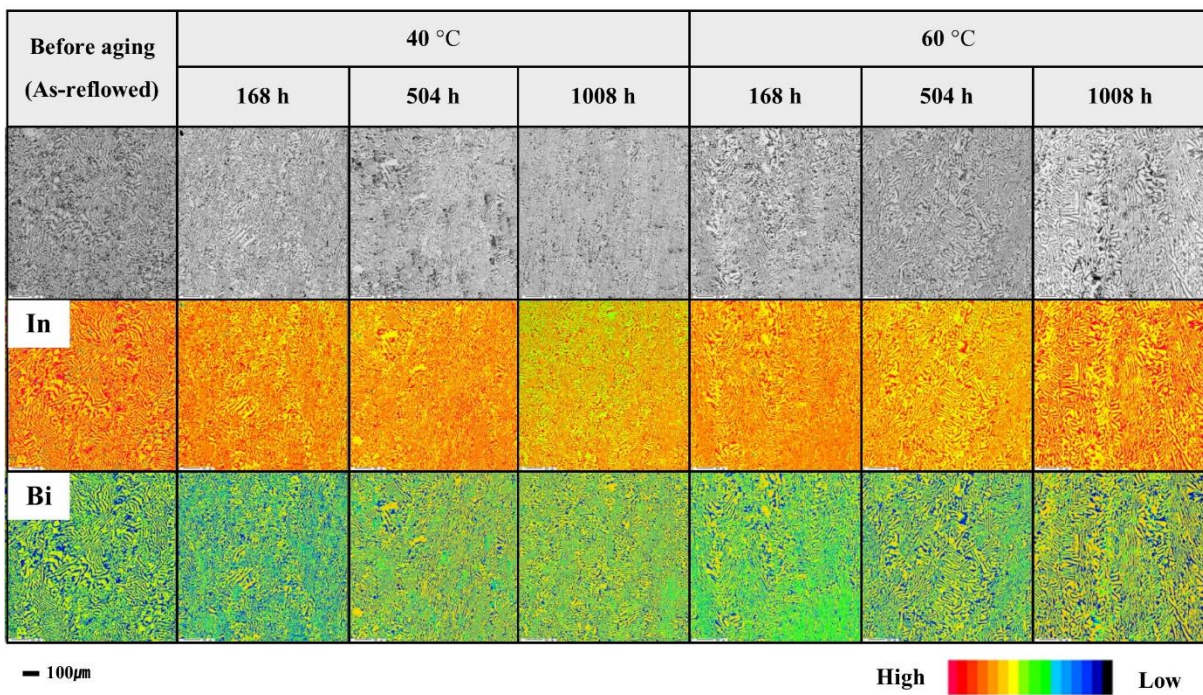


Figure 3.8 (continued)

(d) In-30Bi

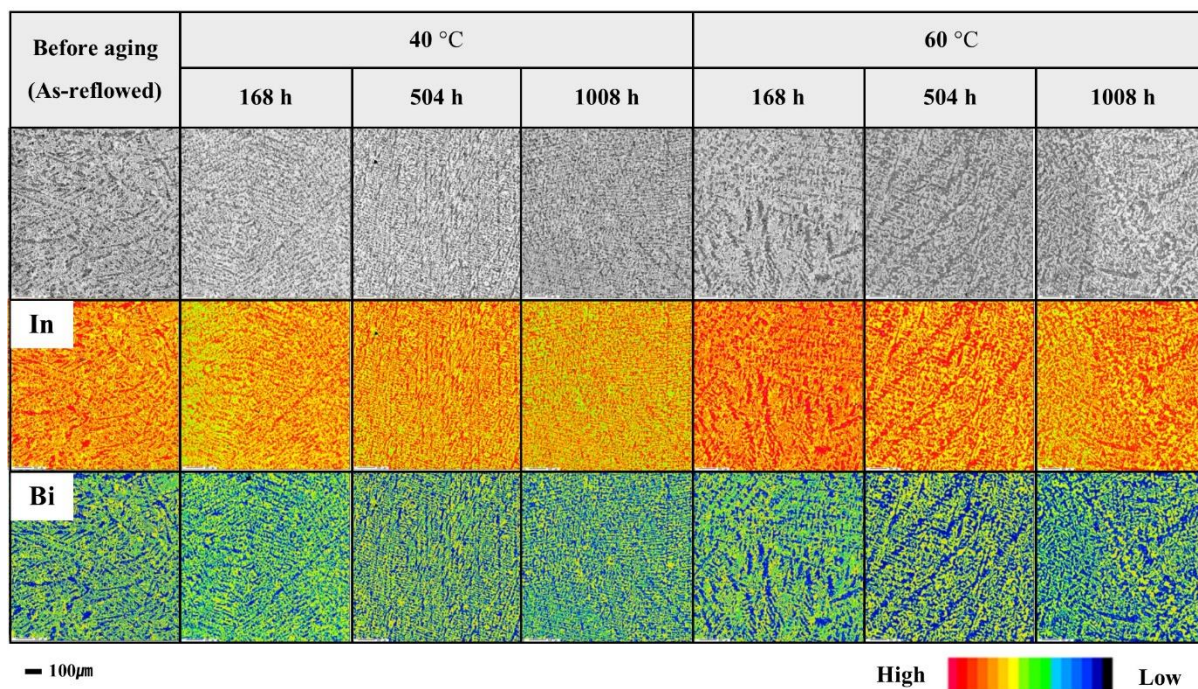


Figure 3.8 (continued)

Table 3.4 Energy-dispersive spectroscopy (EDS) point analysis results on point; A, B, C, and D.

Element	Point A (at. %)	Point B (at. %)	Point C (at. %)	Point D (at. %)
Bismuth	37.8	33.4	2.2	33.1
Indium	62.2	66.6	97.8	66.9
Total	100	100	100	100
Estimated phase	Bi ₃ In ₅	BiIn ₂	In-rich	BiIn ₂

equilibrium at high temperatures [10]. As shown in Table 3.5, after 1008 h of aging at 40 °C the eutectic spacing is maximized at 6.5 μm , approximately 1.27 times larger than that of the as-cast alloy. Especially after 1008 h of aging at 60 °C the eutectic spacing is maximized at 7.51 μm , approximately 1.47 times larger than that of the as-cast alloy. The eutectic spacing increased rapidly when thermal aged at higher temperature such as 60 °C.

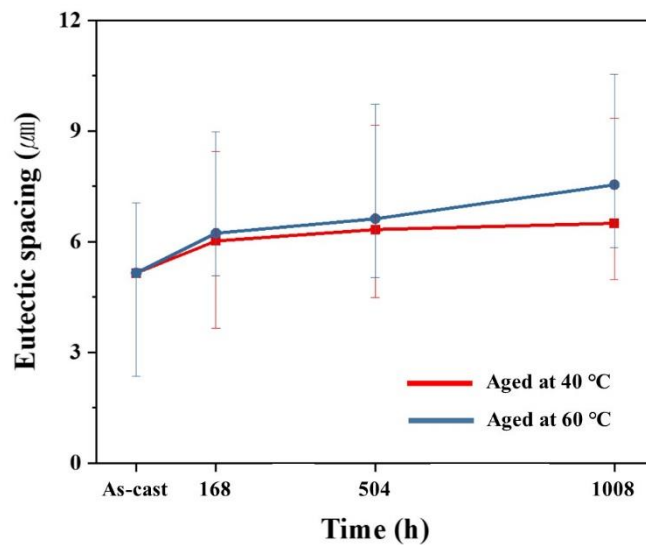


Figure 3.9 Average eutectic spacing within the eutectic In–33.7Bi alloy bulk before and after thermal aging.

As-cast	40 °C			60 °C		
	168 h	504 h	1008 h	168 h	504 h	1008 h
5.12 μm	6.02 μm	6.33 μm	6.50 μm	6.19 μm	6.59 μm	7.51 μm

3.4 Conclusions

In this chapter, the effects of In content on the melting properties and microstructure of In–Bi alloys under thermal aging were investigated. The following conclusions can be made:

- (1) The increase of indium amount in In–Bi alloys depressed their onset temperature. And the results of DSC did not change significantly even after thermal aging at 40 °C and 60 °C.
- (2) The XRD patterns of In–Bi alloys shows stable intermediate phase: Bi_3In_5 , BiIn_2 and In-phase.
- (3) The microstructure of the In–Bi alloys containing the primary In-phase, Bi_3In_5 , and BiIn_2 phases was investigated. The In-rich phase increased with In content. However, the microstructure did not change significantly during thermal aging.
- (4) In the case of In–33.7Bi, the eutectic spacing gradually increased during thermal aging. In case of 40 °C, becoming approximately 1.25 times larger than that of the as-cast alloy. In case of 60 °C, becoming approximately 1.47 times larger than that of the as-cast alloy.

References

- [1] JESD22-A103C, High Temperature Storage Life, JEDEC Standard, (2004)
- [2] Chiu, Tz-Cheng, et al., “Effect of thermal aging on board level drop reliability for Pb-free BGA packages”, 54th Electronic Components and Technology Conference, Vol. 2. IEEE (2004) 1256–1262
- [3] Coppola, L., et al., “Survey on high-temperature packaging materials for SiC-based power electronics modules”, Power Electronics Specialists Conference. IEEE (2007) 2234–2240
- [4] Watson, Jeff, and Gustavo Castro, “A review of high-temperature electronics technology and applications” *Journal of Materials Science: Materials in Electronics*, 26.12 (2015) 9226–9235
- [5] McCluskey, F. Patrick, et al., “Packaging reliability for high temperature electronics: A materials focus”, *Microelectronics International*, 13.3 (1996) 23–26
- [6] JIS Z 3198-1, The methods for lead-free solders-part 1: Methods for measuring of melting temperature ranges, *Jpn. Ind. Stand.*, (2003) 1–6
- [7] <http://www.icdd.com/>: International Center for Diffraction Data powder diffraction file cards
- [8] Jin, Sanghun, et al., “Microstructure and mechanical properties of indium–bismuth alloys for low melting-temperature solder”, *Journal of Materials Science: Materials in Electronics*, 29.19 (2018) 16460–16468
- [9] T. Hakakeyama, Z. Liu, “Handbook of Thermal Analysis”. Wiley, New York (1998) 6–13
- [10] H. Okamoto, P.R. Subramanian, L. Kacprzak, “Binary Alloy Phase Diagrams”, 2nd edn. ASM International, Materials Park, (1990) 748–750

Chapter 4

Mechanical properties of In-Bi alloys during isothermal aging

4.1 Introduction

In *Chapter 3*, the effects of In content on the melting property, phase constitution and microstructure of In–Bi alloys under thermal aging were investigated. And in this Chapter, the mechanical properties and fracture surface characteristics of In–Bi alloys under isothermal aging to test and analyze their thermal stability were investigated. In particular, the comparative analysis of mechanical properties and fracture surface characteristics through thermal aging will be a great help in understanding the thermal properties of In–Bi alloys. And predict that what characteristics will be exhibited when applied as actual bonding materials.

4.2 Experimental

4.2.1 Alloy preparation and aging process

The In and Bi used in this study were in the form of a pure metal sheet and shot, respectively, both which are commercially available. As shown in Table 4.1, In–Bi binary alloys were fabricated with as the same with chapter 3. Alloys with 50, 60, 66.3, and 70 mass% In (Nilaco., Tokyo, Japan, 99.99% pure) are herein referred to as In–50Bi, In–40Bi, In–33.7Bi (eutectic), and In–30Bi, respectively. These specimens were fabricated by dissolving the corresponding metallic sheet and shot in a furnace at 500 °C for 5 h. An equipoise with ± 0.1 mg accuracy was used to weigh the elements. The alloying process was performed in a graphite crucible, in air, with manual stirring every 30 min to ensure homogeneity. The molten alloy was then chill-cast in a steel mold to form a bar-type ingot with a length of 50 mm, width of 10 mm, and thickness of 5 mm. Before the thermal aging test the In–Bi alloys were remelted at 250 °C for 1 h in a crucible. Next, they were cast into bar-shaped steel molds and machined into dumbbell shapes for tensile testing using wire-cutting electrical discharge machines (AG360L, Sodick, Kanagawa, Japan). As shown in Figure 4.1, the dimensions of the gauge section of the tensile test specimens were 1.0 mm (depth) \times 2.0 mm (width) \times 10 mm (length). The dumbbell shape allows the fracture in the middle of the samples to be observed. After machining, SiC paper was utilized to polish the specimens mechanically, up to #2000 grit. Next, polycrystalline diamond spray (3 and 1 μm ; DP-spray P, Struers, Ballerup, Denmark) was used to further polish the specimens. The polished specimens were used for tensile testing after thermal aging. Eight repetitions of the tests were performed to collect the presented results and averages as shown in Table 4.1.

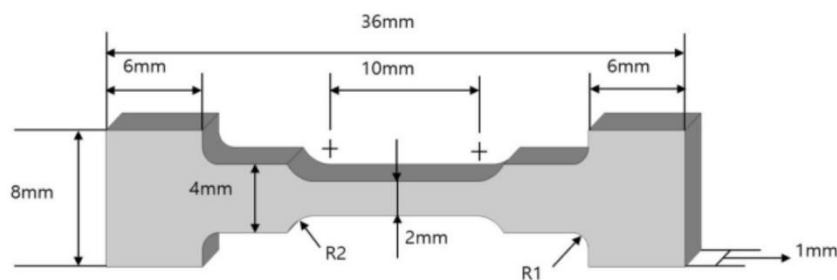


Figure 4.1 The geometry and size of the tensile test specimen.

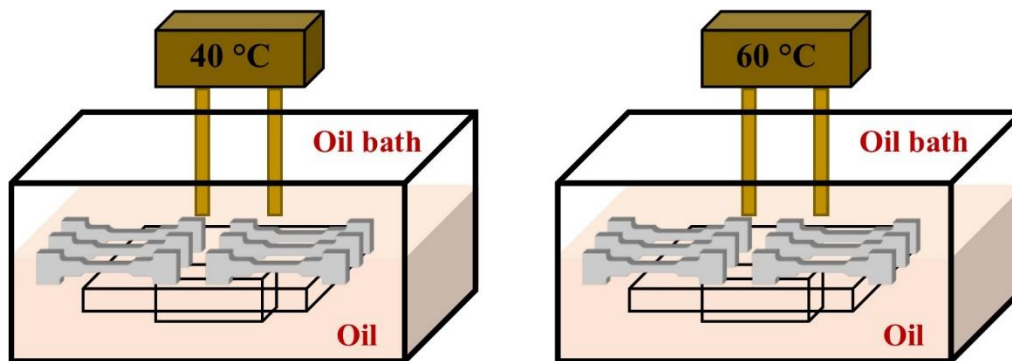


Figure 4.2 The illustration of thermal aging test.

Table 4.1 Sample size of thermal aging test

Temperature	Alloy system designations	108 h	504 h	1008 h	Sum.	Total
40 °C	In-50Bi	8	8	8	24	96
	In-40Bi	8	8	8	24	
	In-33.7Bi	8	8	8	24	
	In-30Bi	8	8	8	24	
60 °C	In-50Bi	8	8	8	24	96
	In-40Bi	8	8	8	24	
	In-33.7Bi	8	8	8	24	
	In-30Bi	8	8	8	24	

The samples were aged in an oil bath at a temperature of 40 °C and 60 °C for 168, 504, and 1008 h as shown in Fig 4.2. After aging, the samples were removed from the oil bath and cooled to 23 °C. The oil on the sample surfaces was removed with ethanol.

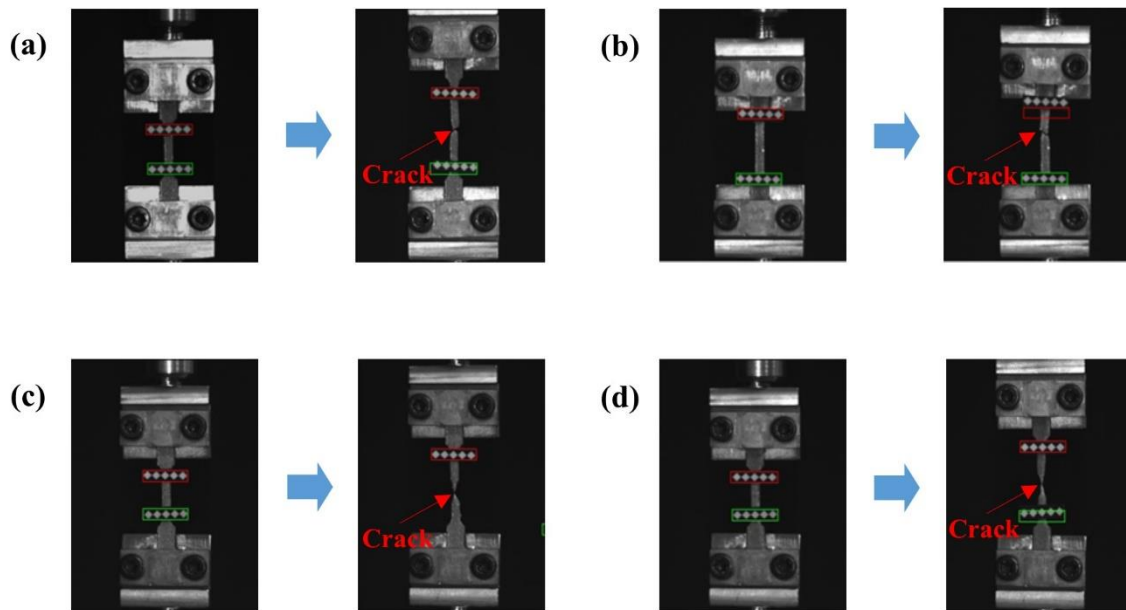


Figure 4.3 The image of the tensile test: (a) In–50Bi, (a) In–40Bi, (a) In–33.7Bi and (a) In–30Bi.

4.2.2 Tensile testing

As shown in Fig. 4.3, the mechanical properties of the In–50Bi, In–40Bi, In–33.7Bi, and In–30Bi alloys were evaluated by tensile testing. Tensile tests were conducted using a universal testing machine (Autograph AG-X, Shimadzu) at room temperature. Using the strain rate of 0.0005 s^{-1} , tensile properties such as the ultimate tensile strength (UTS) and elongation were obtained. Under the assumption of equivalence to the true test-strain, engineering stress–strain curves were used to present the stress–strain characteristics of the In–Bi alloys. This was possible due to their small deformation range. Further examination was performed using FE-SEM to closely analyze the necking and fracture surfaces of the In–Bi alloys after tensile testing.

4.3 Results and discussions

4.3.1 Mechanical properties.

Figure 4.4 shows the stress–strain curves of a specimen measured at room temperature. Figure 4.4(a) shows the S–S curve before thermal aging. The UTS and elongation of the In–

50Bi alloy, In–40Bi alloy, In–33.7Bi alloy, and In–30Bi alloy were 23.3 MPa and 41.9%, 14.8 MPa and 41.6%, 12.6 MPa and 55.7%, and 11.6 MPa and 74.8%, respectively. After thermal aging for 168 h at 40 °C, as shown in Figure 4.4(b), the UTS and elongation of the In–50Bi alloy, In–40Bi alloy, In–33.7Bi alloy, and In–30Bi alloy were 19.3 MPa and 45.3%, 13.1 MPa and 38.6%, 12.0 MPa and 53.8%, and 11.6 MPa and 74.2%, respectively. After thermal aging for 504 h at 40 °C, as shown in Figure 4.4(c), the UTS and elongation of the In–50Bi alloy, In–40Bi alloy, In–33.7Bi alloy, and In–30Bi alloy were 17.9 MPa and 43.1%, 12.3 MPa and 41%, 11.4 MPa and 57.3%, and 11.0 MPa and 78.4%, respectively. After thermal aging for 1008 h at 40 °C, as shown in Figure 4.4(d), the UTS and elongation of the In–50Bi alloy, In–40Bi alloy, In–33.7Bi alloy, and In–30Bi alloy were 16.3 MPa and 44.5%, 12.5 MPa and 45.3%, 11.9 MPa and 64.8%, and 10.9 MPa and 76.2%, respectively. Figure 4.5 shows the summarized tensile properties of the In–xBi alloys with error bar. The effect of thermal aging time is not large except for In–50Bi alloy when considering the average value with error bar. Figure 4.6 illustrates the relationship between the tensile properties and indium content. After thermal aging for 168 h at 40 °C, as shown in Figure 4.6(a), the UTS values of the In–50Bi alloy, In–40Bi alloy, In–33.7Bi alloy, and In–30Bi alloy were 19.3, 13.1, 12.0, and 11.5 MPa, respectively. After thermal aging for 1008 h, the UTS values of the In–50Bi alloy, In–40Bi alloy, In–33.7Bi alloy, and In–30Bi alloy were 16.3, 12.5, 11.9, and 10.9 MPa, respectively. The decrease in the UTS after thermal aging for 1008 h was smaller than that seen after 168 h. Even if the differences in the UTS decrease, the UTS values of the binary In–Bi alloys decrease with increasing In content. The reduction in UTS through the addition of In was most likely due to recrystallization, which leads to induced deformation [1]. As shown in Figure 4.6(b), specimen elongation was drastically increased for higher In content under both as-cast and thermal aging conditions. After thermal aging for 1008 h the elongation values of the In–50Bi alloy, In–40Bi alloy, In–33.7Bi alloy, and In–30Bi alloy were 44.5%, 45.3%, 64.8%, and 76.2%, respectively, as shown in Figure 4.6(b). Therefore, the elongation of binary In–Bi alloys increases with In content. Figure 4.7 illustrates how the tensile properties were affected by thermal aging time. For the as-cast and 1008 h aging conditions the UTS values of the In–50Bi were 23.3 and 16.3 MPa, respectively, as shown in Figure 4.7(a). The UTS of the 1008 h aged specimens compared to the as-cast specimens decreased by 29.8%. However, in the case of In–30Bi the UTS values were 11.6 and 10.9 MPa for the as-cast and thermally aged alloys, respectively. The reduction rate was 5.5%. The changes in UTS with aging time were not

significant except for in the case of In–50Bi, as shown in Figure 4.7(a). The elongation values of In–50Bi were 41.9% and 44.5% under the as-cast and 1008 h aging conditions, respectively, as shown in Figure 4.7(b). The elongation of the specimens aged for 1008 h increased by 6.2% compared to the as-cast specimens. In the case of In–30Bi, the elongations values were 74.8% and 76.2% in the as-cast and 1008 h aging conditions, respectively. The elongation of the specimens aged for 1008 h increased by 1.8% compared to the as-cast specimens. The changes in elongation with aging time were not significant, as shown in Figure 4.7(b).

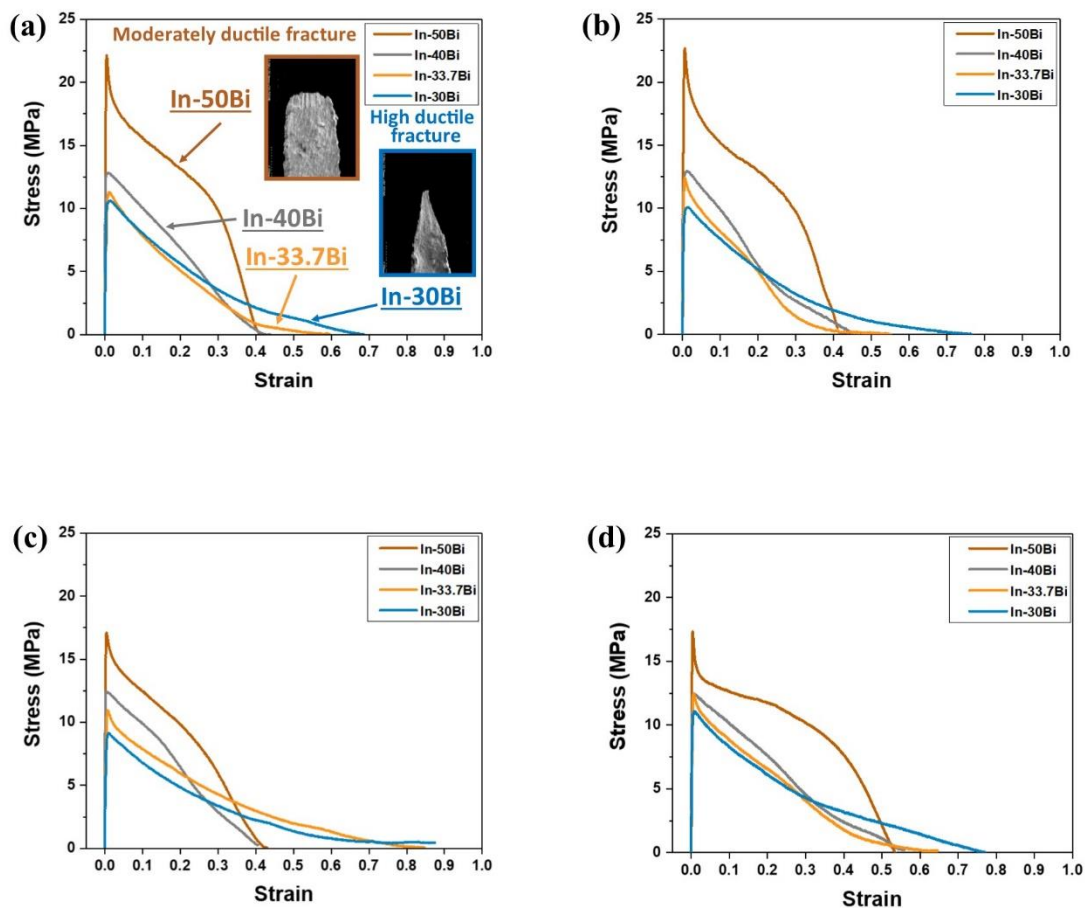


Figure 4.4 Tensile test results of In–Bi alloys: (a) as-cast and (b) thermally aged for 168 h, (c) 504 h, and (d) 1008 h at 40 °C.

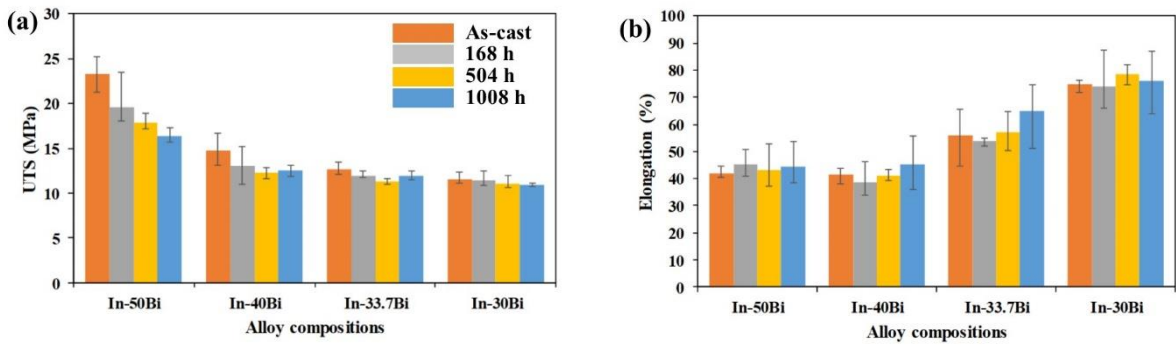


Figure 4.5 The effect of aging on the tensile properties of In–Bi alloys: (a) ultimate tensile strength (UTS) and (b) elongation at 40 °C.

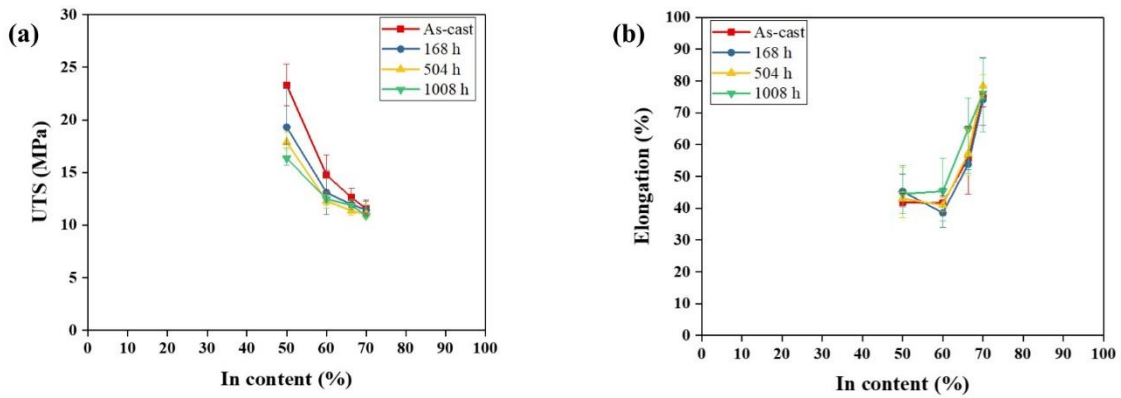


Figure 4.6 Tensile properties by indium content: (a) UTS and (b) elongation at 40 °C.

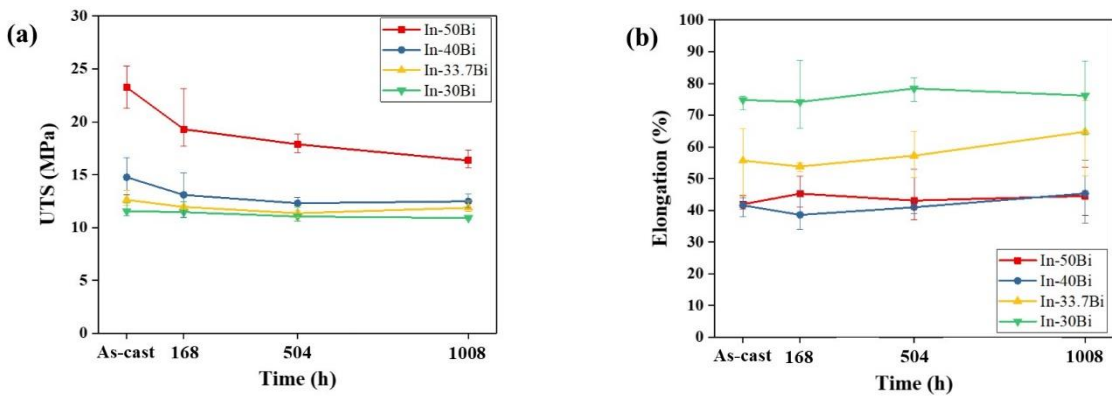


Figure 4.7 Tensile properties by thermal aging time: (a) UTS and (b) elongation at 40 °C.

And figure 4.8 shows the stress–strain curves at 60 °C. After thermal aging for 168 h at 60 °C, as shown in Figure 4.8(b), the UTS and elongation of the In–50Bi alloy, In–40Bi alloy, In–33.7Bi alloy, and In–30Bi alloy were 17.6 MPa and 43.6%, 13.0 MPa and 49.5%, 10.4 MPa and 66.1%, and 9.9 MPa and 75.2%, respectively. After thermal aging for 504 h at 60 °C, as shown in Figure 4.8(c), the UTS and elongation of the In–50Bi alloy, In–40Bi alloy, In–33.7Bi alloy, and In–30Bi alloy were 17.0 MPa and 48.6%, 12.3 MPa and 45.8%, 11.0 MPa and 65.6%, and 10.0 MPa and 70.5%, respectively. After thermal aging for 1008 h at 60 °C, as shown in Figure 4.8(d), the UTS and elongation of the In–50Bi alloy, In–40Bi alloy, In–33.7Bi alloy, and In–30Bi alloy were 16.7 MPa and 42.5%, 12.32 MPa and 43.4%, 10.9 MPa and 63.2%, and 9.8 MPa and 63.9%, respectively. Figure 4.9 shows the summarized tensile properties of the In–xBi alloys with error bar. The effect of thermal aging time is not large except for In–50Bi alloy when considering the average value with error bar. Figure 4.10 illustrates the relationship between the tensile properties and indium content. After thermal aging for 168 h at 60 °C, as shown in Figure 4.10(a), the UTS values of the In–50Bi alloy, In–40Bi alloy, In–33.7Bi alloy, and In–30Bi alloy were 17.6, 13.0, 10.4, and 9.9 MPa, respectively. After thermal aging for 1008 h, the UTS values of the In–50Bi alloy, In–40Bi alloy, In–33.7Bi alloy, and In–30Bi alloy were 16.7, 12.3, 10.9, and 9.8 MPa, respectively. The decrease in the UTS after thermal aging for 1008 h was smaller than that seen after 168 h. Even if the differences in the UTS decrease, the UTS values of the binary In–Bi alloys decrease with increasing In content. As shown in Figure 4.10(b), specimen elongation was drastically increased for higher In content under both as-cast and thermal aging conditions. After thermal aging for 1008 h at 60 °C, the elongation values of the In–50Bi alloy, In–40Bi alloy, In–33.7Bi alloy, and In–30Bi alloy were 43.6%, 49.5%, 66.1%, and 75.2%, respectively, as shown in Figure 4.10(b). Therefore, the elongation of binary In–Bi alloys increases with In content. Figure 4.11 illustrates how the tensile properties were affected by thermal aging time. For the as-cast and 1008 h aging at 60 °C conditions, the UTS values of the In–50Bi were 23.3 and 16.7 MPa, respectively, as shown in Figure 4.11(a). The UTS of the 1008 h aged specimens compared to the as-cast specimens decreased by 28.3%. However, in the case of In–30Bi the UTS values were 11.6 and 9.8 MPa for the as-cast and thermally aged alloys, respectively. The reduction rate was 15.5%. The changes in UTS with aging time were not significant except for in the case of In–50Bi, as shown in Figure 4.11(a). The elongation values of In–50Bi were 41.9% and 42.5% under the as-cast and 1008 h aging conditions, respectively, as shown in Figure 4.11(b). The elongation

of the specimens aged for 1008 h increased by 1.4% compared to the as-cast specimens. In the case of In-30Bi, the elongations values were 74.8% and 63.9% in the as-cast and 1008 h aging conditions, respectively. The elongation of the specimens aged for 1008 h decreased by 14.6% compared to the as-cast specimens. Compared with the UTS for all alloys, the changes in elongation with aging time were not significant, as shown in Figure 4.11(b).

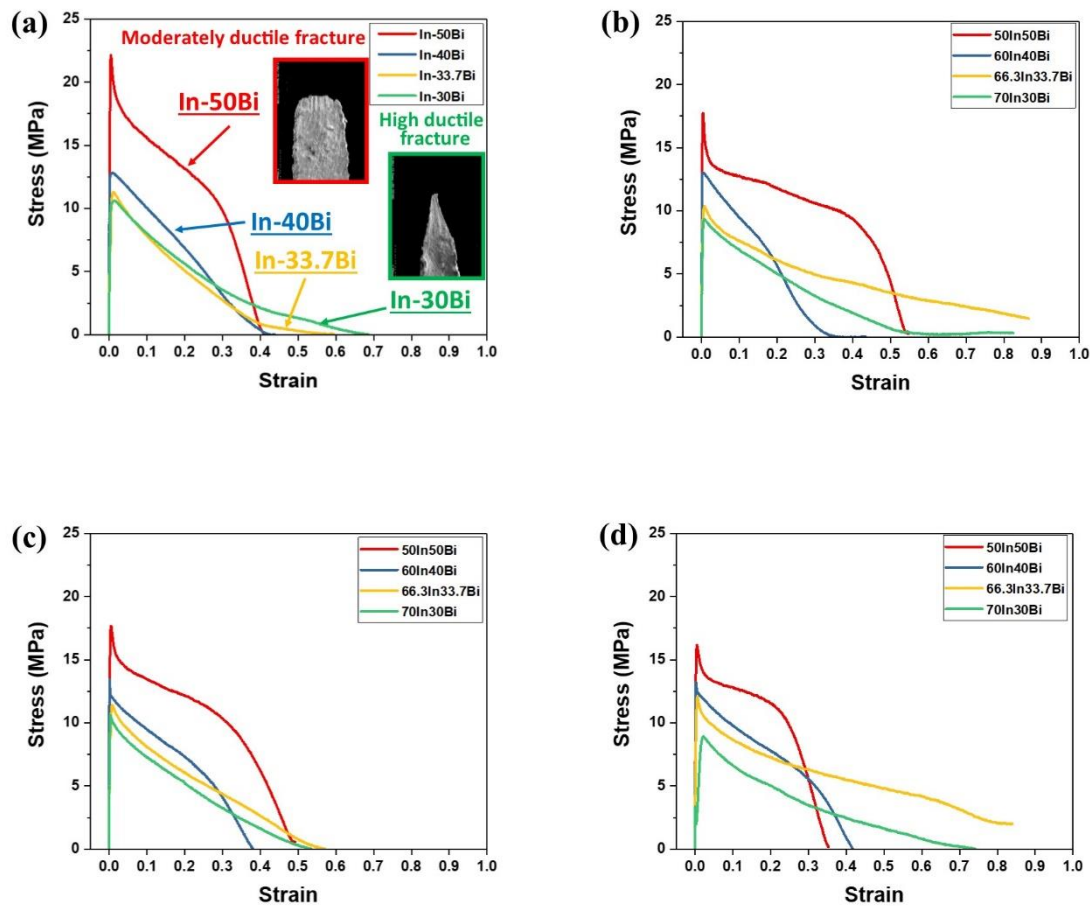


Figure 4.8 Tensile test results of In-Bi alloys: (a) as-cast and (b) thermally aged for 168 h, (c) 504 h, and (d) 1008 h at 60 °C.

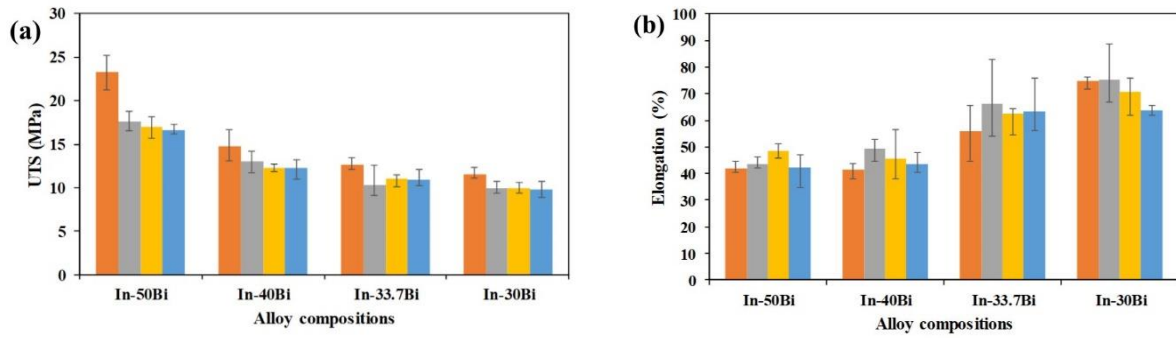


Figure 4.9 The effect of aging on the tensile properties of In–Bi alloys: (a) ultimate tensile strength (UTS) and (b) elongation at 60 °C.

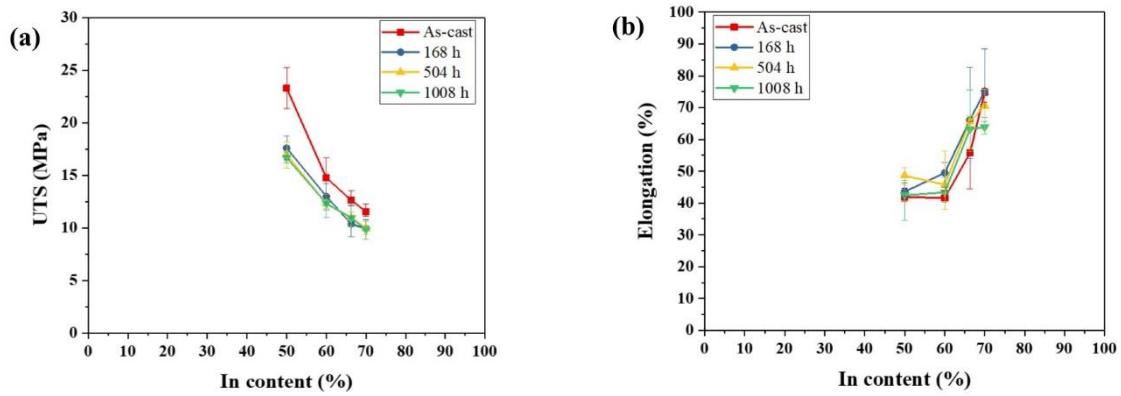


Figure 4.10 Tensile properties by indium content: (a) UTS and (b) elongation at 60 °C.

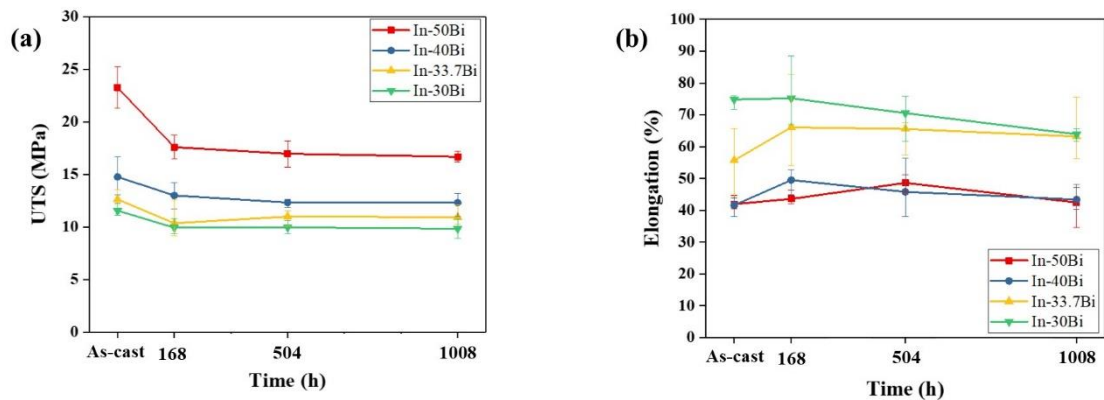


Figure 4.11 Tensile properties by thermal aging time: (a) UTS and (b) elongation at 60 °C.

The observed large increase in ductility may be caused by the addition of excess In to the binary In–Bi alloys, which causes In-rich phases to form [2]. Furthermore, the addition of excess In to the In–Bi system implies a comparatively smaller amount of Bi, which is brittle by nature, in the system, resulting in a more ductile behavior. In–Bi alloys exhibited stress–strain curves that were considerably different from those of Sn-based alloys, as shown in Figure 4.4. and 4.8. For In–50Bi, which had the smallest amount of In of the tested alloys, the elastic–plastic transition showed a sharp bend in the stress–strain curve. The deformation of In–Bi alloys can be approximated as ideal plastic behavior. Increasing the reduction in the cross-sectional area up to the neck of the sample can lead to a decrease in the measured load. Increasing the In content not only greatly increases the elongation property, but also causes the reduction in area to remain extremely high. As expected, the thermally aged In–Bi alloys showed outstanding low-temperature deformation properties owing to their stable thermal behaviors.

4.3.2 Fracture modes

The as-cast and thermally aged specimens with different alloy compositions were observed after tensile testing, as shown in Figure 4.12. Generally, ductile fractures are caused by a simple overload of a ductile material [3]. In-based alloys exhibit outstanding low-temperature deformation properties [4]. As expected, In–33.7Bi and In–30Bi exhibited high ductility as shown in Fig. 4.13. As is common for soft alloys, the fracture surfaces showed ductile fracture features in the neck shapes for all In–Bi alloys. The different neck shapes appeared according to the In content, due to its ductility. As shown in Figure 4.14(a), post necking led to a moderate ductile fracture in In–50Bi, which contained the lowest In content. On the tip of the fracture surface of the In–50Bi alloy an irregular and fibrous appearance was observed. However, alloys with greater In contents, such as In–33.7Bi and In–30Bi, also showed high ductility, as represented by reductions in the cross-sectional areas approaching 90 and 100%, respectively, as shown in Figure 4.15. Eventually, the contact area becomes too small to support the load, resulting in fracture. The specimen necks to a point; this type of failure is typically called rupture [5]. This can also be seen in Figure 4.16(b). As the In content increases, the neck width decreases. In particular, In–30Bi showed a reduction in the neck width to a dot-like shape; it also showed the highest ductility of the tested In–Bi alloys. As mentioned

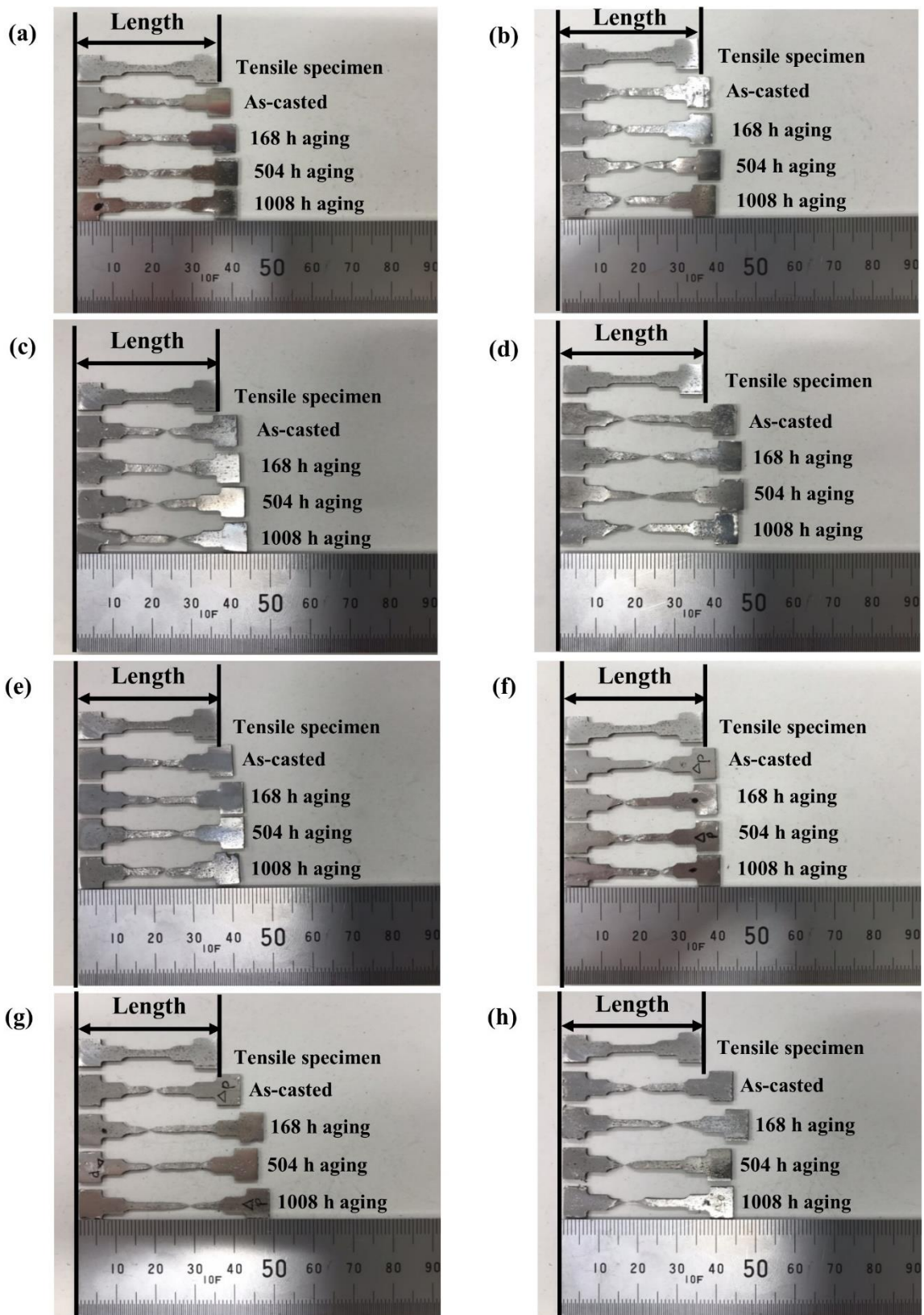
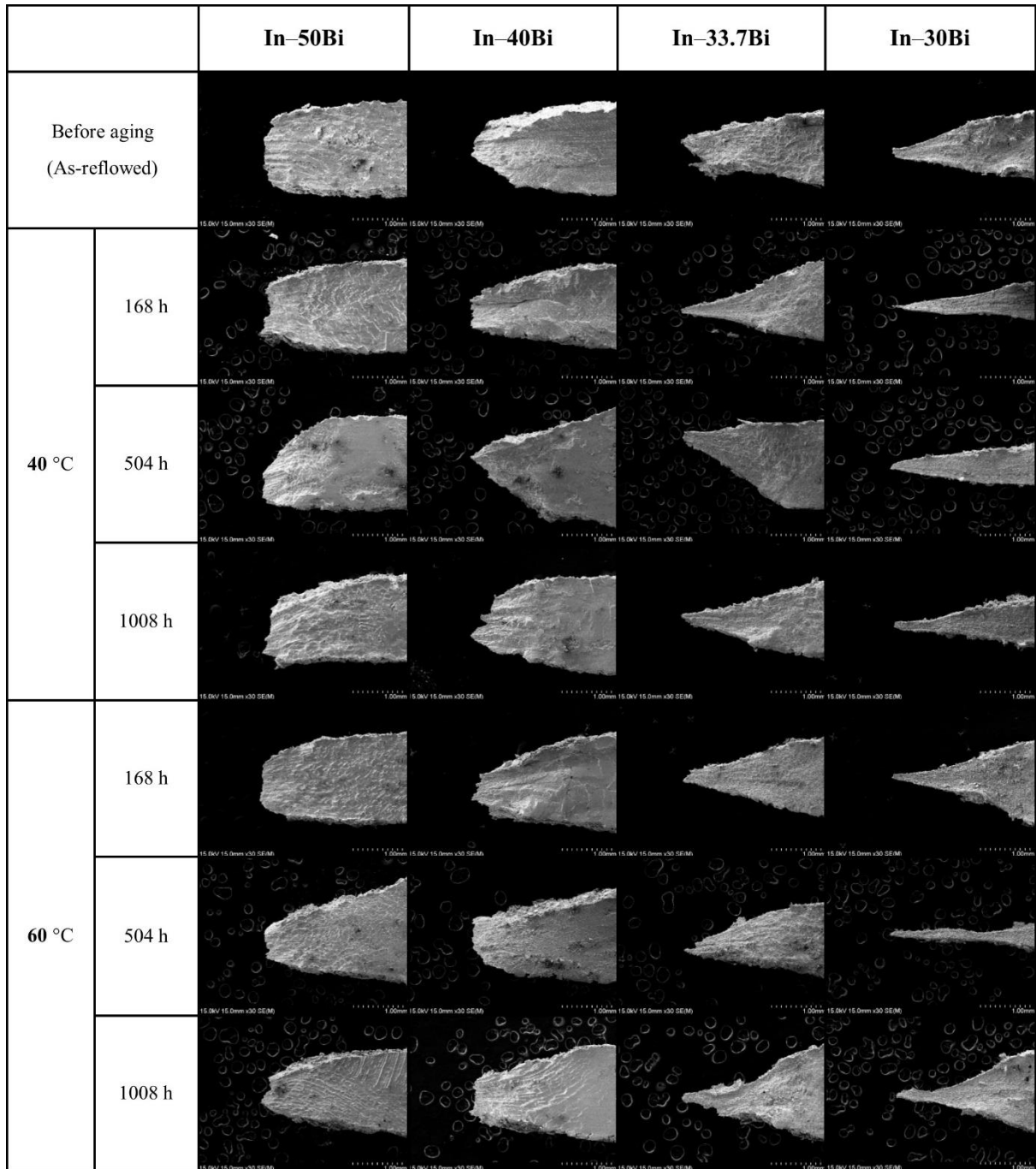


Figure 4.12 Photographs of the bulk specimens after tensile tests for observing change in length of In–Bi alloys: (a) In–50Bi, (b) In–40Bi, (c) In–33.7Bi and (d) In–30Bi thermally aged at 40 °C. And (e) In–50Bi, (f) In–40Bi, (g) In–33.7Bi and (h) In–30Bi thermally aged at 60 °C.



1.00 mm

Figure 4.13 Fracture surfaces of tensile specimens by thermal aging time (side view).

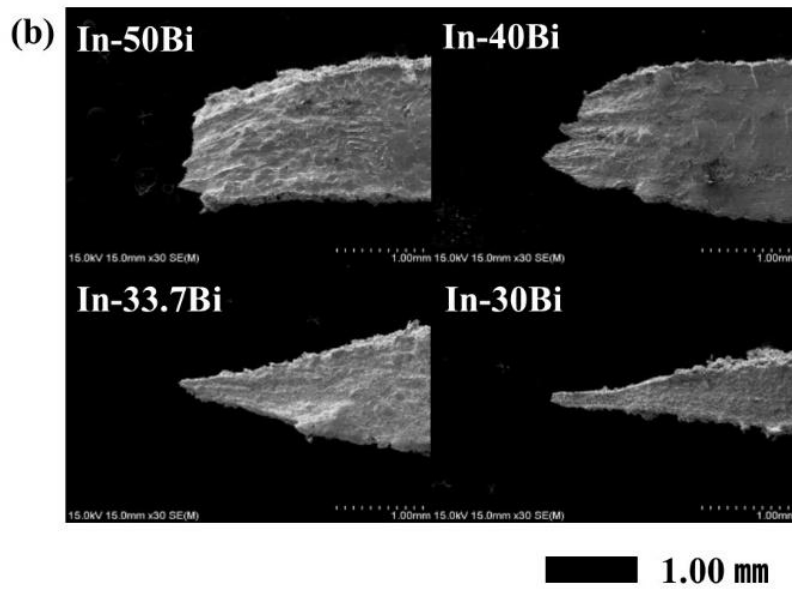
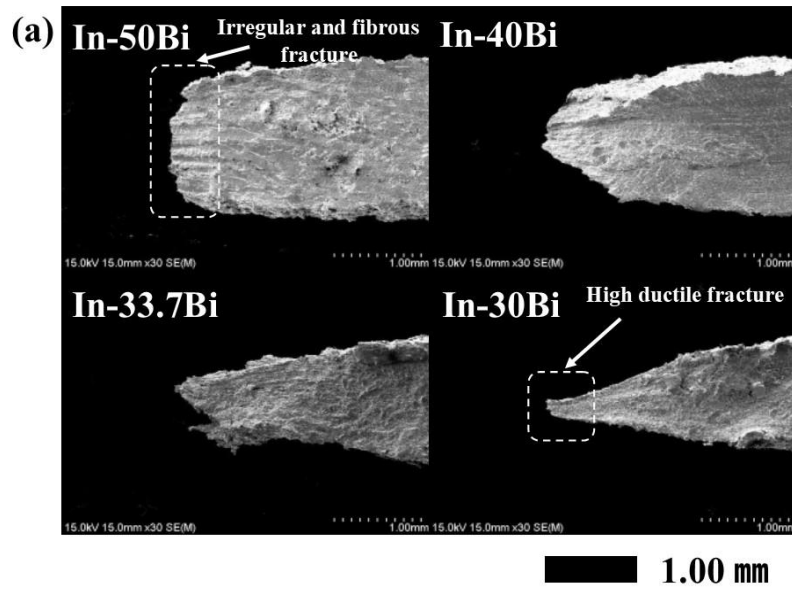
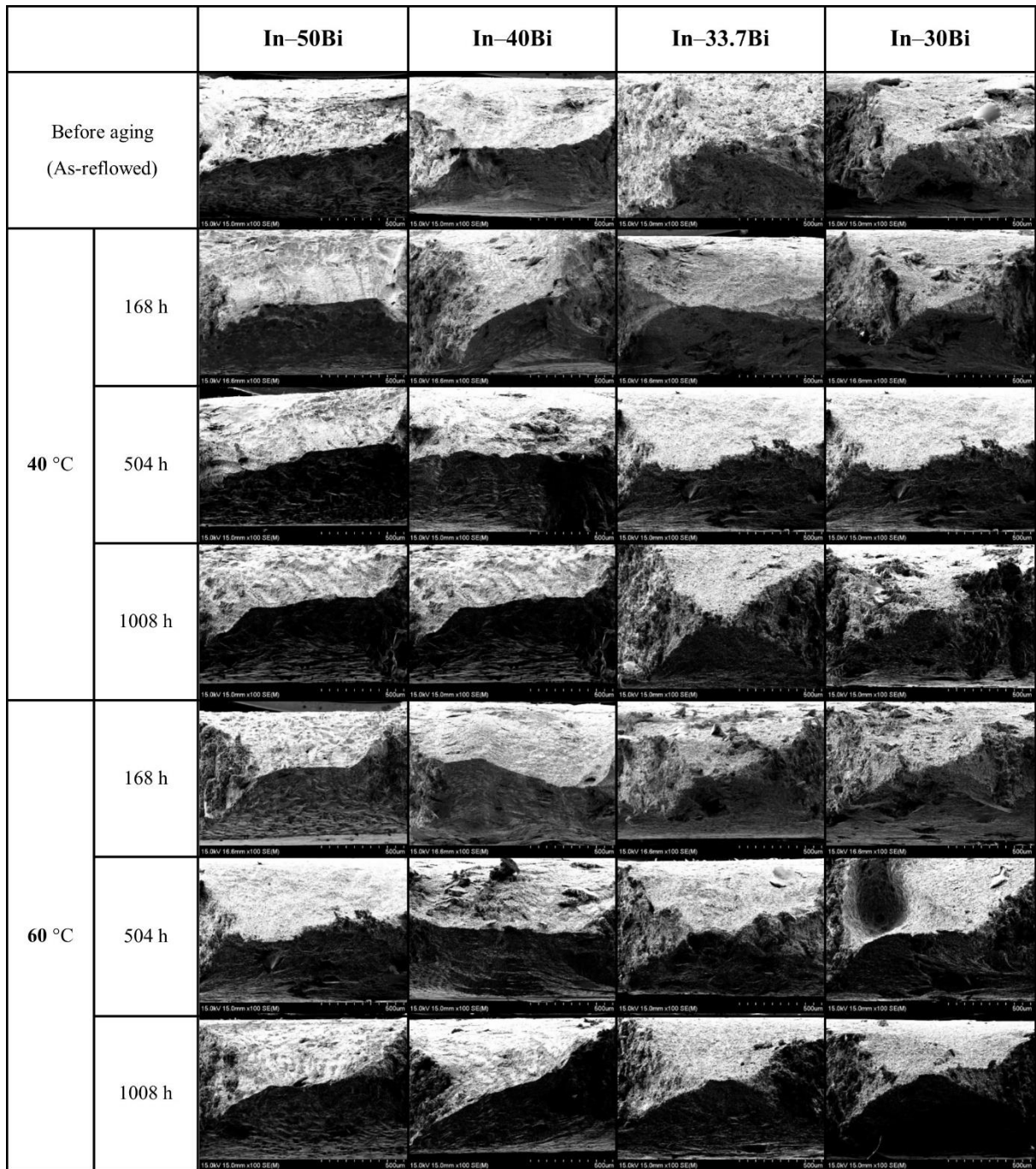


Figure 4.14 Fracture surfaces of tensile specimens (side view): (a) as-cast and (b) thermally aged for 1008 h at 40 °C.



500 μm

Figure 4.15 Fracture surfaces of tensile specimens by thermal aging time (top view).

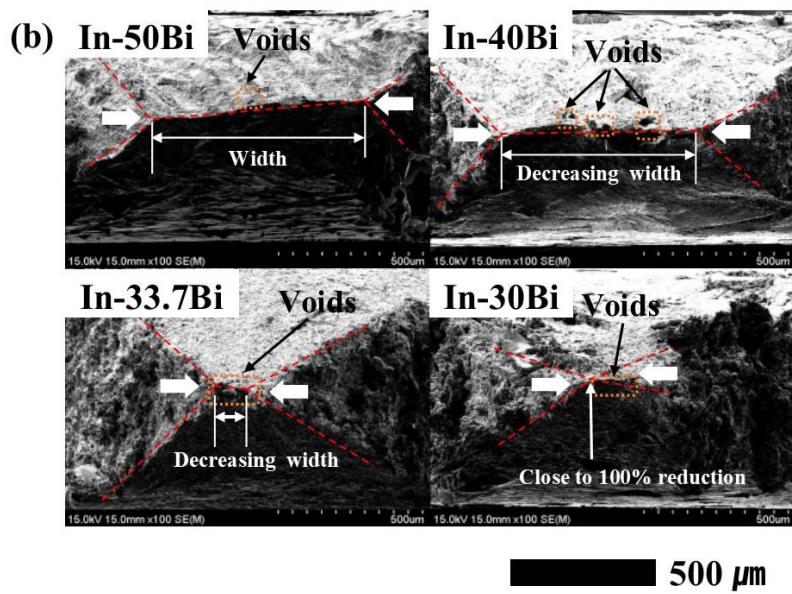
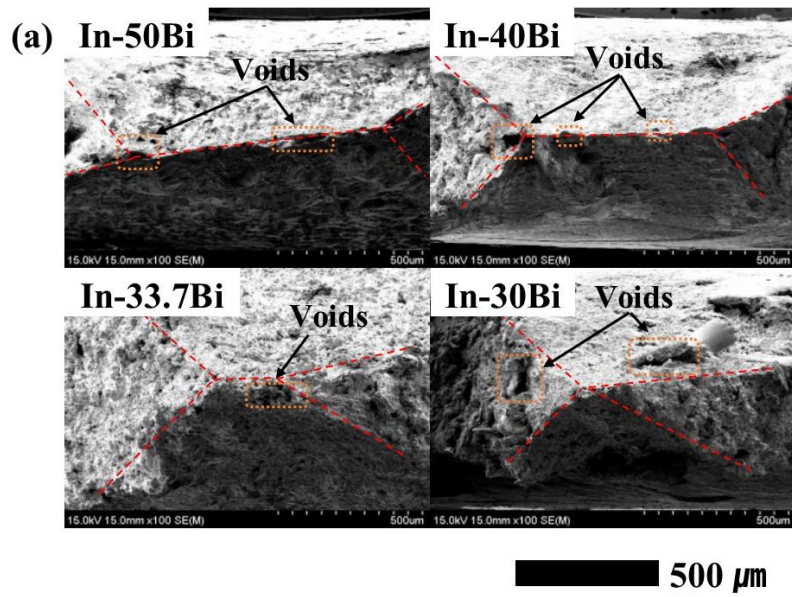


Figure 4.16 Fracture surfaces of tensile specimens (top view): (a) as-cast and (b) thermally aged for 1008 h at 40 °C.

in our previous study (Chap. 2) [6], ductile fracture is accompanied by necking and the nucleation and coalescence of microvoids. Small spherical voids form under high stress, causing the fracture of the alloy at the grain boundaries, as shown in Figure 4.16. As shown in Figure 4.17, in the case of In-30Bi the microvoids grew and coalesced into larger cavities when there was an increase in the local stress. Finally, no significant differences in fracture surfaces were observed between the as-cast and thermally aged specimens.

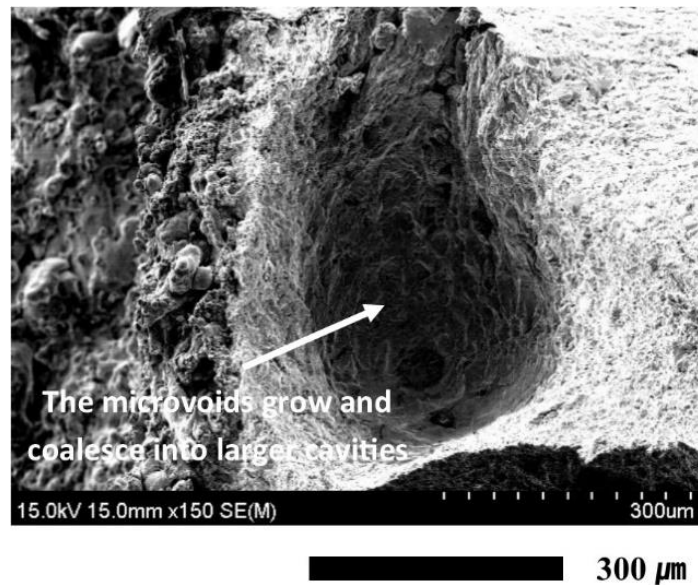


Figure 4.17 The morphology of a ductile fracture.

3.4 Conclusions

In this chapter, the effects of In content on the microstructure and mechanical properties of In–Bi alloys under thermal aging were investigated. The following conclusions can be made:

- (5) The UTS of In–Bi alloys decreased with increasing indium content and thermal aging time. However, the changes in UTS with aging time were not significant, except for in the case of In-50Bi.
- (6) The elongation of In–Bi alloys was drastically increased with increasing In content in both the as-cast and thermally aged specimens. However, the elongation behavior of these alloys did not change significantly after thermal aging. The thermally aged In–Bi alloys showed outstanding low-temperature deformation properties due to their stable thermal behaviors.
- (7) The In–Bi alloys showed typical ductile fractures. An increase in In content decreased the cross-sectional area of the tensile sample, indicating high ductility. The elongation and the area reduction remained very high at the aging temperature.

References

- [1] R.P. Reed et al., “Tensile strength and ductility of indium”, *Mater. Sci. Eng. A*, 102(2) (1988) 227–236
- [2] M. Plotner, B. Donat, A. Benke, “Deformation properties of indium-based solders at 294 and 77 K”, *Cryogenics*, 31(3) (1991) 159–162
- [3] Benzerga, A.A.; Leblond, J.-B., “Ductile fracture by void growth to coalescence” *Adv. Appl. Mech.*, (2010) 44, 169–305
- [4] Cheng, X. A., “Study on Indium Joints for Low-Temperature Microelectronics Interconnections” Ph.D. Thesis, Loughborough University, Loughborough, UK, (2011) 74–178
- [5] Askeland, D.R.; Phulé, P.P., “Microstructural features of fracture in metallic materials. In *The Science and Engineering of Materials*”, Thomson Learning: Toronto, ON, Canada, (2003) 230–233
- [6] Jin, Sanghun, et al., “Microstructure and mechanical properties of indium–bismuth alloys for low melting-temperature solder”, *Journal of Materials Science: Materials in Electronics*, 29.19 (2018) 16460–16468

Chapter 5

Shear properties of In-Bi alloy joints with Cu substrates

5.1 Introduction

In previous chapter, the effects of In content on the material properties of In–Bi alloys under thermal aging were investigated. Based on the microstructure and mechanical of In–Bi alloys, In–Bi alloys can be expected to have good thermal stability. And In–Bi alloys with low melting temperatures are promising candidates for flexible electronics applications as well as for devices with PP- and PMMA-based substrates. Therefore, the purpose of this chapter is to evaluate the shear strengths of the Cu/In–Bi alloy/Cu joints and analyze the interfacial reactions as a function of isothermal aging to evaluate their long-term reliability. An isothermal aging test has been generally performed in order to examine the durability of die attach for high temperature electronics on the thermal stress induced by coefficient of thermal expansion (CTE) mismatch between the dissimilar materials under temperature fluctuation [1]. So it is necessary to investigate on the long-term reliability of In–Bi alloy joint under isothermal temperature for the replacement of low-melting temperature such as Sn–Bi and Sn–Zn [2, 3]. Especially, the fracture behavior of In–Bi alloy joint and microstructural change were examined

in order to reveal the relationship between the microstructural characteristics at the bonding interface and joint strength of In–Bi joint.

5.2 Experimental

5.2.1 Joint sample preparation

We selected four alloy compositions with 50, 60, 66.3, and 70 mass % In, denoted as In–50Bi, In–40Bi, In–33.7Bi, and In–30Bi, respectively. The alloys are the same with chapter 2, 3 and 4. The In–Bi alloys were prepared from indium (99.99% pure, Nilaco) and bismuth (99.99% pure, Nilaco) as starting materials. Each alloy was melted in a furnace at 500 °C for 5 h before being cast in a steel mold. The alloying process was performed in air and the molten alloys were frequently stirred to ensure homogeneity. Alloy sheets were fabricated by casting and cold rolling processes. Then, the alloy sheets were sandwiched between oxygen free Cu discs. Before making a Cu/In–Bi alloy/Cu joint sample, 10 -mm diameter Cu discs were cleaned using 4 vol.% HCl and ethanol as shown in Fig. 5.1(a). An alloy sheet with the thickness of 200 μm was put on the 10 mm diameter Cu disc and a mildly activated 12 wt.% rosin flux was dropped. Then 3-mm diameter Cu discs, which were cleaned using the aforementioned method, were placed on top of the alloy sheet, as shown in Fig. 5.1(a). The joint samples were placed inside the reflow oven (Sanyo Seiko SMT Scope SK-8000), preheated at 50 °C for 90 s, and heated to 100 °C for 600 s in a nitrogen atmosphere. The set heating profile and measured temperature profile of this process are shown in Fig. 5.1(b). In this study, over six samples were used as the average for each alloy composition as shown in Table 5.1.

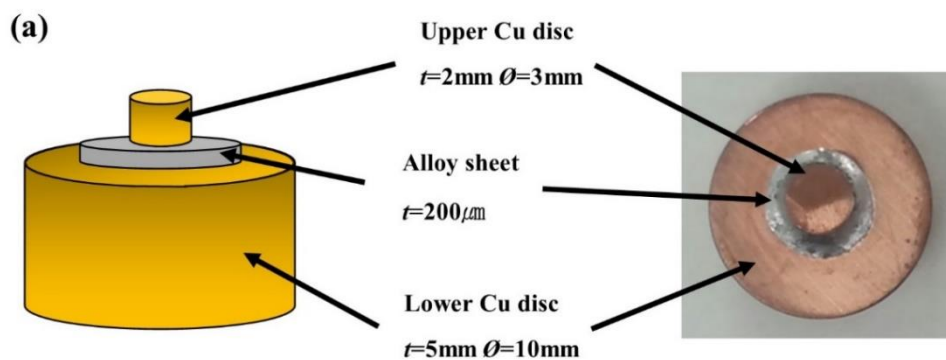


Figure 5.1 Illustration of the heating process: (a) a schematic diagram of the Cu–Cu joint and real joint sample (b) the heating profile of the process.

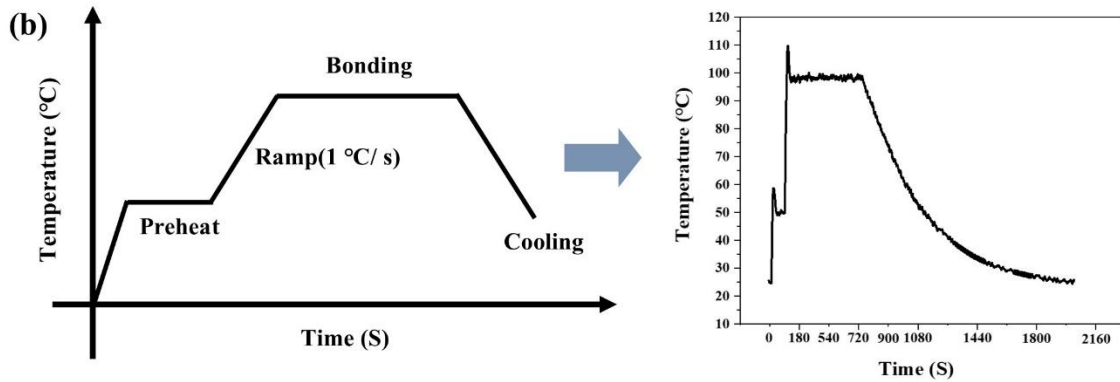


Figure 5.1 (continued)

5.2.2 Thermal aging and IMC thickness measurement

The Cu–Cu joint samples were aged at 40 and 60 °C for 168, 504, and 1008 h in an oil bath to evaluate the morphology and intermetallic compound (IMC) growth near the interface between the alloy and Cu disc. The IMC thickness at the interface was measured and analyzed to identify the phases in a cross-section of the joint sample. The thicknesses of the IMC layers were determined using ImageJ quantitative analysis software. The average thickness was

Table 5.1 Sample size of thermal aging test

Temperature	Alloy composition	108 h	504 h	1008 h	Sum.	Total
40 °C	In–50Bi	6	6	6	18	72
	In–40Bi	6	6	6	18	
	In–33.7Bi	6	6	6	18	
	In–30Bi	6	6	6	18	
60 °C	In–50Bi	6	6	6	18	72
	In–40Bi	6	6	6	18	
	In–33.7Bi	6	6	6	18	
	In–30Bi	6	6	6	18	

calculated by measuring the area of the compound and dividing it by the total length of the compound. In this work, the thickness of the IMC layers was reported as an average over three locations. Two repetitions of the measurement of each composition were performed to collect the presented results and averages.

5.2.3 Shear strength test

Shear tests were performed on as-reflowed and thermally aged joint samples. The joint samples were clamped on the testing machine (STR-1000, Rhesca) and shear tests were conducted at a crosshead speed of 1 mm/min at room temperature, as shown in Fig. 5.2. The shear strength was determined by dividing the shear force at failure by the area of the alloy. In this work, the shear strength was reported as the average over four samples for each alloy composition.

5.2.4 Microstructural characterization

The reflowed and aged samples were mounted in epoxy and cross-sectioned by mechanical polishing to observe their microstructure using scanning electron microscopy (SEM, SU-70, Hitachi). Cu/In–Bi alloy/Cu joint samples were cut and ground with 400#, 800#, 1200#, and 2000# SiC paper, then carefully polished using polishing pastes. The compositions of the IMC layers and bulk alloys were analyzed by elemental point analysis using an energy-dispersive x-ray spectrometer (EDS, Oxford Instruments). The elemental mapping of the microstructure was conducted by electron probe microanalyzer (EPMA, JXA-8530F, JEOL).

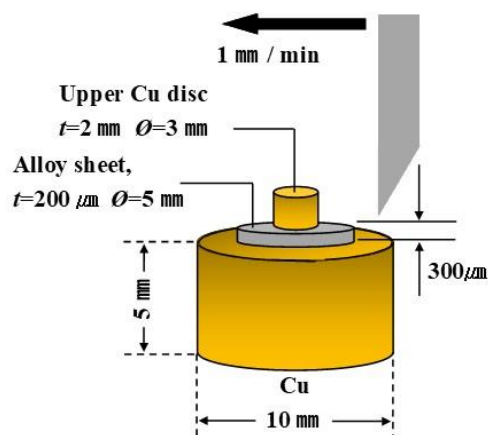


Figure 5.2 Schematic illustration of the shear test.

5.3 Results and discussions

5.3.1 Cross-sectional microstructure of Cu/In–Bi alloy/Cu joints

Prior to shear testing, the cross-sectional microstructures of the joints were observed. Fig. 5.3(a) shows the microstructures of the In–Bi alloy part of the joint samples as reflowed. Indium was detected as the In-rich phase and Bi was observed in the form of Bi_3In_5 and BiIn_2 , as shown in Fig. 5.3. It was confirmed that the In–Bi alloy part of the joint samples contains intermediate phases: Bi_3In_5 , BiIn_2 and a primary In-phase. In the case of In–50Bi, it appeared as a result of a peritectic reaction, where the liquid and the BiIn solid-solution phase were isolated by the Bi_3In_5 phase [4]. In–40Bi appeared to be a hypoeutectic alloy in which the eutectic reaction resulted in a transformation to a lamellar mixture of In and BiIn_2 phases. The In–33.7Bi alloy formed lamellar microstructures in which In-rich and BiIn_2 phases were inter-

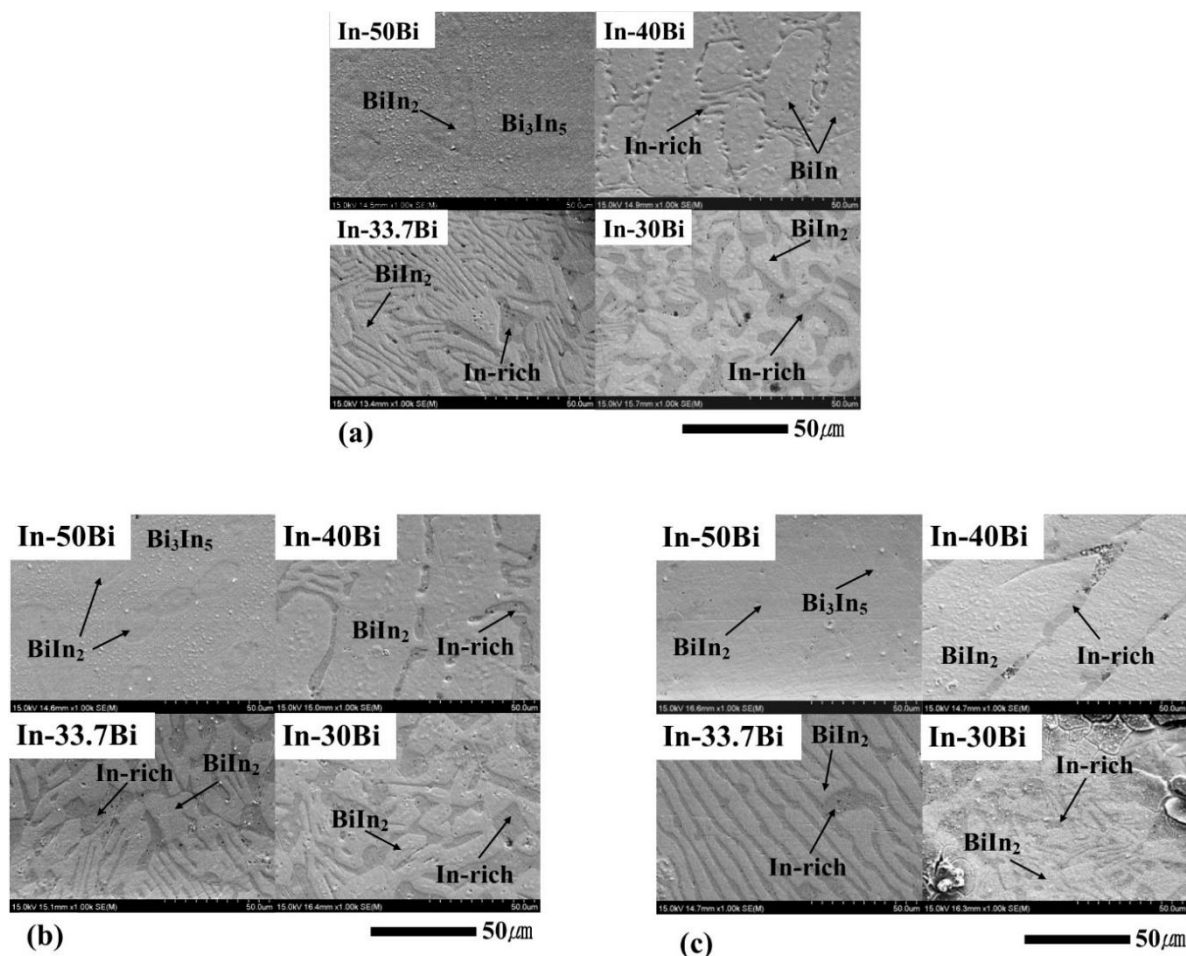


Figure 5.3 Cross-sectional microstructure of In–Bi alloys (a) as reflowed, (b) thermally aged for 1008 h at 40 °C and (c) 60 °C.

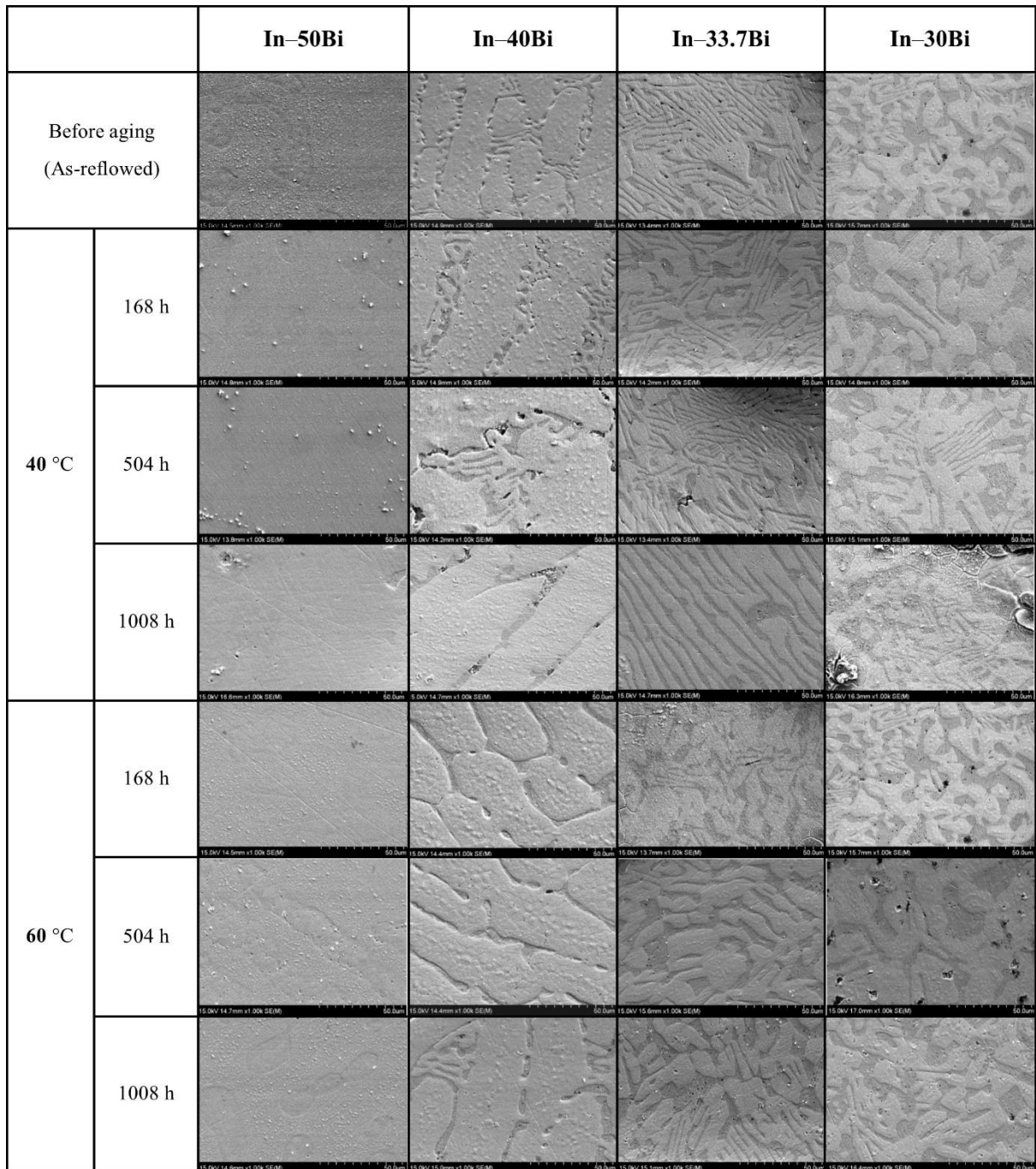


Figure 5.4 Cross-sectional microstructure of In-Bi alloys as reflowed and thermally aged.

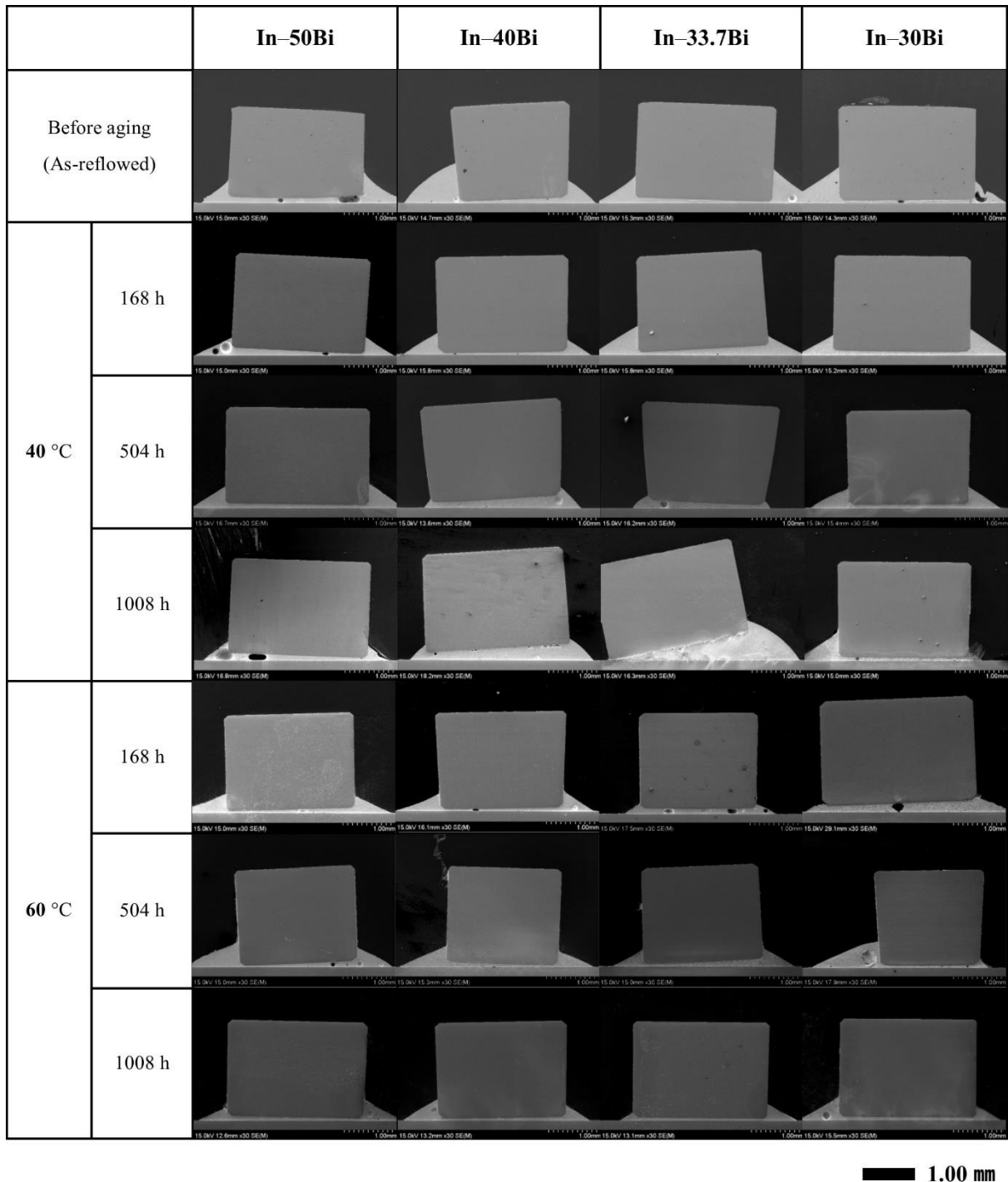


Figure 5.5 Cross-sectional image of In-Bi alloys as reflowed and thermally aged.

locked with each other in a eutectic composition. The bright and dark regions in the SEM images shown in Fig. 5.3 represented In and BiIn₂, respectively. The In-30Bi case appeared as a hypereutectic alloy. It had a eutectic structure because its composition was very close to the In-33.7Bi alloy. The compositions of the In-Bi IMCs were investigated using EDS elemental point analysis and compositions were decided. Fig. 5.4 shows the BiIn₂ phase was coarsened after thermal aging at 40 and 60 °C for 1008 h except In-50Bi. The coarsened BiIn₂ phase was considered as one of the reasons to explain how shear strength was affected after thermal aging applied for more than 168 h at 40 and 60 °C. As shown in Fig. 5.4, the results of microstructure did not change significantly even after thermal aging at 40 and 60 °C. It means that there is no new phase generated by the reaction same as tensile specimens in chapter 3. As shown in Fig. 5.5, the fillet shape of the In-Bi alloy joints was fine overall. And no big void was observed.

5.3.2 Morphology of interfacial and growth rate of IMCs after thermal aging

Cross-sectional EPMA images of the interface after thermal aging for 1008 h at 40 and 60 °C are shown in Fig. 5.6. The interfacial IMC phases formed between the In-Bi alloys and Cu substrates were investigated thoroughly using EPMA after reflowing and after thermal aging. As we know, the Sn-based solder has the scallop-like morphology of IMC after reflow [5, 6]. However, In-Bi alloy joints exhibited layer-like morphology except In-50Bi. And the In-50Bi showed the non-uniform morphology on IMC phases. These were identified as Cu_xIn_y IMCs, owing to the participation of In in the interfacial reactions between the In-Bi alloys and Cu substrates. However, as EPMA mapping observations could not provide sufficient information to fully determine the interfacial IMC phases, further composition analyses were carried out using point analysis of the EPMA data, and the results are shown in Table 5.2. The exact morphologies of the formed IMCs could be observed as shown in Fig. 5.7. Elemental analyses using point analysis revealed that the IMC layer has a composition close to 80.6In-18.9Cu-0.5Bi (mass %).

Fig. 5.8 shows SEM images of the interfacial IMC layers of the as-reflowed and thermally aged In-Bi alloy joints after aging for 168, 504 and 1008 h at 40 and 60 °C. Fig. 5.9 shows the results of the IMC thickness measurements after thermal aging. As the amount of indium was

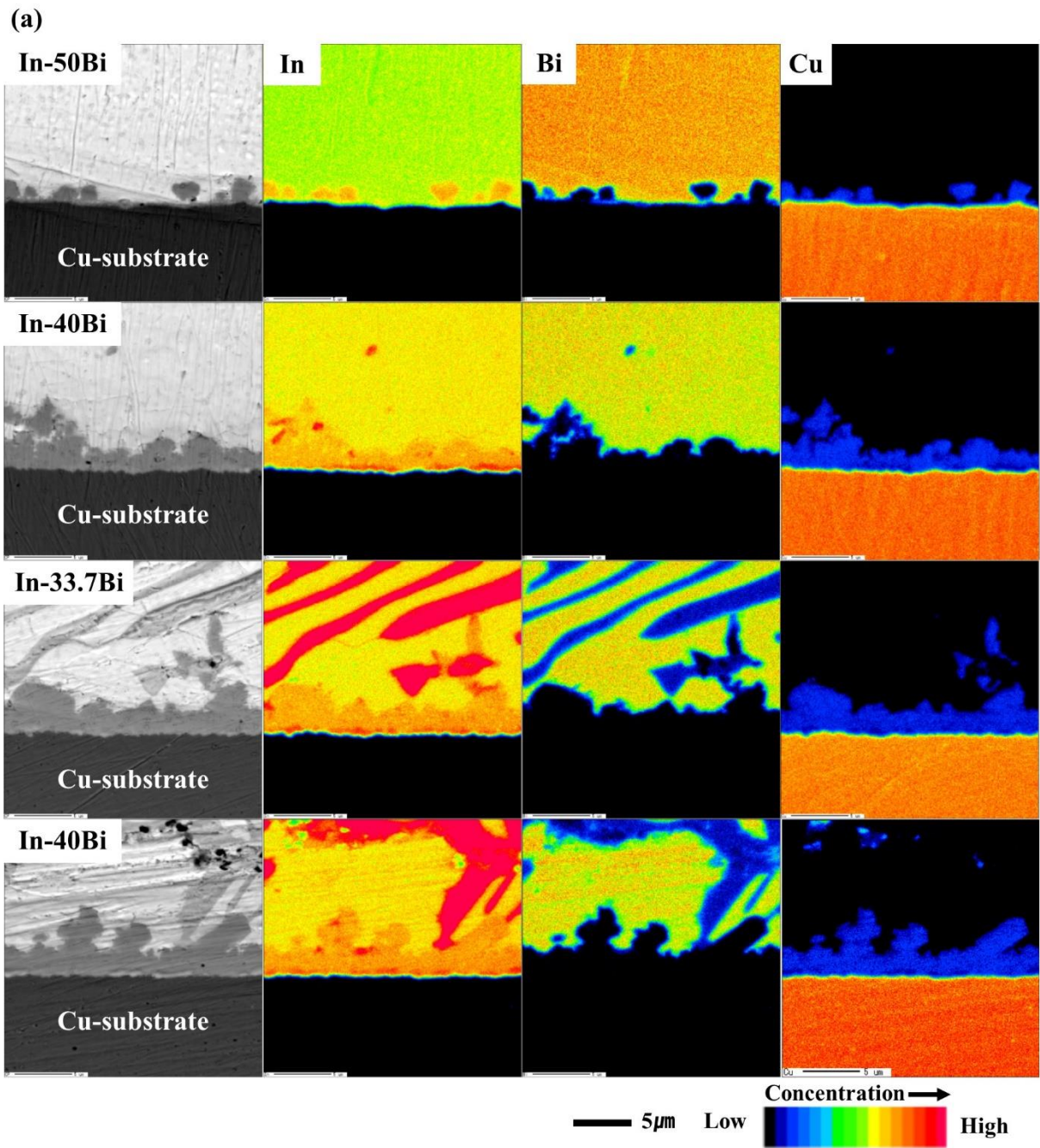


Figure 5.6 EPMA mapping results of In-Bi alloys after thermal aging for 1008 h (a) at 40 °C and (b) at 60 °C.

(b)

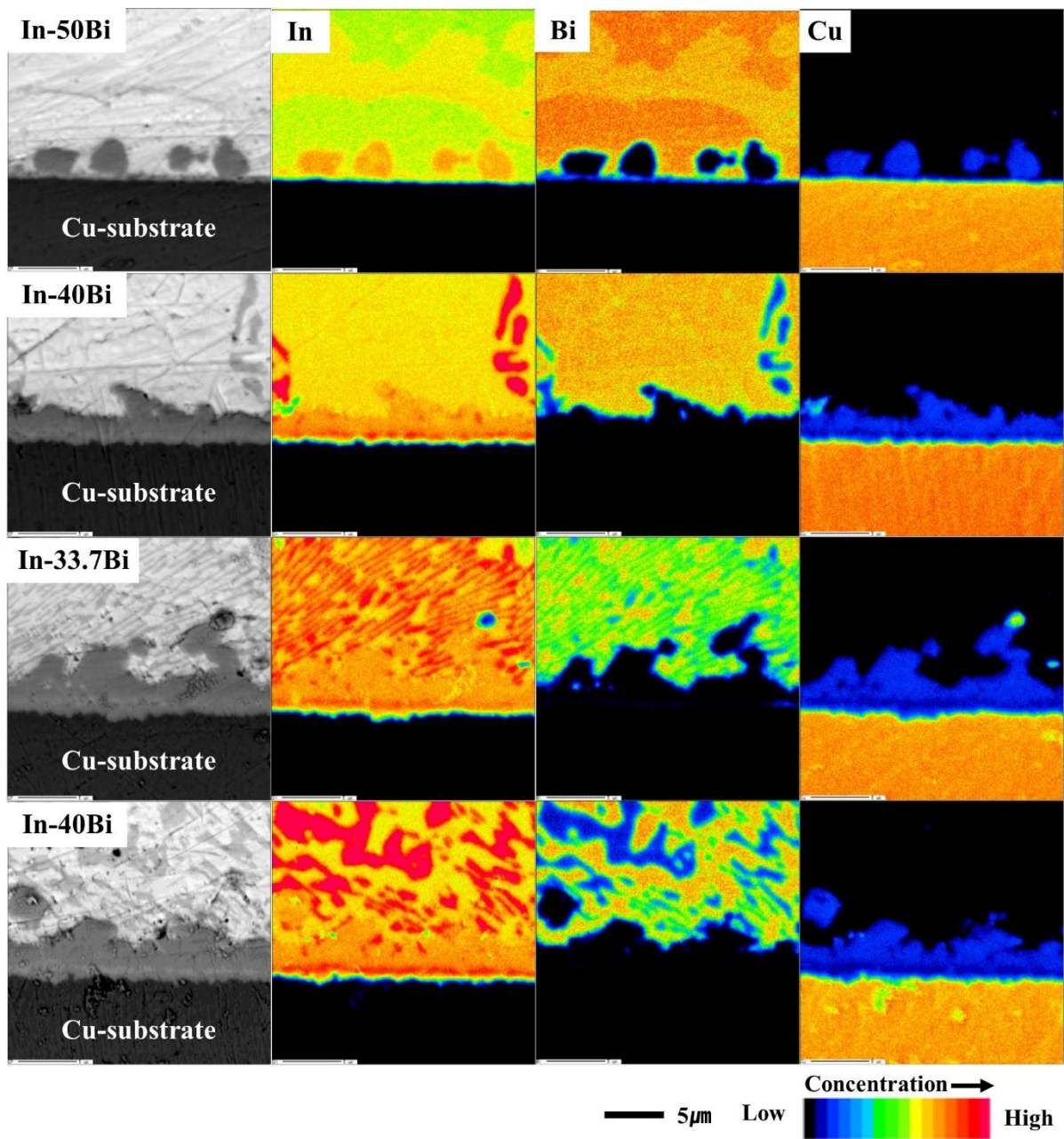


Figure 5.6 (continued)

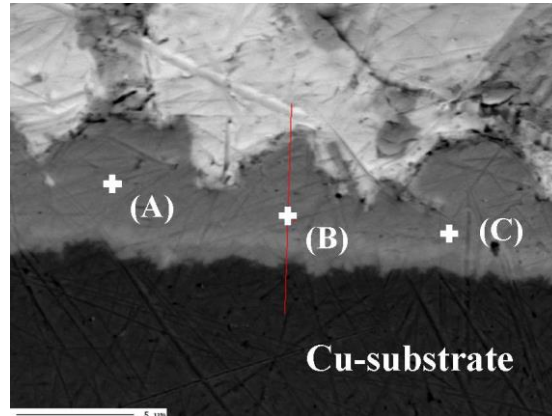


Figure 5.7 Cross-sectional EPMA image of the interface after thermal aging for 504 h at 60 °C.

Table 5.2 Point analysis of IMCs

Point	Nominal composition (mass %)		
	In	Bi	Cu
A	75.14	0.56	24.3
B	83.04	0.26	16.7
C	80.56	0.47	18.97

increased, the IMC thickness increased as the aging time was increased. The aging of joint specimens at 40 °C also resulted in the same trend. Considering all the thermally aged samples, the IMCs at the interface between the alloys and the substrate after thermal aging became thicker as the amount of indium was increased.

The growth rate of IMCs at the interface depends on the formation rate of IMCs during reflow and the diffusion rate of alloy and substrate during aging time. The relationship between the IMC thickness and aging time is as below [7].

$$d - d_0 = (Dt)^{(n)} \quad (1)$$

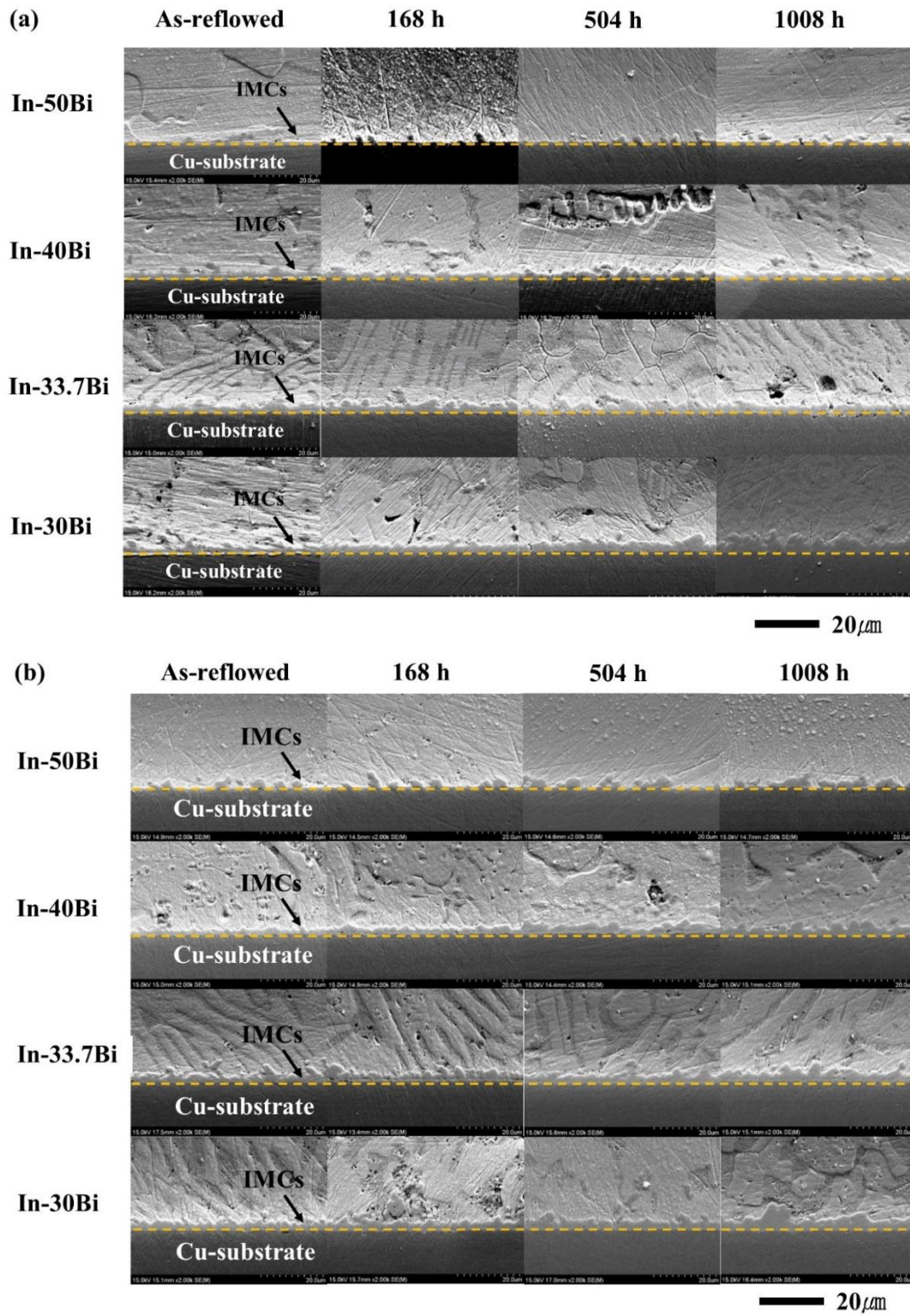


Figure 5.8 Cross-sectional images of the interfacial IMC layers of the as-reflowed and thermally aged In–Bi alloy joints after aging for 168, 504 and 1008 h (a) at 40 °C and (b) 60 °C.

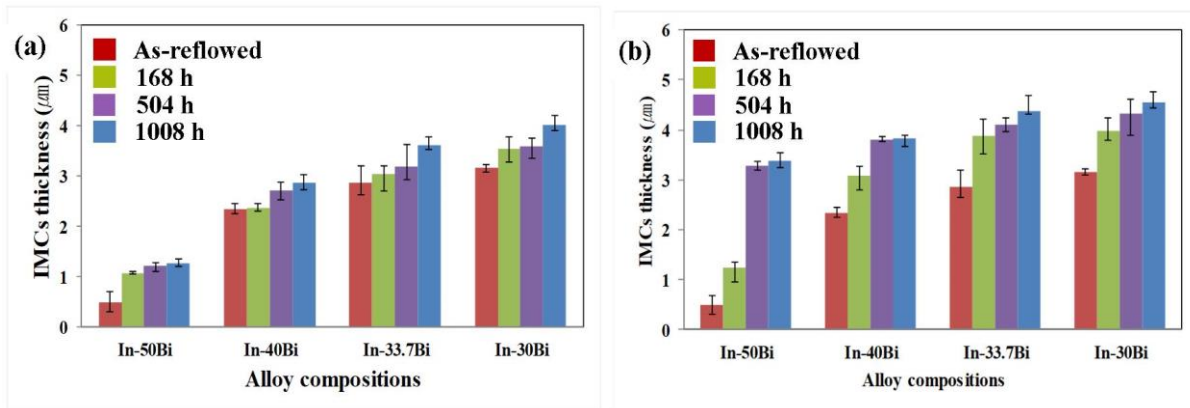


Figure 5.9 Result of IMCs thickness after thermal aging (a) at 40 °C and (b) at 60 °C.

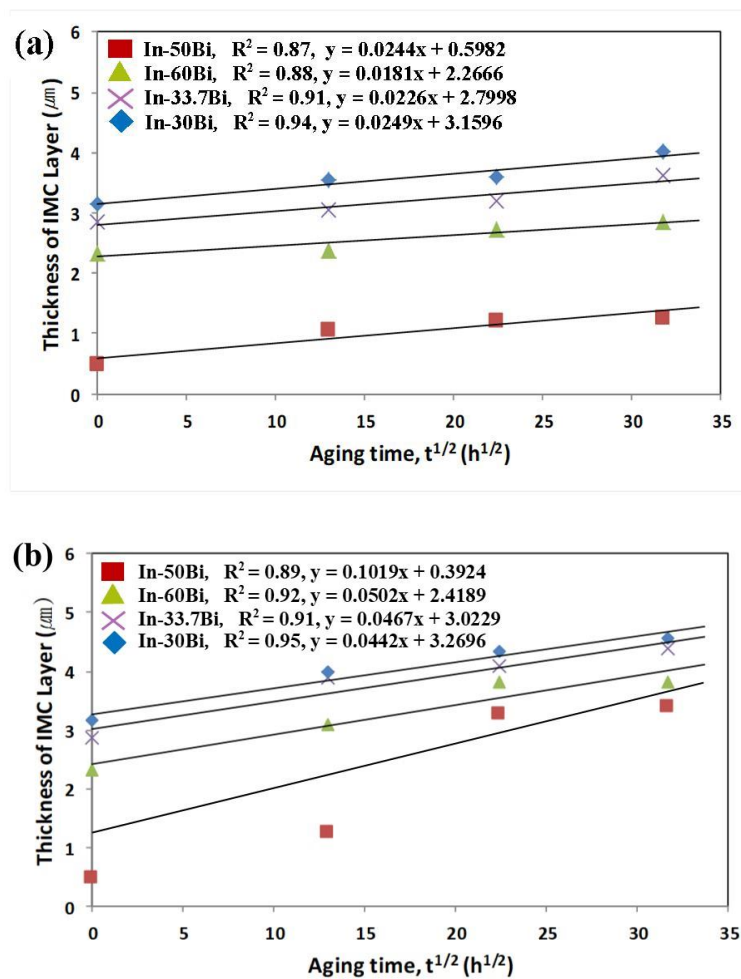


Figure 5.10 Relationship between IMC thickness and square root of aging time (a) at 40 °C and (b) at 60 °C.

Table 5.3 Calculated the layer growth coefficient of IMC layers and the linear correlation coefficient (R^2)

IMC	Temperature	Alloy compositions	Layer growth coefficient (m^2/s)	R^2
Cu_xIn_y	40 °C	In-50Bi	1.63×10^{-19}	0.87
		In-40Bi	0.77×10^{-19}	0.88
		In-33.7Bi (eutectic)	1.59×10^{-19}	0.91
		In-30Bi	1.99×10^{-19}	0.94
	60 °C	In-50Bi	2.31×10^{-18}	0.89
		In-40Bi	6.12×10^{-19}	0.92
		In-33.7Bi (eutectic)	6.37×10^{-19}	0.91
		In-30Bi	5.40×10^{-19}	0.95

where d is the thickness of the IMC layer, d_0 is the initial thickness of IMC layer in as-reflowed. D is the layer growth coefficient and t is the aging time. n is 1/2 (one-half). As shown in Table 5.3, the growth rate of IMC was faster for higher aging temperature. And the curve of the average thickness of the Cu_xIn_y IMC versus the square root of aging time at 40 °C and 60 °C aging temperature is shown in Fig. 5.10. The IMC layer thickness was found to increase linearly with the square root of aging time and the growth was faster for higher aging temperature. All of the linear correlation coefficient values (R^2) for these plots were greater than 0.85. The good linear correlation prompts that the growth of the IMC layer is controlled by diffusion over the temperature range studied [8–10].

5.3.3 Effects of aging time on shear strengths

The reliability of these joints was examined. Thus, we investigated the shear strengths of the produced joints after reflow and thermal aging. Fig. 5.11 shows the shear strength results of In–Bi joints after reflowed, and thermal aging at 40 °C and 60 °C for 168, 504 and 1008 h. The shear strength of the In–50Bi alloy, In–40Bi alloy, In–33.7Bi alloy, and In–30Bi alloy before thermal aging were 23.8 MPa, 22.1 MPa, 21.0 MPa, and 18.8 MPa, respectively. After thermal aging for 168 h at 40 °C, as shown in Figure 5.11(a), the shear strength of the In–50Bi

alloy, In-40Bi alloy, In-33.7Bi alloy, and In-30Bi alloy were 31.4 MPa, 24.8 MPa, 23.0 MPa and 19.0 MPa, respectively. After thermal aging for 504 h at 40 °C, the shear strength of the In-50Bi alloy, In-40Bi alloy, In-33.7Bi alloy, and In-30Bi alloy were 31.0 MPa, 26.5 MPa, 22.8 MPa and 21.6 MPa, respectively. After thermal aging for 1008 h at 40 °C, the shear strength of the In-50Bi alloy, In-40Bi alloy, In-33.7Bi alloy, and In-30Bi alloy were 35.0 MPa, 27.4 MPa, 25.9 MPa and 23.1 MPa, respectively. Figure 5.11(a) shows the summarized shear strength of the In-xBi alloys. After thermal aging for 168 h at 60 °C, as shown in Figure 5.10(b), the shear strength of the In-50Bi alloy, In-40Bi alloy, In-33.7Bi alloy, and In-30Bi alloy were 37.0 MPa, 32.7 MPa, 23.6 MPa and 20.9 MPa, respectively. After thermal aging for 504 h at 60 °C, the shear strength of the In-50Bi alloy, In-40Bi alloy, In-33.7Bi alloy, and In-30Bi alloy were 36.9 MPa, 30.7 MPa, 21.6 MPa and 19.7 MPa, respectively. After thermal aging for 1008 h at 60 °C, the shear strength of the In-50Bi alloy, In-40Bi alloy, In-33.7Bi alloy, and In-30Bi alloy were 35.4 MPa, 27.5 MPa, 21.0 MPa and 19.3 MPa, respectively. Figure 5.11(b) shows the summarized shear strength of the In-xBi alloys. Evidently, all alloys exhibited increased joint strength as the aging time was increased. Furthermore, the In-50Bi joints exhibited the greatest shear strength among all the alloys after both reflow and thermal aging. Fig. 5.11(a) also shows that the addition of indium decreased the shear strength of the In-Bi alloy joints after aging at 40 °C. The specimens aged at 60 °C also exhibited the same trend as shown in Fig. 5.11(b). However, the shear strength of the In-Bi joints thermally aged at 60 °C

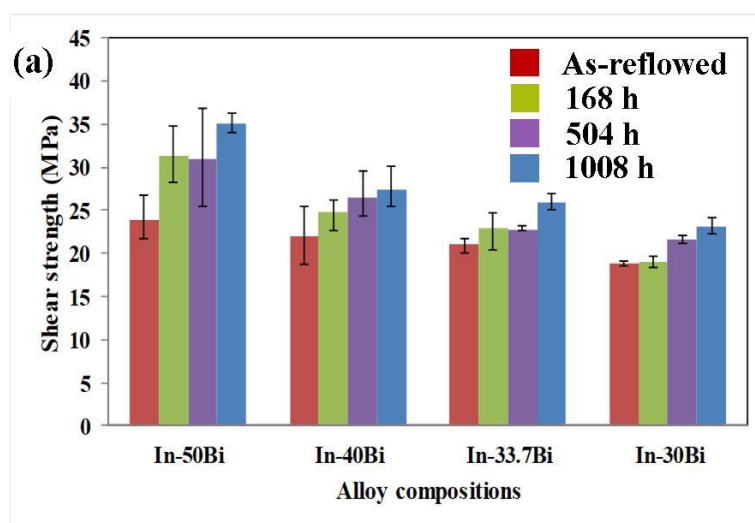


Fig. 5.11 Result of shear strength test after thermal aging (a) at 40 °C and (b) at 60 °C.

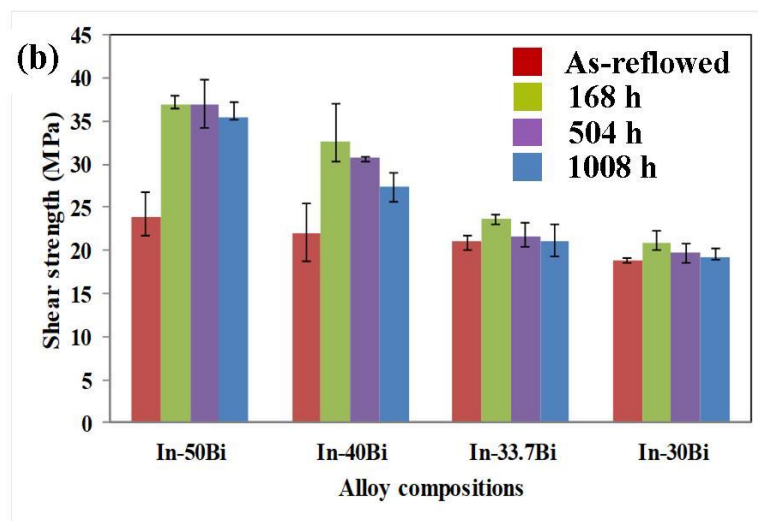


Figure 5.11 (continued)

showed different results. The alloy joints exhibited increased shear strength up to 168 h of aging time. However, beyond this, the shear strength decreased as the aging time was increased. The growth of IMCs at the interface decreased shear strength after thermal aging. Generally, excessive growth of intermetallic compounds at the interface is considered to reduce the shear strength. This can be also confirmed in the fracture surface.

5.3.4 Fracture surfaces in alloy joints after shear test

Fig. 5.12 shows the results of the EPMA elemental mapping analysis of the as-reflowed and thermally aged In–Bi alloy joints after shear tests. The fracture surfaces were pock-marked with void. The presence of larger and continuous voids at the interface between the alloy and IMCs are correlated with alloy joint strength. And observed in all specimens at all compositions and aging time, the fracture typically occurred at the bulk alloy after thermally aged at 40 °C. However, the solder joints at 60 °C for aging duration of 504 and 1008 h were exhibited the fracture surface at interface on the Cu substrate. This means that as aging continues at 60 °C, the IMCs on the Cu substrate were more brittle than the bulk IMCs. This is related to the decrease in shear strength due to thermal aging at 60 °C.

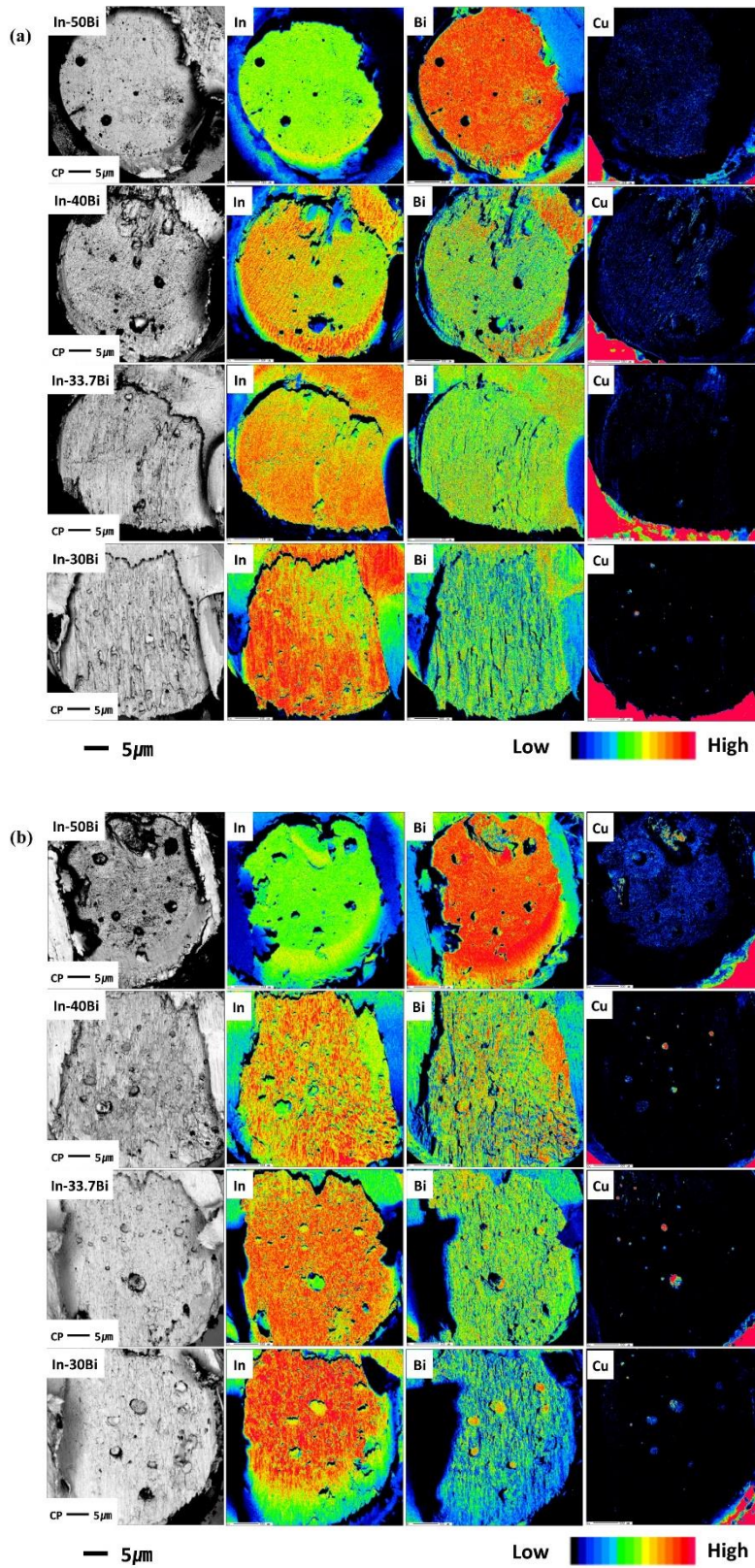


Figure 5.12 EPMA mapping results of fracture surface of (a) as-reflowed and after thermal aging for 1008 h (b) at 40 °C and (c) at 60 °C.

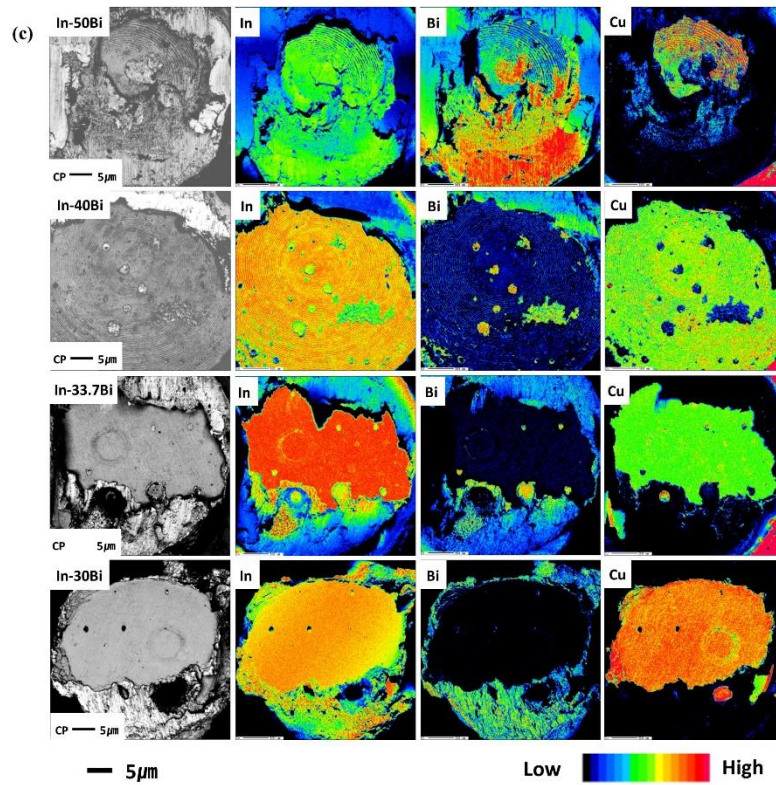


Figure 5.12 (continued)

5.4. Conclusion

In this chapter, the effect of thermal aging on the shear strength of In-Bi joints was investigated. The following summaries were obtained:

- (1) The microstructures of the investigated In-Bi alloys contained primary In-phase, Bi_3In_5 , and BiIn_2 phases.
- (2) As the amount of indium was increased, the IMC thicknesses increased with increasing aging time. The IMC formed on the Cu substrate after thermal aging was Cu_xIn_y .
- (3) The growth rate of IMC was faster for higher aging temperature. And all of the linear correlation coefficient values (R^2) were greater than 0.85.

- (4) All the joints exhibited increased shear strength as the aging time was increased. Furthermore, the addition of indium was found to decrease the shear strength of the In-Bi joints. However, the shear strength decreased only after aging at 60 °C for 504 h or more.

References

- [1] Frear, D., Dennis Grivas, and J. W. Morris, “A microstructural study of the thermal fatigue failures of 60Sn-40Pb solder joints”, *Journal of Electronic Materials*, 17.2 (1988) 171–180
- [2] Miao, Hui-Wei, and Jenq-Gong Duh, “Microstructure evolution in Sn–Bi and Sn–Bi–Cu solder joints under thermal aging”, *Materials chemistry and physics*, 71.3 (2001) 255–271
- [3] Kim, Kyung-Seob, et al., “Analysis on interfacial reactions between Sn–Zn solders and the Au/Ni electrolytic-plated Cu pad”, *Journal of alloys and compounds*, 379.1-2 (2004) 314–318
- [4] H. Okamoto, P.R. Subramanian, L. Kacprzak, “Binary Alloy Phase Diagrams”, 2nd ed., ASM International, (1990) 748–750
- [5] King-Ning Tu, “Solder Joint Technology”, Springer, New York, Vol. 117 (2007) 62–67.
- [6] K. Zeng, K.N. Tu, “Six cases of reliability study of Pb-free solder joints in electron packaging technology”, *Mater. Sci. Eng. Rep.*, R38 (2002) 55–105.
- [7] Jiawei Zhang, et al., “Impact of isothermal aging on the long-term reliability of finepitch ball grid array packages with different Sn-Ag-Cu solder joints”, *IEEE Trans. Compon. Packag. Manuf. Technol.*, 2 (8) (2012) 1317–1328.
- [8] I. Manna, S. Bader, W. Gust, B. Predel, Interdiffusion between in layer and bulk Cu or Cu-In alloy, *Phys. Status Solidi A* 119 (1) (1990) 9–13.
- [9] S.M.L. Nai, J. Wei, M. Gupta, Interfacial intermetallic growth and shear strength of lead-free composite solder joints, *J. Alloys Compd.* 473 (1–2) (2009) 100–106.
- [10] Ousama M. Abdelhadi, Leila Ladani, IMC growth of Sn-3.5 Ag/Cu system: combined chemical reaction and diffusion mechanisms, *J. Alloys Compd.* 537 (2012) 87–99.

Chapter 6

Transient liquid phase bonding of In-Bi alloy with added Cu particles

6.1 Introduction

The In–Bi alloy has been recognized as a promising substitute because its onset temperature is lower than other solder alloy and mechanical properties are comparable to the Sn–Bi and Sn–In alloys [1–3]. As mentioned, the major failure mechanisms of IC packages are delamination, whisker growth and warpage which caused by high temperature of reflow process. Especially, flexible substrate materials are prone to thermal damages and maybe deformed at this temperature. The eutectic composition of the In–Bi system is In–33.7Bi, which has an Onset temperature of 71.5 °C. The low melting point of In–33.7Bi alloy is an advantage for low-temperature soldering. However, contrary to this advantage, it means In–33.7Bi alloy has a disadvantage which can only be used for applications with working temperatures below 71.5 °C. The limited use is a mortal weak point as a bonding material for electronic packaging. To supplement for disadvantage, one method that can increase the melting point of solder during processing is transient liquid phase (TLP) bonding. TLP bonding consists of the

isothermal solidification of an initially molten joint through the disappearance of the liquid as a result from the interaction between the molten solder and the substrates and formation of solid IMC phases [4–7]. Thus, a TLP joint can be processed at a relatively low temperature, but results in the formation of a new in situ alloy with a higher re-melting point. Recently, the application of TLP processing to low-temperature soldering in the microelectronics industry has attracted more interest. The principle behind TLP processing is the solid–liquid interdiffusion (SLID) between the atoms of two materials, and has been primarily applied to the low-temperature bonding of power semiconductor dies [8]. The aim of this study was to investigate the TLP bonding process of a In–33.7Bi alloy with added Cu particles to increase the melting point of the solder joint. Thus, in this study, Cu microparticles as the high-temperature material and mixed with In-Bi eutectic powder as the low-temperature material. And the influence of processing temperature, time and thermos compression conditions on joint strength, remelting temperature has been investigated. In addition, the interfacial microstructure between the filler metal and Cu substrate and particles were investigated.

6.1.1 TLP bonding process

According to the article by Tuah Poko et al. [9], TLP bonding has four stages such as dissolution, widening, isothermal solidification and homogenization as shown in Fig. 6.1.

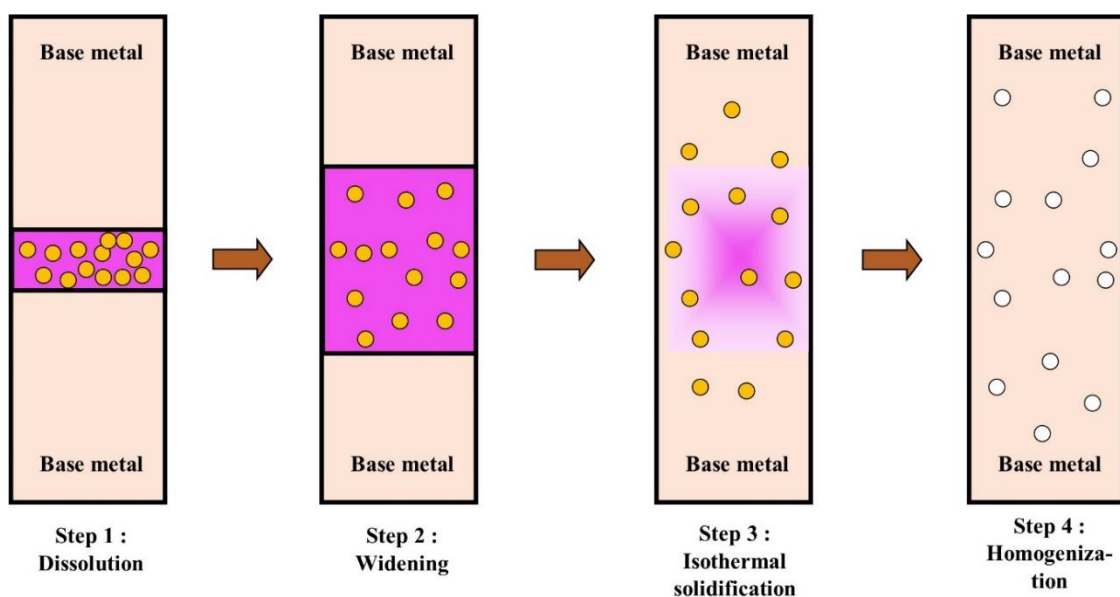


Figure 6.1 Illustration of TLP bonding process [9].

The TLP bonding process differs from diffusion bonding in which diffusion occurs when a melting point represent element from an interlayer moves into lattice and grain boundaries of the substrates at the bonding temperature [10]. Solid state diffusional processes lead to a change of composition at the bond interface and the dissimilar interlayer melts at a lower temperature than the parent materials. Thus a thin layer of liquid spreads along the interface to form a joint at a lower temperature than the melting point of either of the parent materials. This method differs from brazing in that it is "isothermally solidifying" [11]. While holding the temperature above the filler metal melting point, interdiffusion shifts the composition away from eutectic, so solidification occurs at the process temperature [12]. If sufficient interdiffusion occurs, the joint will remain solid and strong well above the original melt process temperature [13]. This is why it is termed "transient liquid phase." The liquid solidifies before cooling.

6.2 Experimental

6.2.1 TLP bonding sample preparation

In this chapter, In–33.7Bi with added Cu particles (30 mass%). The In–33.7Bi alloy powder were prepared by Nihon Genma MFG. Co., Ltd. which were made of eutectic In–Bi, Cu particles ($\text{\O} 3\sim 5 \mu\text{m}$, Mitsui Mining and Smelting Co., Ltd., code: 1400YM) and a mildly activated 12 wt.% rosin flux as shown in Fig. 6.2. Figure 6.3(a) shows a scanning electron microscopy (SEM, SU-70, Hitachi) image of the Cu particles. The diameter of the Cu particles was determined using ImageJ quantitative analysis software. The diameter was reported as an average of 150 particles, and the resulting particle size distribution is shown in Fig. 6.3(b). Then, the alloy paste was sandwiched between oxygen free Cu discs. Before making a Cu/ In–Bi–30Cu/Cu joint sample, 10-mm diameter Cu discs were cleaned using 4 vol.% HCl and

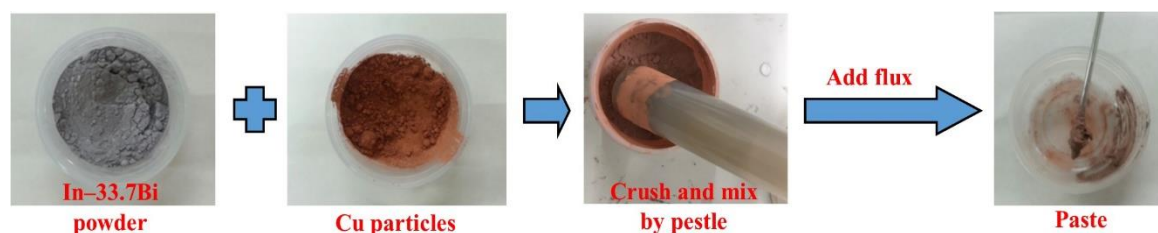


Figure 6.2 The process of make an alloy paste.

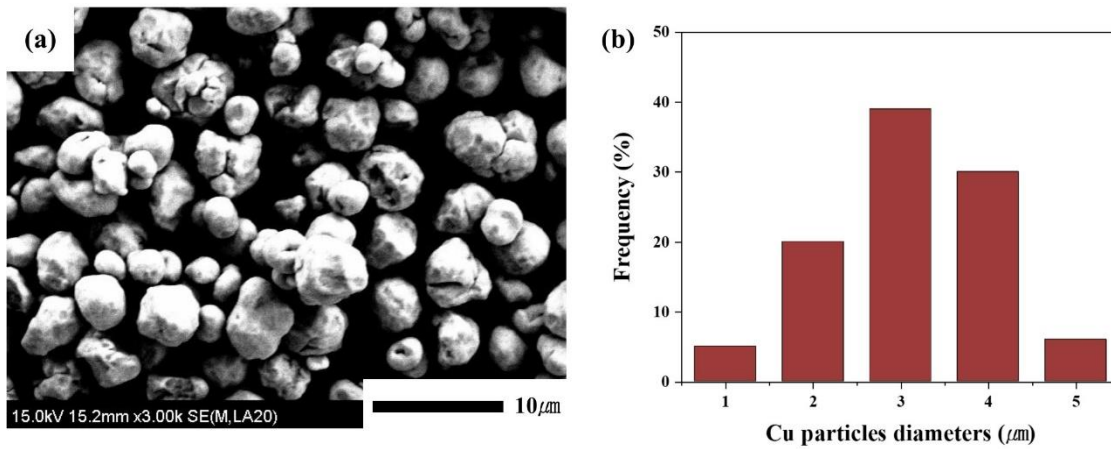


Figure 6.3 SEM image of (a) Cu particles before addition to the alloy paste and (b) the frequency of Cu particles diameters.

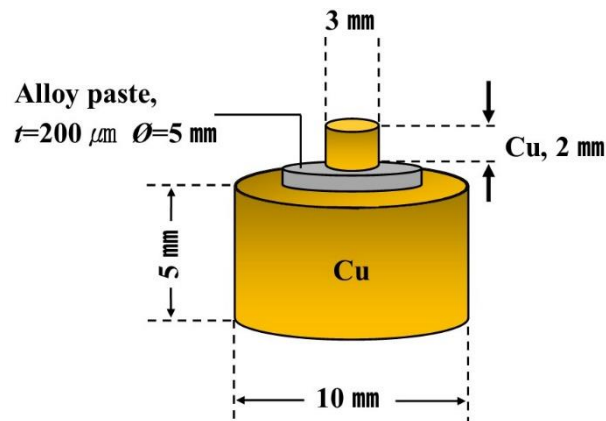


Figure 6.4 The schematic illustration of the TLP bonding sample.

ethanol. As shown in Fig. 6.4, an alloy paste was deposited onto the 10-mm diameter Cu disc by printing through a 200-μm-thick stencil. Then 3-mm diameter Cu discs, which were cleaned using the aforementioned method, were placed on top of the alloy paste to make a Cu/filler metal/Cu sandwich without applied pressure.

6.2.2 TLP bonding process.

The samples with added Cu particles were pre-heated at 50 °C for 90 s and then reflowed at 100 °C in N₂ atmosphere for 10, 50 min as shown in Fig. 6.5(a). In addition, samples were bonded using a thermos-compression bonding system with same bonding profile, respectively, for comparison. The prepared joint specimens were first pre-heated at 50 °C for 90 s then bonded at 100 °C for 10 min and 50min with a pressure of 5 MPa using a thermo-compression bonding system as shown in Fig. 6.5(b).

6.2.3 Microstructural characterization

The reflowed and thermo-compressed samples were mounted in epoxy and cross-sectioned by mechanical polishing to observe their microstructure using scanning electron microscopy (SEM, SU-70, Hitachi). Cu/ In–Bi–30Cu/Cu joint samples were cut and ground with 400#, 800#, 1200#, and 2000# SiC paper, then carefully polished using polishing pastes. The compositions of the IMC layers and bulk alloys were analyzed by elemental point analysis using an energy- dispersive x-ray spectrometer (EDS, Oxford Instruments). The elemental mapping of the microstructure was conducted by electron probe microanalyzer (EPMA, JXA-8530F, JEOL). In addition, line and point analysis were also performed with the EPMA.

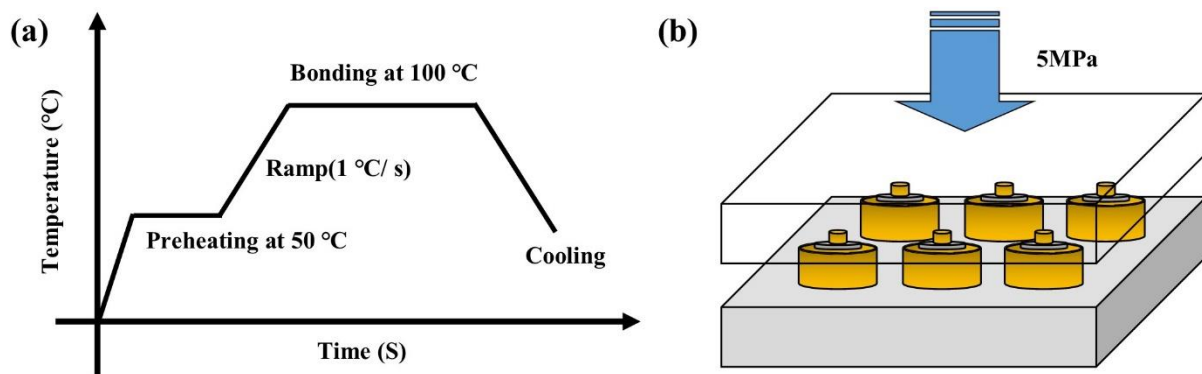


Figure 6.5 The schematic illustration of (a) heating profile and of (b) the thermos-compression bonding.

6.2.4 Elemental analysis and Differential scanning calorimetry (DSC) analysis

The phase contents of In–Bi–30Cu alloy were measured before TLP bonding by X-ray diffraction (XRD, Ultima IV, Rigaku, Tokyo, Japan) with Cu K α radiation ($\lambda = 1.54059 \text{ \AA}$) at an accelerating voltage of 40 kV. The diffraction beam was scanned in steps of 0.02° across the 2θ range of $20\text{--}80^\circ$ at $2^\circ/\text{min}$. The International Center for Diffraction Data powder diffraction file cards, including #00-001-1042 for In, #00-011-0566 for BiIn₂, #00-001-1241 for Cu, and #00-002-1041 for CuO, were used as references to identify the diffraction patterns. Quantitative phase analysis was conducted via the reference intensity ratio method using PDXL software provided by Rigaku. Phase analysis was reaffirmed by HighScore Plus software version 3.0e (PANalytical B.V, Almero, Netherlands).

The DSC was performed with a differential scanning calorimetry (DSC, DSC7020, Hitachi, Tokyo, Japan) to examine the re-melting onset temperature of the joints. The heating rate and isothermal period used were $10^\circ\text{C}/\text{min}$ and 10 min, respectively. In this study, Cu/In–Bi–30Cu/Cu alloy joints were examined by DSC after removal from the Cu substrates. The mass of the samples used for the DSC measurements ranged from 8 to 10 mg. The melting range of each valley was considered the difference between the solidus (hereinafter referred to as the melting onset) and liquidus points, which were calculated from the DSC measurements.

6.3 Results

6.3.1 Estimating the Cu content required for TLP bonding

The scale of the reaction between the In and Cu to form Cu_xIn_y was investigated as shown in Fig 6.6. This mathematical analysis only considered the reaction between the In atoms and added Cu particles; the flux of Cu atoms from the substrates was neglected. To determine the concentration of Cu required to convert the entire In phase into IMCs, three Cu particle contents were theoretically investigated: 10, 20, 30, 40, 50 and 60 mass%. By considering the atomic weights of In, Bi, and Cu which are 114.818, 208.98, and 63.546, respectively, the

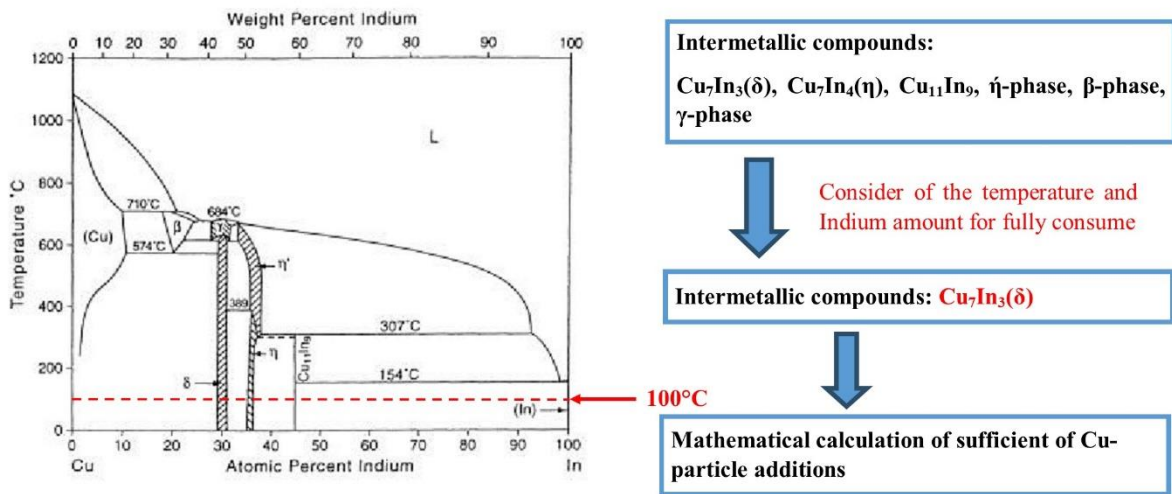


Figure 6.6 The binary phase diagram of Cu and In.

atomic percentages of In, Bi, and Cu required for the In–Bi powder + 10 mass% of Cu particles were 62.23, 17.63, and 19.14 %, respectively. By similar calculations, the atomic percentages of In, Bi, and Cu were 51.02, 14.23, and 34.75 % for the In–Bi powder + 20 mass% of Cu particles and 40.88, 11.4, and 47.72 % for the In–Bi powder + 30 mass% of Cu particles and 32.31, 9.01, and 58.68 % for the In–Bi powder + 40 mass% of Cu particles and 24.98, 6.97, and 68.05 % for the In–Bi powder + 50 mass% of Cu particles and 18.64, 5.2, and 76.16 % for the In–Bi powder + 60 mass% of Cu particles, respectively. These values are summarized in Table 6.1, where they are used to calculate the percentage of unreacted In–Bi or unreacted Cu expected in the system assuming formation of Cu_7In_3 IMCs only. For the In–Bi + 50 mass% of Cu alloy, all of the In phase would react with the Cu to form Cu_7In_3 and leave 9.73 % of the Cu phase in the solder. Finally, for the In–Bi + 60 mass% of Cu alloy, all of the In phase would react with the Cu and leave 32.69 % of unreacted Cu in the solder. Thus, only the In–Bi solders with 50 or 60 mass% of Cu have a sufficient concentration of Cu to react with and consume the entire In phase inside the solder. However, in case of the In–Bi solder with 40, 50, 60 mass% of Cu particles had problems which were not mixing properly due to too much Cu particles. Therefore, the In–Bi solder with 30 mass% of Cu particles (hereinafter referred to as In–Bi–30Cu solder) was used in this study.

Table 6.1 Mathematical calculation of sufficient of Cu particle

Indium - Bismuth :	66.3 wt. % In - 33.7 wt. % Bi						
Indium : Bismuth	1 : 1.97				IMCs : Cu-In₃		
Cu-particle contents (mass %.)	Composition	wt. %	at. %		Copper	Indium	Remain Cu
10 %	Indium	59.7	63.23		2.73	21.08	-
	Bismuth	30.3	17.63				
	Copper	10	19.14				
	Total	100	100				
20 %	Indium	53.06	51.02		4.96	17.01	-
	Bismuth	26.94	14.23				
	Copper	20	34.75				
	Total	100	100				
30 %	Indium	46.43	40.88		6.82	13.63	-
	Bismuth	23.57	11.4				
	Copper	30	47.72				
	Total	100	100				
40 %	Indium	39.8	32.31		8.38	10.77	-
	Bismuth	20.2	9.01				
	Copper	40	58.68				
	Total	100	100				
50 %	Indium	33.16	24.98		9.72	8.33	remain 9.73 at.% Cu
	Bismuth	16.84	6.97				
	Copper	50	68.05				
	Total	100	100				
60%	Indium	26.53	18.64		10.88	6.21	remain 32.69 at.% Cu
	Bismuth	13.47	5.2				
	Copper	60	76.16				
	Total	100	100				

6.3.2 Microstructure of the alloy joints

Figure 6.7 shows a comparison of the microstructure of the conventional In–Bi and In–Bi–30Cu alloys after being reflowed at 100 °C for 10 min. The bright and dark gray regions in the images represent the BiIn₂ and In phases, respectively. The dark spots in Fig. 6.7(b) are Cu particles that have partly reacted with the In phase. In addition, there is a very thin, sunflower-shaped Cu–In IMC layer around each Cu particle. Even though the addition of Cu particles in this study is because of their advantage in reducing the reflow period in comparison with the Cu/In–Bi/Cu alloy joint, to investigate the required reflow period for the complete isothermal solidification, investigation on the longer period of reflow is needed. Therefore, samples were subjected to 10 and 50 min reflow periods at 100 °C. Figure 6.8 shows the different microstructures of the In–Bi–30Cu alloy after being reflowed at 100 °C for 10 and 50 min. As can be seen, there are some differences such as the lamellar structures were disappeared and only BiIn₂ and Cu–In IMCs have existed. And as the heating time increased, the thickness of

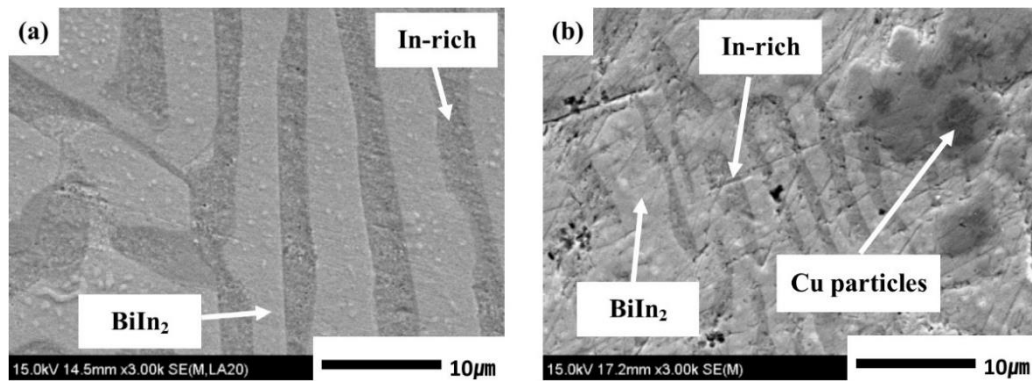


Figure 6.7 The microstructure of (a) In–Bi and (b) In–Bi–30Cu after reflow at 100 °C for 1 min.

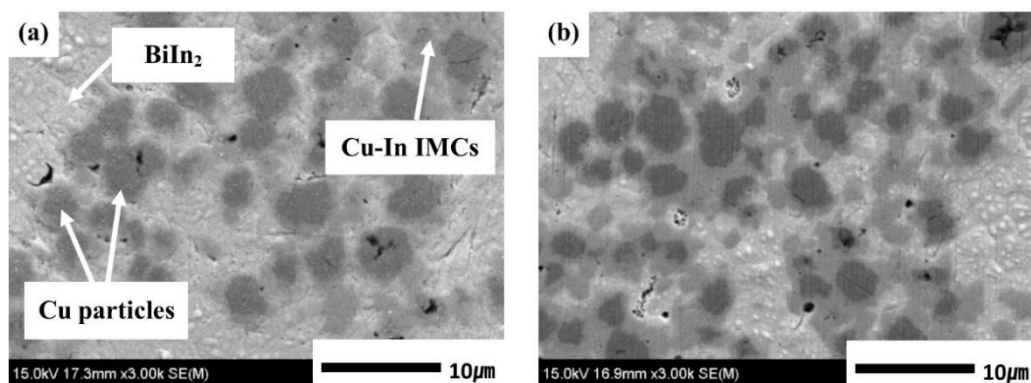


Figure 6.8 The microstructure of In–Bi–30Cu after reflow at 100 °C for (a) 10 min and (b) 50 min.

the IMC layers around the Cu particles was increased as shown in Figs. 6.8 and 6.9. Fig 6.8 and Fig 6.9 show a large difference compared to the previous images, revealing that 50 min of reflow is highly effective for reacting Cu with In. And even though Fig. 6.8(b) and Fig. 6.9(b) shows that the reactions between Cu and In increase significantly, the BiIn₂ phase is still clearly visible.

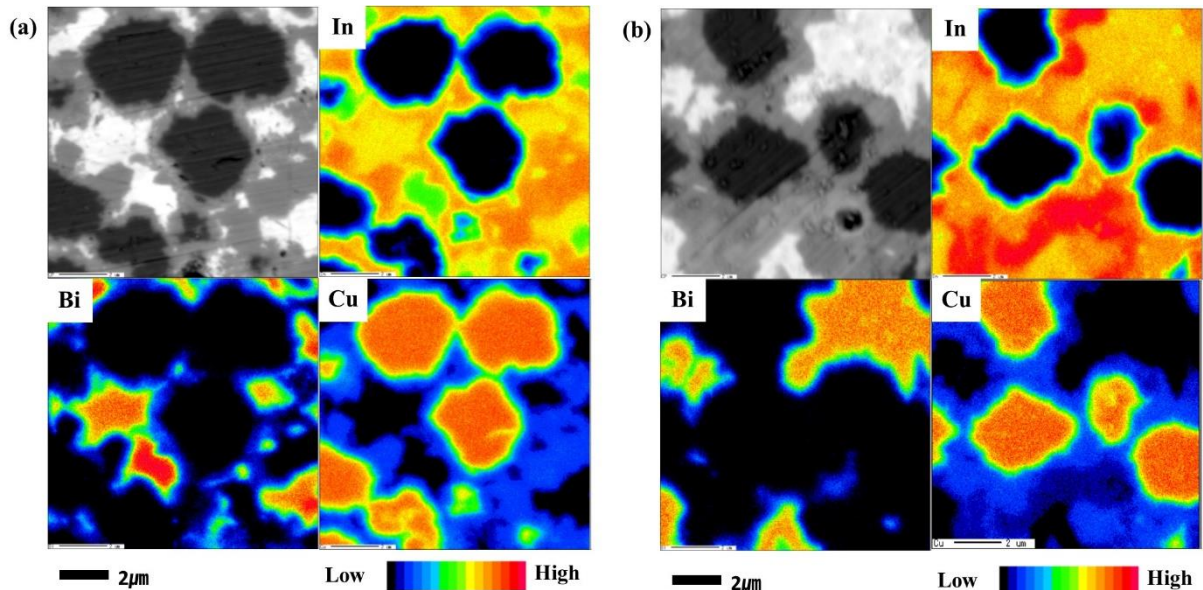


Figure 6.9 The EPMA analysis of In-Bi-30Cu for (a) 10 min and (b) 50 min.

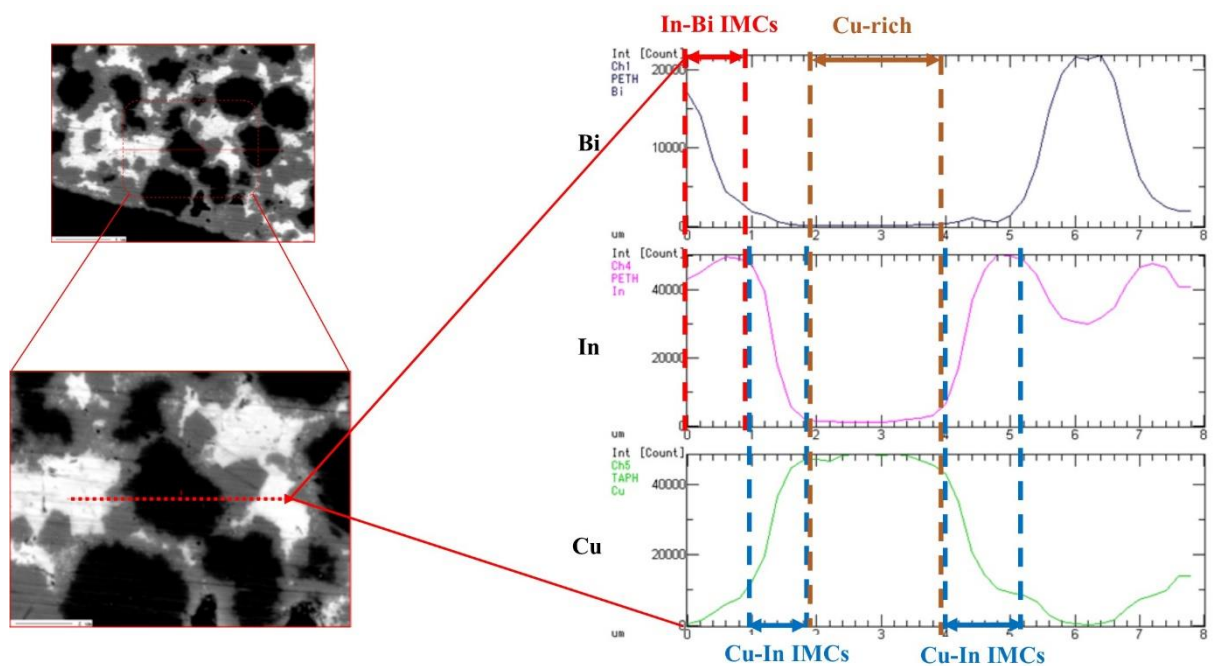


Figure 6.10 The line analysis of In-Bi-30Cu after reflow at 100 °C.

Figure 6.9 shows the EPMA elemental mapping results of the In–Bi–30Cu solder after being reflowed at 100 °C for 10min and 50 min. As can be seen, there is one Cu–In IMCs which is a thin layer around the Cu particles. Fig. 6.10 shows the line analysis of the Cu–In IMCs was formed around the Cu particles. Considering these results, the results show Cu particles reacted with the In phase to make the Cu–In IMCs.

6.3.3 Thermal analysis of the compositional shift by DSC

Figure 6.11 shows the DSC curves of the In–Bi–30Cu alloy before and after the reflow of both the bulk alloy and the alloy sandwiched between Cu substrates. In Fig. 6.11(a), a melting event of the alloy paste occurs at approximately 71.9 °C, which represents the melting

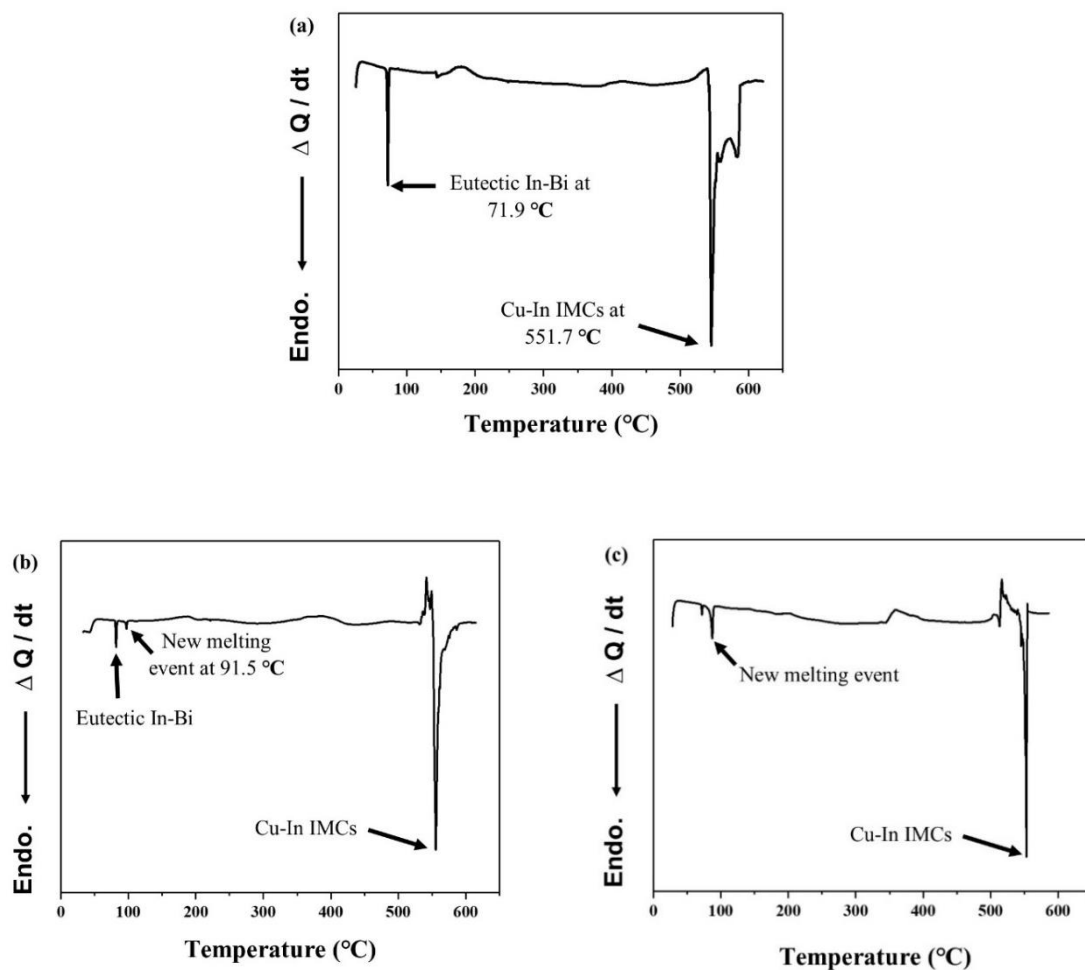


Figure 6.11 The DSC results of In–Bi–30Cu (a) before reflow (paste), (b) after reflow at 100 °C for 10 min, and (c) after reflow at 100 °C for 500 min.

of the eutectic In–33.7Bi phase. In addition, one valley is present at approximately 551.7 °C, which represent the melting of the Cu_xIn_y IMCs. Even though the alloy paste does not contain these Cu–In IMCs, once the temperature reaches a certain level during the DSC test, it allows Cu and In to react and form the Cu–In IMCs. The DSC curves in Fig. 6.11(b), (c) have a new valley indicating a melting event at approximately 91.5 °C. Figure 6.11(b) shows that after the alloy is reflowed at 100 °C for 10 min, peaks representing eutectic In–Bi and new melting event co-exist, while Fig. 6.11(c) shows that almost all the In phase has been consumed.

6.3.4 Shear strength of the alloy joints

In this chapter, finally, investigated the shear strengths of the produced joints after TLP bonding. The shear strengths of In–Bi–30Cu alloy joints after reflowed and thermo-compression bonding are shown in Fig. 6.12. Evidently, both conditions exhibited increased joint strength as the bonding time was increased. however, in case of reflowed for 10min, shear strength was approximately 9.3 MPa which exhibited the lowest shear strength among all the conditions of both reflow and thermo-compression bonding. And in case of thermo-compressed for 50min, shear strength was approximately 20.1 MPa which exhibited the highest shear strength among all the conditions of both reflow and thermo-compression bonding. In case of

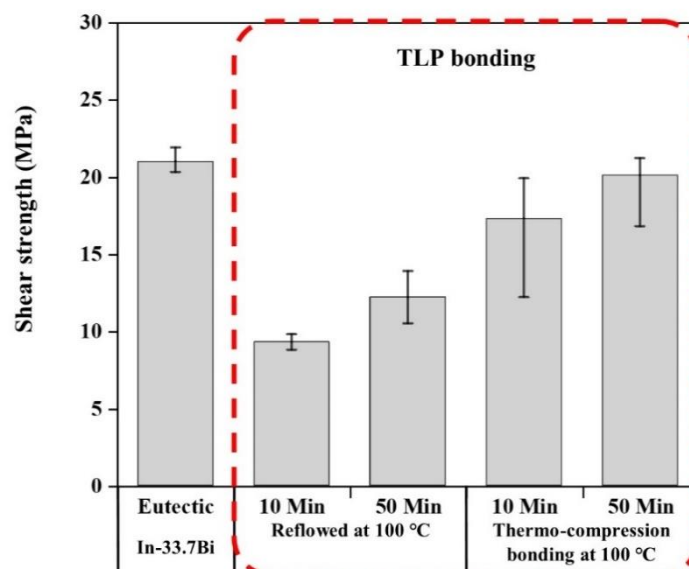


Figure 6.12 The shear strength results of In–Bi–30Cu alloy.

reflowed, the bonding joints contained large voids resulting in a considerable degradation in shear strength as shown in Fig. 6.13. however, in case of thermo-compressed, to reduce the extent of void formation and consequently improve the shear strength of the particulate-reinforced alloy joints as shown in Fig. 6.14.

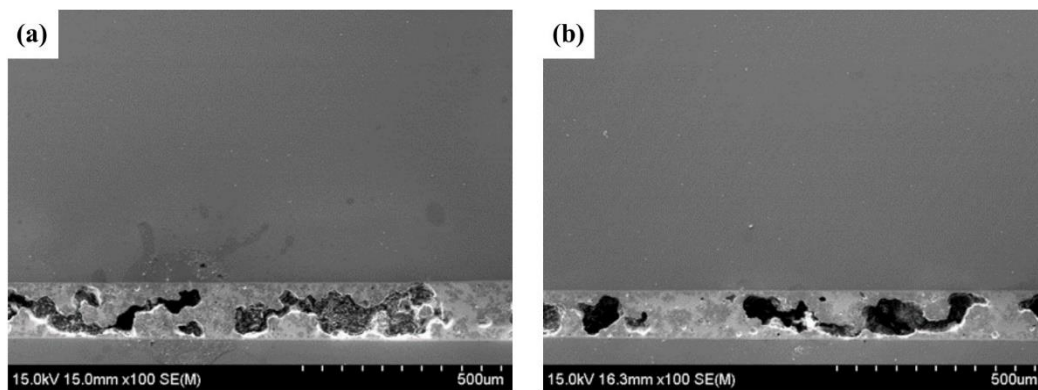


Figure 6.13 Cross-sectional image of In-Bi-30Cu alloy after reflowed at 100 °C for (a) 10 min and (b) 50 min.

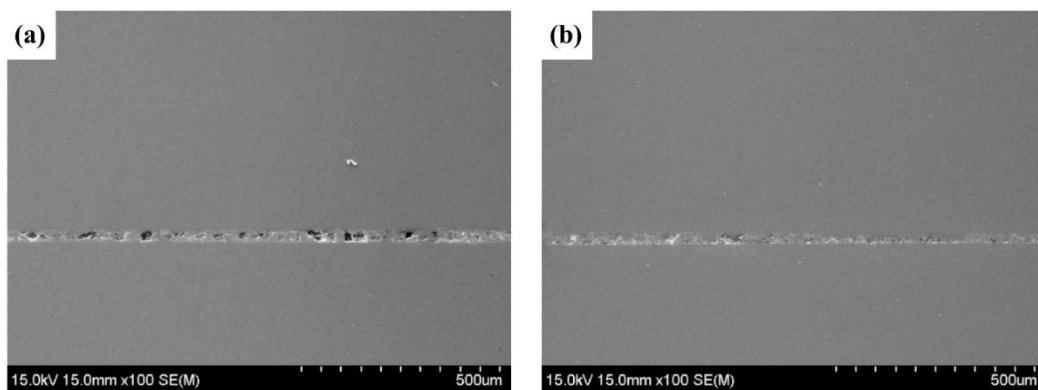


Figure 6.14 Cross-sectional image of In-Bi-30Cu alloy after thermos-compressed at 100 °C for (a) 10 min and (b) 50 min.

6.4 Conclusion

The microstructures and shear strength of the In–33.7Bi eutectic alloys with 30 mass% of added Cu particles were investigated. The results obtained in this study are summarized below:

- [1] By adding 30 mass% of Cu particles and being reflowed at 100 °C for 10 min and 50 min, the In phase was successfully consumed by the Cu, leaving Cu–In IMCs and a BiIn₂ phase in the alloy joint.
- [2] The new melting event that appeared in the DSC curves at 91.5 °C and 551.7 °C are believed to be attributed to the local compositions of Cu–In IMCs and BiIn₂ in the ternary In–Bi–Cu system. Therefore, it could be concluded that the melting point of the In–Bi solder was increased by approximately 550 °C.
- [3] To achieve the complete conversion of the In-rich phase to Cu–In IMC phases with lower heat inputs, decreasing the size of the Cu particles is recommended. And the Cu particles of nano-size are better than micro-size when mixing for homogenization in preparation of the alloy paste. Also, surface modification (e.g., protective coatings) of the Cu particles will be required to prevent oxidation.

References

- [1] Mei, Zequn, and J. W. Morris, “Characterization of eutectic Sn-Bi solder joints” *Journal of Electronic Materials*, 21.6 (1992) 599–607
- [2] Morris, J. W., JL Freer Goldstein, and Z. Mei, “Microstructure and mechanical properties of Sn-In and Sn-Bi solders”, *JOM* 45.7 (1993) 25–27
- [3] Jin, Sanghun, et al., “Microstructure and mechanical properties of indium–bismuth alloys for low melting-temperature solder”, *Journal of Materials Science: Materials in Electronics*, 29.19 (2018) 16460–16468
- [4] Mokhtari, Omid, and Hiroshi Nishikawa, “Transient liquid phase bonding of Sn–Bi solder with added Cu particles”, *Journal of Materials Science: Materials in Electronics*, 27.5 (2016) 4232–4244
- [5] MacDonald, W. D., and T. W. Eagar, “Transient liquid phase bonding” *Annual review of materials science*, 22.1 (1992) 23–46
- [6] Cook, Grant O., and Carl D. Sorensen, “Overview of transient liquid phase and partial transient liquid phase bonding”, *Journal of materials science*, 46.16 (2011) 5305–5323
- [7] Park, M. S., S. L. Gibbons, and R. Arroyave, “Phase-field simulations of intermetallic compound growth in Cu/Sn/Cu sandwich structure under transient liquid phase bonding conditions”, *Acta Materialia*, 60.18 (2012) 6278–6287
- [8] Li, J. F., P. A. Agyakwa, and C. M. Johnson, “Kinetics of Ag_3Sn growth in Ag–Sn–Ag system during transient liquid phase soldering process”, *Acta Materialia*, 58.9 (2010) 3429–3443
- [9] Di Luozzo, Nicolás, “Transient liquid phase diffusion welding of metallic parts”, *Diss. Université de Grenoble*, (2014) 12–15
- [10] D’hondt, T., and S. F. Corbin, “Thermal analysis of the compositional shift in a transient liquid phase during sintering of a ternary Cu-Sn-Bi powder mixture”, *Metallurgical and Materials Transactions A*, 37.1 (2006) 217
- [11] Guo, F., et al., “Microstructural characterisation of reflowed and isothermally-aged Cu and Ag particulate reinforced Sn-3.5 Ag composite solders”, *Soldering & surface*

mount technology, 13.1 (2001) 7–18

[12] Lee, J. G., et al., “Intermetallic morphology around Ni particles in Sn-3.5 Ag solder”, *Soldering & surface mount technology*, 14.2 (2002) 11–17

[13] Lee, Jong-Bum, How-Yuan Hwang, and Min-Woo Rhee, “Reliability investigation of Cu/In TLP bonding”, *Journal of Electronic Materials*, 44.1 (2015) 435–441

Chapter 7

Summary

7.1 Summary

In this dissertation, the development of In–Bi alloys with low-melting temperature for microelectronics interconnections was presented. This thesis has focused on the studies of: (i) microstructure and mechanical properties of In–Bi alloys; (ii) effect of In content on the microstructure and mechanical properties of In–Bi alloys during thermal aging; (iii) shear properties of In–Bi alloy joints with Cu substrates during thermal aging; (iv) Transient liquid phase bonding of In–Bi alloy with added Cu particles. The main findings and conclusions include:

In *Chapter 1*, the immersing issues on the increase of demand for flexible electric device, low temperature solders and interconnection technologies in electric packaging were summarized. The resent research trends next-generation electronics devices by flexible substrate and research objective of this research were also presented.

In *Chapter 2*, In–50 mass% Bi, In–40 mass% Bi, In–33.7 mass% Bi, and In–30 mass% Bi having a melting temperature of approximately 80 °C on the In–Bi binary phase diagram were selected. And their basic material properties such as melting temperature, microstructure and mechanical properties after tensile testing were evaluated to understand the characteristics of In–Bi alloys. The microstructures of the investigated In–Bi alloys contained primary In-phase, Bi₃In₅, and BiIn₂ Phases. Furthermore, the endothermic peaks were found between 72.7 and 91.2 °C on each differential scanning calorimetry (DSC) curve. While the tensile strengths of the In–Bi alloys declined with increasing indium content the elongation was dramatically increased at room temperature. In addition, as the indium content increased, the cross-sectional area of the tensile sample decreased, which shows high-ductility characteristics.

In *Chapter 3*, the effects of In content on the melting properties and microstructure of In–Bi alloys under thermal aging were investigated. An aging temperature of 40 °C and 60 °C was selected as it represents the typical user and harsh environmental conditions for flexible electronic devices. The increase of indium amount in In–Bi alloys depressed their onset temperature. And the results of DSC did not change significantly even after thermal aging at 40 and 60 °C. The microstructure of the In–Bi alloys containing the primary In-phase, Bi₃In₅, and BiIn₂ phases was investigated. The In-rich phase increased with In content. However, the microstructure did not change significantly during thermal aging. In the case of In–33.7Bi, the eutectic spacing gradually increased during thermal aging, becoming approximately 1.25 times larger than that of the as-cast alloy.

In *Chapter 4*, the thermal aging test was conducted on In–Bi alloy specimens to evaluate the change of their mechanical properties and fracture characteristics during aging. Ultimately, The UTS of In–Bi alloys decreased with increasing indium content and thermal aging time. However, the changes in UTS with aging time were not significant, except for in the case of In-50Bi. The elongation of In–Bi alloys was drastically increased with increasing In content in both the as-cast and thermally aged specimens. However, the elongation behavior of these alloys did not change significantly after thermal aging. The thermally aged In–Bi alloys showed outstanding low-temperature deformation properties due to their stable thermal behaviors. In addition, the fracture surfaces exhibited ductile fractures in the neck shapes. An increase in In

content decreased the cross-sectional area of the tensile sample, indicating high ductility. And the elongation and the area reduction remained very high at the aging temperature.

In *Chapter 5*, the purpose of this chapter is to evaluate the shear strengths of the Cu/In–Bi alloy/Cu joints and analyze the interfacial reactions as a function of isothermal aging to evaluate their long-term reliability. As the amount of indium was increased, the IMC thicknesses increased with increasing aging time. The IMC formed on the Cu substrate after thermal aging was Cu_xIn_y . The growth rate of IMC was faster for higher aging temperature. And all of the linear correlation coefficient values (R^2) were greater than 0.85. All the joints exhibited increased shear strength as the aging time was increased. Furthermore, the addition of indium was found to decrease the shear strength of the In–Bi joints. However, the shear strength decreased only after aging at 60 °C for 504 h or more.

In *Chapter 6*, Cu microparticles as the high-temperature material and mixed with In–Bi eutectic powder as the low-temperature material. And the influence of reflow conditions and thermo-compression conditions on joint strength, remelting temperature has been investigated. In addition, the interfacial microstructure between the filler metal and Cu substrate and particles were investigated. By adding 30 mass% of Cu particles and being reflowed at 100 °C for 10 min and 50 min, the In phase was successfully consumed by the Cu, leaving Cu–In IMCs and a BiIn_2 phase in the alloy joint. The new melting event that appeared in the DSC curves at 91.5 °C and 551.7 °C are believed to be attributed to the local compositions of Cu–In IMCs and BiIn_2 in the ternary In–Bi–Cu system. Therefore, it could be concluded that the melting point of the In–Bi solder was increased by approximately 550 °C. To achieve the complete conversion of the In-rich phase to Cu–In IMC phases with lower heat inputs, decreasing the size of the Cu particles is recommended. However, surface modification (e.g., protective coatings) of the Cu particles will be required to prevent oxidation.

Consequently, the development of In–Bi alloys with low-melting temperature for microelectronics interconnections was successfully demonstrated in this research. Based on

these results, In–xBi alloys with low melting temperatures are promising candidates for flexible electronics applications as well as for devices with PP- and PMMA-based substrates.

7.2 Environmental assessment on In–Bi alloys

Low-melting temperature alloys for flexible electronic devices comprise an area that has grown steadily in importance in the past decade and will continue to gain relevance in the foreseeable future. As mentioned above, the In–Bi alloys with low-melting temperature is proven a promising low-cost lead-free solder alloys for flexible electronic device packaging. In addition to the performance of the bonded joint, environmental aspect also was evaluated for the practical use.

7.2.1 Materials and bonding process

As I mentioned, when the contaminated groundwater by lead is absorbed into the human body, it is pointed out as an environmental pollutant because it has detrimental effects on the human body such as lowering of intelligence and deterioration of vital function. Therefore, it can be prevented by using Pb-free solder such as In–Bi based alloys.

The environmental assessment of various bonding process was also conducted, in term of the energy consumption and possible pollution release of each process. Generally, the soldering process using high-temperature lead-free solders is negative effect on saving cost because of electric energy is increased to maintain a high-temperature process. However, low-temperature In–Bi alloy can decrease the process temperature and cost as shown in Fig. 7.1. In addition, the Cu–In TLP bonding can be identified as low-temperature bonding process for high-temperature, it could be saved the process temperature. Moreover, low-temperature process reduces the harmful gas such as CO₂ as shown in Fig. 7.1. It will protect the earth from environmental destruction such as global warming.

7.2.2 Recycling from e-waste

Electronic Waste (e-waste) contains many valuable resources together with plenty of

Environmental assessment

Prevention of Global warming & Cost Reduction

The electricity consumption of reflow process (Sn-Bi solder at 170 °C) [1]:

53 (kW)



The electricity consumption of reflow (In-Bi alloy at 100 °C):

32 (kW) (34% reduction)

The average reduction of electricity consumption by the decrease of reflow temperature [2]:
 $\{53 - 32 \text{ (kW)}\} \times \{\text{average operation hours } 18 \text{ (h)}\} \times \{\text{average operation days } 300 \text{ (d)}\} = 113,400 \text{ (kWh)}$

The average reduction of CO₂ emission by the decrease of reflow temperature [2]:
 $113,400 \text{ (kWh)} \times \{\text{CO}_2 \text{ emission coefficient } 0.555 \text{ (kg-CO}_2\text{/kWh)}\} = 62,937 \text{ (kg-CO}_2\text{)}$

Annual saving by decrease reflow temperature [2]:
 $113,400 \text{ (kWh)} \times 20 \text{ (yen/kWh)} = 1,258,740 \text{ (yen)}$

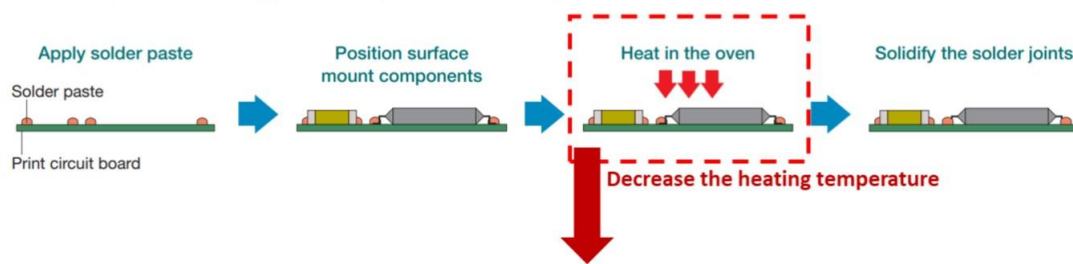


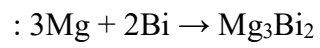
Figure 7.1 Illustration of environmental assessment of In-Bi alloys.

hazardous materials, which are considered both an attractive secondary resource and an environmental contaminant. Especially, solder alloy scrap is generated during the manufacturing process and is generated by discarded electronic products. And indium is a material that expensive and must be recycled in terms of resource circulation. Recycling waste In-Bi alloys to conserve resources and protect environment. The method that recycles indium is as below:

i) Separation of alloy element [3]

- Removal bismuth element from the In-Bi alloy scrap: Bi removal by Mg addition

- Add Mg element to the In-Bi molten alloy and refined by the reaction of Mg and Bi



ii) Dissolve the PCB in acid solution

- PCB is immersed in the acid, only indium is dissolved and purified by an electrolytic refining method.

7.3 Future work

The work in this thesis can be further enhanced and extended by further investigations recommended as follows:

1. TLP bonding, Cu_2In , at the Cu–In IMCs formed bonding process was only identified by SEM/EDS. Advanced microscopy technology (e.g. transmission electron microscopy – TEM) could be employed to elaborate the mechanism of its formation (e.g. lattice structure)
2. Experiments can be designed to obtain deformation information during the micro-mechanical testing of micro-specimens, at the same time a study on mechanisms of such deformation at micro or even nano-scale under various temperature using nanoindentation may be of interest, which can also be correlated with the effect of microstructure (e.g. IMC morphology and grain size) inside the joints on its mechanical properties.
3. It will be even more interesting to be executed in-situ, allowing low-temperature cycling to be carried out followed by TEM analysis at micro and nano-scale, as such one can verify the effect of such cycling on the evolution of IMCs during the following aging.
4. Thermo-mechanical analyses indicate the interfaces between the chip and In-Bi alloy joint are the main positions for stress concentration and deformation during low-temperature excursion. Hence, further analysis could be carried out by introducing the bond pad (UBM) and the IMC layer into the FE model, which could offer more detailed behavior (e.g. damage / failure) at the interface under various low-temperature excursions.
5. Experiments with actual PP- and PMMA flexible substrate to evaluate solder ability and reliability.

References

- [1] <https://patents.google.com/patent/WO2012102578A2/ko>
- [2] https://www.tamura-ss.co.jp/en/csr/report/pdf/env_2006.pdf
- [3] Solder 합금 Scrap 재활용 공정기술 지원, 한국생산기술연구원, 지식경제부, (2008) 30–32 (in Korean)

Research achievements

I Paper related doctoral thesis

1. **Microstructure and mechanical properties of indium–bismuth alloys for low melting-temperature solder. (published)**

Journal of Materials Science: Materials in Electronics, 29,19 (2018), 16460-16468.

Sanghun Jin, Min-Su Kim, Shutetsu Kanayama, Hiroshi Nishikawa

2. **Shear properties of In-Bi alloy joints with Cu substrates during thermal aging. (published)**

Microelectronics Reliability, 88, (2018), 795-800.

Sanghun Jin, Min-Su Kim, Shutetsu Kanayama, Hiroshi Nishikawa

3. **Effects of In Content on the Microstructure and Mechanical Properties of In–Bi Alloys During Isothermal Aging. (published)**

Metals, 9, 5 (2019), 548.

Sanghun Jin, Omid Mokhtari, Shutetsu Kanayama, Hiroshi Nishikawa

II Conferences

Oral:

1. 19th Electronics Packaging Technology Conference(EPTC2017), Singapore, December 7-10 2017, “Effect of Indium on Deformation of Binary In-Bi alloys”.

Poster:

1. 2018 Japan-Taiwan Workshop on Electronic Interconnection II, Mie, Japan, April 16 2018, “The properties of In-Bi binary alloys for low temperature”.
2. 29th European Symposium on Reliability of Electron Devices, Failure Physics and Analysis, Aalborg, Denmark, October 1-5 2018 “Shear properties of In-Bi alloy joints with Cu substrates during thermal aging”.

Acknowledgements

I would like to thank my supervisor *Prof. Hiroshi Nishikawa* for his valuable suggestions, guidance and support throughout my Ph.D. study. I really appreciate their continuous encouragement and efforts to set me on the right path. I would also like to appreciate members of doctoral committee, *Prof. Soshu Kirihara* and *Assoc. Prof. Hiroaki Muta*, for their insightful comments and helpful discussion for this dissertation.

I acknowledge the technical support that I have received throughout my Ph.D. research from *Dr. Min-su Kim* and *Dr. Omid Mokhtari* in the Joining and Welding Research Institute, particularly for the training, kind assistance and invaluable discussions in materials characterization.

I would like to express the appreciation to members and alumni of Nishikawa Laboratory, *Mr. Shiqi Zhou*, *Ms. Mai Morishita*, *Mr. Sota Yamano*, *Mr. Shunichi Koga*, *Mr. Jun Matsunobu*, *Mr. Shuhei Kanekuro*, *Mr. Kenji Inoue*, *Mr. Siliang He*, *Dr. Xiangdong Liu*, *Mr. Jin Zhi*, *Mr. Gao Runhua*, *Mr. Byungho Park*, *Ms. Satomi Takahashi*, *Ms. Misa Teranishi*, *Ms. Aiko Yonezawa*, *Ms. Sachiko Sakata* and, for their warm encouragement and invaluable friendship.

I would like to thanks the following staff in the Joining and Welding Research Institute for their great technical support: *Ms. Kunika Uehara*, *Mr. Takeshi Murakami*, *Mr. Takuya Ogura* and *Mr. Kenji Asano*.

I would like to express my thanks to members of Micro-Joining Center of Korea Institute of Industrial Technology, *Dr. Chang-Woo Lee*, *Dr. Sehoon Yoo*, *Dr. Jung-Hwan Bang* and *Dr. Yong-Ho Ko*, for their helpful advice on my research.

Thanks are also extended to all my friends and colleagues for all their helps during my stay at Osaka.

Finally, I would like to thank my family for their continuous encouragement and support all the time. In particular, I was able to graduate with my wife's devoted love. I love you so much. And thank you to my daughter for growing up well. Thank you very much for father-in-law, mother-in-law and brothers-in-law. And I really appreciate my father and mother. Thank you for raising me so far. And really miss my mother in the sky. Please be happy in there.

Jin Sanghun

Division of Sustainable Energy and Environmental Engineering, Graduate School of Engineering
Department of Manufacturing Process, Joining and Welding Research Institute
Osaka University